Université du Québec
à Rimouski

SENSIBILITÉ DES FLUX SPECTRAUX D'ÉNERGIE CINÉTIQUE AUX LIMITES DE MESURES DES RADARS HAUTES FRÉQUENCES DANS L'ESTUAIRE MARITIME DU SAINT LAURENT

Thèse présentée

dans le cadre du programme de doctorat en océanographie physique

en vue de l'obtention du grade de Philosophiae Doctor

PAR

©JEAN CLARY

Octobre 2021

Composition du jury :

Daniel Bourgault, président du jury, Université du Québec à Rimouski

Cédric Chavanne, directeur de recherche, Université du Québec à Rimouski

Louis-Philippe Nadeau, codirecteur de recherche, Université du Québec à Rimouski

Alexander Barth, examinateur externe, Université de Liège

Dépôt initial le 30 avril 2021

Dépôt final le 21 octobre 2021

À Arthur Philippe, petit homme dont je rêvais de devenir le père. À Lior, mon fils que je rêve de connaître, mais dont je suis cruellement privé. Justice sera faite.

> *"In order to progress we must recognize our ignorance and leave room for doubt. Scientific knowledge is a body of statements of varying degrees of certainty — some most unsure, some nearly sure, but none absolutely certain."*
>
> (Richard Feynmann)

> *" No one trusts a model except the man who wrote it ; everyone trusts an observation except the man who made it. "*
>
> (Harlow Shapley)

REMERCIEMENTS

Je dois en premier lieux, remercier mon directeur Cédric Chavanne, qui as toujours été d'un calme olympien avec moi. Je ne peux que le remercier pour la confiance qu'il a eu et maintenu en moi, malgré tous les aléas et toutes les tempêtes de ces six années et demi de doctorat. Je remercie aussi mon co-directeur Louis-Philippe Nadeau, grâce à qui nous avons réussi c̀onstruire une belle histoire malgré tous les désaccords en cours de route. Je remercie sincèrement James Caveen et Simon Senneville, qui sont aussi compétents que sympathiques et honnêtes. Sans eux, je ne serais arrivé (techniquement) à presque rien.

Je remercie sincèrement tous mes colocataires de doctorat, et en particulier : Maite, Myriam, Arthur, Amélie et Tsnim. C'est à Rimouski que j'ai fait les plus belles rencontres de ma vie, que j'ai rencontré les personnes les plus honnêtes et les plus sincères. En particulier, je pense à Marie, Eloisa, Camille, Fred, Léo, Quentin,... Bien sur, je remercie Gwenn qui m'a supportée au bureau, ainsi que Michel mon compagnon de doctorat, mon frère d'arme. Je remercie aussi Abigaelle pour ses commentaires sur la conclusion générale et pour ses excellentes pâtisseries. Enfin, je remercie Sandy Gregorio du fond du cœur. Son soutien et son empathie sur le plan professionnel et sur le plan affectif me sont extrêmement précieux.

AVANT-PROPOS

Je me rêvais scientifique et philosophe tout à la fois, mêlant un émotionnel sans raison avec une raison sans émotion. Mon but a toujours été de développer une compréhension rationnelle à une réalité sensible, ce qui pourrait, je pense, être une bonne définition de la physique. Comme la réalité sensible dépend de nos sens, je m'intéresse aussi aux questions liées à la perception de notre environnement. Je cherche à allier raison et perception, à l'opposé d'une vision plus classique consistant à les mettre en opposition. Cette vision classique, j'en ai fait l'expérience durant la majeure partie de ma scolarité, où la science me semblait être surtout un critère arbitraire d'intelligence, un savoir technique froid, une raison sans émotion. En conséquence, ma scolarité a été marqué par mon désintérêt à devoir ingurgiter, telle une oie, des heures de savoirs fades, puis d'être essentiellement jugé sur la capacité de reproduire un raisonnement ou un savoir technique, sans jamais douter.

Le doute est cependant au cœur de toute démarche scientifique. Il est normal de penser que les sens et/ou les raisonnements puissent être trompeurs, i.e. qu'une observation et/ou une théorie puissent être biaisées. La remise en question d'un savoir est nécessaire lorsque une théorie est contredite par l'expérience. En général, soit la théorie doit être corrigée (solution législative) soit la grandeur observée contient une autre information (solution ontologique). Pour donner un exemple, la loi de la gravité newtonienne a permis la découverte de Neptune par le calcul, mais cette même loi s'est revélée non adaptée pour expliquer les anomalies de trajectoire de Mercure pres du Soleil.

Cette perte de certitude peut être psychologiquement difficile à vivre. Il m'a fallu considérer qu'une part de mon savoir relevait plus de la croyance et de l'interprétation que d'une vérité absolue reconfortante. La confrontation au réel a souvent été déroutante durant cette thèse, d'une part parce qu'on n'est pas sûr de la grandeur mesurée ni même de la bonne qualité de la mesure et d'autre part parce que le modèle ne sera jamais qu'une représentation idéalisée de la réalité. On n'est jamais plus ignorant que de sa propre ignorance. Cette leçon d’humilité est importante à mes yeux.

Quand Cédric m’as choisi pour mener ce projet de doctorat (j’ignore toujours pourquoi), le cheminement était assez limpide : des radars sont mis en place, il suffit d’exploiter les mesures pour avoir des cartes de courants, puis d’estimer la cascade d’énergie. En fait, j’ai passé la majorité de mon doctorat à déconstruire ces grandes lignes, sans que Cédric ne me lâche, pour chercher à comprendre ce qu’on mesure ou savoir ce qu’on peut mesurer. J’ai tenté d’améliorer le traitement des mesures HFRs en cherchant à savoir ce qui est possible de mesurer et de valider. Ce doctorat met clairement en avant les difficultés liées à l’utilisation des radars à hautes fréquences pour estimer directement les flux spectraux de KE à des échelles suffisamment petites pour que de multiples processus coexistent.

.

RÉSUMÉ

L'énergie dans les océans est essentiellement fournie aux grandes échelles par les vents, les flux atmosphérique de chaleurs et les marées. On sait aussi que l'essentiel de cette énergie est perdu par dissipation visqueuse moléculaire. Par contre, on ignore ce qui se passe en détail entre ces deux extrêmes. Si les grandes échelles spatiales et temporelles sont bien mesurées par les satellites altimétriques, les échelles plus fines sont peu ou mal observées, en raison des contraintes de résolution spatiale et temporelle. L'utilisation de radars à hautes fréquences permet de mesurer une région côtière quasiment en continu et à des résolutions suffisantes pour distinguer les processus super-inertiels et/ou subméso-échelles. Essentiellement, nous montrons que les flux spectraux d'énergie cinétique du courant rotationnel ($\sim$ en équilibre)sont bien estimés lorsque les courant totaux sont relativement bien reconstruits (il faut un minimum de 70% de mesures indépendantes) et que les effets de géométrie (non-périodicité, taille du domaine) modifient les grandes échelles alors que les limites de résolution et de bruit de mesures modifient surtout les petites échelles. Nous montrons aussi que l'échelle de transition (échelle de changement de signe du transfert d'énergie) du courant rotationnel est bien estimée, même si l'amplitude du flux ne l'est pas forcément. Nous montrons aussi que les incertitudes de mesures et les divers moyens de les compenser changent surtout les flux du courant non-rotationnel. Comme les interactions sont fortement non linéaires, le moyennage en temps doit se faire en évitant de filtrer la dynamique non-rotationnelle.

Mots clés : estuaire, observation, radar à haute fréquence, turbulence, interpolation, transfert d'énergie

ABSTRACT

Energy in the oceans is primarily supplied at large scales by sunlight, winds and tides. We also know that most of this energy is lost by viscous dissipation at very small scales. On the other hand, we do not know what happens in detail between these two extremes. If the large spatial and temporal scales are well measured by satellite altimeters, the finer scales are little or poorly observed, due to the constraints of spatial and temporal resolution. The use of high frequency radars makes it possible to measure a coastal region almost continuously and at resolutions sufficient to distinguish super-inertial and / or submesoscale processes. Essentially, we show that kinetic energy spectral fluxes of rotational(~ balanced) currents are correctly inferred when total currents are relatively well mapped (a minimum of 70 % of independent measurements is necessary) and that the effects of geometry (non-periodicity, size of the domain) modify the large scales while the limits of resolution and measurement noise mainly modify small scales. We also show that the transition scale (positive to negative spectral fluxes) of the rotational current is well estimated, even if the amplitude of the flux is not necessarily so. We also show that the uncertainties of measurements and the various mitigations mainly change the flows of the non-rotational current. As non linear interactions are important, time averaging must not filter out non-rotational dynamics.

Keywords : observation, estuary, high frequency radar, turbulence, interpolation, energy transfer

TABLE DES MATIÈRES

LISTE DES TABLEAUX

LISTE DES FIGURES

INTRODUCTION GÉNÉRALE

Le but de ce doctorat est d'estimer les interactions courants-courants (appelé aussi ”le transfert spectral d'énérgie cinétique) à la surface de l'estuaire maritime du Saint-Laurent. Ces courants sont obtenus à partir de mesures de radars à hautes fréquences (RHFs). Les étapes principales sont 1) tester les conditions dans lesquelles les transferts d'énergie cinétique sont vraisemblables, 2) mener un contrôle de qualité rigoureux sur les mesures puis les combiner, et 3) analyser ces transferts au regard du cadre théorique et des conditions dynamiques environnantes (bathymétrie, vents, variations saisonnières).

Plus généralement, ce doctorat vise à améliorer l'état des connaissances des transferts d'énergie cinétique à des échelles spatiales de l'ordre de 1-10 km, qui ne sont pas observables à partir de mesures altimétriques satellitaires. Mieux connaître ces transferts à de petites échelles spatiales est essentiel à l'amélioration des modèles océaniques, des échanges entre l'océan et l'atmosphère, et de l'activité biologique à certains endroits du globe. À notre connaissance, il n'existe qu'une seule étude scientifique ayant cherché à estimer les transferts spectraux d'énergie à partir de RHFs, celle de Soh and Kim (2018).

0.1 Contexte

0.1.1 Vision générale

Les océans représentent environ 70% de la surface de la Terre. Depuis le début de l'ère anthropique, ils ont capturé environ 90% de la chaleur produite par l'activité humaine (due au CO2 et à d'autres gaz à effet de serre). Cette capacité de l'océan à capturer le CO2 et la chaleur est en grande partie due aux tr´es nombreux courants hors équilibre existant dans l'océan.

Ces courants ont des échelles spatiales allant d'environ 1 m à environ 1000 km. Les échelles pour lesquelles les effets de la rotation de la Terre sont bien plus grands que ceux de l'advection (les méso-échelles) sont bien comprises. Les échelles pour lesquelles les effets de l'advection sont importante (les subméso-échelles) sont moins bien comprises. Les avancées faites les dernières années ont néanmoins permis de comprendre que les subméso-échelles sont la clef pour comprendre les échanges thermiques avec l'atmosphère (Su et al., 2018). Ces subméso-échelles se caractérisent par la création locale de fortes vitesses verticales, qui permettent aussi l'oxygénation de l'océan, la capture de CO2 ou l'activité planctonique (Martin and Pondaven, 2003; Lévy et al., 2012b,a). Ces subméso-échelles sont difficiles à observer car elles sont éphémères et varient aussi bien saisonnièrement que géographiquement. Elles jouent pourtant un rôle important dans la circulation océanique et dans les couplages physico-chimiques. Il est crucial de mieux étudier ces subméso-échelles pour mieux comprendre les défis liés au réchauffement climatique. Malheureusement, la résolution numérique de tous les processus existant est impossible, même dans un proche futur. Il faudrait des ordinateurs environ 10 milliards de fois plus puissant (Fox-Kemper et al., 2019). La solution actuelle consiste à utiliser des approximations mathématiques, mais il est difficile de savoir si ces représentations sont correctes ou pas. Les erreurs ne peuvent être remarquées qu'en comparant avec les observations et les expériences en laboratoire.

Les études numériques considérant les subméso-échelles se font sur un domaine restreint (Klein et al., 2008; Capet et al., 2008c; Thomas et al., 2008; Lévy et al., 2010). Les subméso-échelles sont essentiellement prises en compte par l'utilisation d'une résolution impossible à adopter pour un modèle de prévision globale. Ces études vont dans le sens d'une modification de la circulation méso-échelle par les subméso-échelles. L'idée générale qui ressort de toutes ces études est que vouloir modéliser et prévoir l'évolution de la circulation océanique, et donc des changements climatiques, c'est comme vouloir modéliser la respiration dans les poumons sans considérer les alvéoles, où se déroulent les échanges de gaz entre l'air et le sang (Ferrari, 2011).

L'idée que les subméso-échelles puissent modifier les méso-échelles a longtemps été

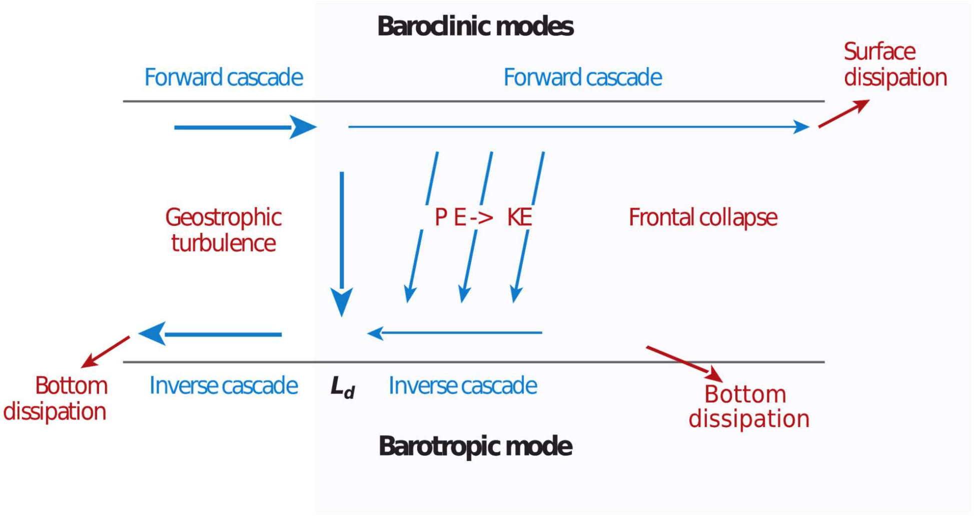

Figure 1: Représentation schématique des transferts d'energie. Extrait de Ferrari and Wunsch (2009). Les forcages aux grandes échelles maintiennent l'APE. Dans la figure, EKE est l'énergie cinétique des tourbillons. L'énergie barocline contient APE et EKE alors que l'énergie barotrope contient uniquement de l'EKE.

négligée car environ 80% de l'énergie cinétique (KE) présente dans les océans se trouvent aux méso-échelles, où elle est en équilibre hydrostatique et géostrophique. L'essentiel de l'énergie est fournie aux océans aux grandes échelles spatiales. Elle provient du forçage atmosphérique (ensoleillement et vents) et des marées. En raison de ces forçages, la densité ne dépend pas que de la pression, mais aussi de la température et de la salinité. Par conséquent, les surfaces d'égale pression et les surfaces dégale densité ne sont alignées. Un tel écoulement est dit barocline. Si une perturbation suffisamment puissante affecte un tel écoulement, alors les isopycnes (lignes d'égale densité) perdent de leur inclinaison. De l'énergie potentielle disponible (APE) est alors libérée par abaissement du centre de gravité. Cette transformation de APE en KE existe préférentiellement aux échelles proches du rayon de déformation de Rossby (R_d). Une vision schématique est montrée par la figure 1.

Les tourbillons créés par la transformation de APE en KE transfèrent de la quantité de mouvement de la surface vers le fond, faisant perdre à l'écoulement son caractère barocline. Pour un écoulement barocline le transfert d'énergie se fait vers les petites échelles, alors que pour un écoulement non-barocline (e.g. barotrope), le transfert d'énergie se fait vers les grandes échelles. Aux échelles proches du rayon de déformation de Rossby, environ 3/4 de l'énergie barocline est convertit en énergie barotrope, ce qui se traduit par l'existence d'une échelle de transition (le transfert de KE passe du caractère directe à inverse). Le flux spectral de KE change de signe (équation 1).

0.1.2 Formulation mathématique

L'impact des subméso-échelles sur les méso-échelles peut être quantifié en calculant le flux spectral de KE (Π), i.e. la quantité d'énergie cinétique qui passe à travers une longueur d'onde donnée à partir des longueurs plus grandes.

$$\Pi(k) = -\int_{k}^{\infty} \widehat{\mathbf{u}^*}.(\widehat{\mathbf{u}.\nabla_{\mathbf{h}})\mathbf{u}}dk \tag{1}$$

où $\mathbf{u}$= u$\mathbf{i}$+v$\mathbf{j}$ est le vecteur courant, $\hat{}$ est l'opérateur transformée de Fourier, .* est le conjugué complexe, et $\mathbf{u}.\nabla_{\mathbf{h}} = u\dfrac{\partial}{\partial x} + v\dfrac{\partial}{\partial y}$ est l'opérateur lié à l'advection. Sans intégrale, le transfert spectral correspondrait aux sources et aux puits à chaque longueur d'onde mais sans connaître explicitement le sens de la cascade d'énergie (Scott and Arbic, 2007). La définition du flux spectral d'énergie cinétique s'obtient en multipliant l'équation de Navier Stokes par $\mathbf{u}$. Seul le terme lié à l'advection permet de redistribuer de l'énergie selon les échelles spatiales. Il s'agit de la 'triade d'interaction' dans la littérature de la turbulence (Tsinober, 1996; Kraichnan, 1971; Salmon, 1980; CHEN et al., 2005; Moffatt, 2014).

La difficulté de l'estimation de Π provient du besoin de connaître le champ $\mathbf{u}$ partout (nécessaire pour calculer la transformée de Fourier) ainsi que la nécessité de bien connaître le gradient horizontal des courants. Dans les études numériques tout est connu mais pour les observations c'est plus difficile. Les observations récentes en plein océan (Shcherbina et al., 2013; Callies and Ferrari, 2013; Callies et al., 2015) sont réalisées sur des transects (une seule dimension horizontale), ce qui empêche le calcul du flux spectral. Ces études reposent sur le calcul de la répartition de KE selon l'échelle spatiale, i.e. le spectre de KE, sur le transect pour ensuite déduire le sens du transfert de KE.

Il n'est cependant pas évident de déduire le sens de la cascade d'énergie cinétique à partir de la seule connaissance de la pente du spectre. Une pente du spectre en $k^{-5/3}$ peut signifier une cascade vers les grandes échelles (en turbulence 2D) ou vers les petites échelles (turbulence 3D). La différence fondamentale vient de la possibilité au tourbillon de s'étirer en turbulence 3D. En raison de la conservation de la vorticité potentielle, si un tourbillon s'étire, alors il tourne plus vite (création de vitesse). En général, les observations sont analysées au regard de la théorie quasi-géostrophique (QG, pente du spectre de KE en k^{-3}) et de la théorie quasi-géostrophique de surface (SQG, pente du spectre de KE en k^{-2}). En QG, les courants subméso-échelles sont très faibles et n'ont aucun effet sur la circulation générale alors qu'en SQG les courants subméso-échelles peuvent modifier la circulation générale via une cascade de KE inverse. Cependant, les régimes QG et SQG sont en compétition. La domination d'un régime sur l'autre varie saisonnièrement (Sasaki et al., 2014) suite au renforcement du régime de surface en hiver. La cause en serait la forte production de subméso-échelles en hiver par les instabilités de la couche de mélange (Boccaletti et al., 2007; Fox-Kemper et al., 2008). Ces instabilités ont été mises en avant dans de multiples études (Mensa et al., 2013; Callies and Ferrari, 2013; Sasaki et al., 2014; Callies et al., 2015). La dominance d'un régime par rapport à l'autre n'est toutefois pas toujours très claire (Xu and Fu, 2011).

0.1.3 Observations altimétriques

Le premier besoin pour estimer des flux spectraux de KE à partir d'observations est celui de connaître les deux composantes du courant horizontal. Historiquement, ce besoin a été satisfait en premier par les altimètres. Ceux-ci mesurent l'élévation de la hauteur de la mer (ssh), duquel le courant géostrophique est déduit. Ces courants sont forts aux méso-échelles mais faibles aux subméso-échelles, où la cascade inverse débute (Capet et al., 2008a; Klein et al., 2008). Les mesures des altimètres AVISO sont généralement données au 1/3° (environ 40 km, dépendamment de la latitude). La première estimation directe des transferts d'énergie, à partir de mesures altimétriques, montre l'existence d'une cascade inverse aux échelles supérieures à 150 km (Scott and Wang, 2005). Cette observation est en accord avec la théorie de la turbulence 2D (i.e. barotrope) mais est en contradiction avec le fait que les altimètres capturent essentiellement le premier mode barocline (Wunsch, 1997). L'étude de Scott and Arbic (2007) montre que l'énergie totale barocline cascade bien vers les petites échelles mais que l'énergie cinétique barocline subit une cascade inverse.

Le deuxième résultat surprenant de Scott and Wang (2005) est l'échelle de transition entre cascade inverse et cascade directe trouvée (environ 150 km). Des études ultérieures montrent que l'échelle de transition du courant géostrophique est très sensible à la résolution spatiale et temporelle (Arbic et al., 2012, 2013, 2014). La résolution effective des altimètres actuels (environ 100 km) est un vrai problème. Les procédures de grillage des bandes mesurées par les altimètres provoquent la fusion des structures non résolues. Ce biais d'observation se traduit par la surestimation des tourbillons méso-échelles, la sous-estimation en densité des tourbillons et la surestimation du rayon de déformation (Amores et al., 2018). Ces biais sont la cause probable de la surestimation de l'échelle de transition. Même avec la prochaine génération d'altimètres (SWOT et COMPIRA), seule les échelles supérieures à 40 km seront observable en raison des bruits de mesures (Gómez-Navarro et al., 2018), malgré une résolution effective de 15-20 km (Fu and Ubelmann, 2014). Il sera donc difficile, même avec la prochaine génération d'altimètres d'étudier les subméso-échelles.

La résolution d'observation n'est pas la seule limite importante des altimètres. La deuxième limite est due au fait que les altimètres mesurent la hauteur de surface de la mer (ssh). D'une part la ssh est considérablement modifiée par les ondes internes, qui ne sont pas en équilibre géostrophique et dont on ignore la signature sur les courants géostrophiques. D'autre part, il n'est possible de déduire que les courants géostrophique qui sont de moins en moins importants à mesure qu'on descend vers les subméso-échelles.

0.2 Les radars à haute fréquence

En raison des limites d'observation des altimètres, il est nécessaire de recourir à d'autres systèmes de mesures. Des trajectoires suivies par GPS ont récemment été utilisées pour inférer indirectement le transfert d'énergie en surface (Poje et al., 2017; Mensa et al., 2018). L'existence de biais statistiques fausse néanmoins l'estimation d'une éventuelle échelle de transition (Pearson et al., 2019). Les drifters ont tendance à s'accumuler dans les zones de convergence, en conséquence l'échantillonage de la région observée n'est pas uniforme, ce qui cause des biais dans les flux spectraux estimés ̀partir de drifters. La seule manière d'estimer directement les transferts de KE nécessite la connaissance du champ de courant bidimensionnel, sur des temps suffisamment longs. Or, il se trouve que de multiples radars à haute fréquence (RHFs) peuvent être combinés pour obtenir le courant en surface, duquel le transfert spectral d'énergie cinétique peut être estimé. La seule étude connue reposant sur ce principe est celle de Soh and Kim (2018). Ces RHFs ont une résolution spatiale de 1-10 km (dépendamment de la fréquence utilisée) et une résolution temporelle d'environ 1 heure, ce qui permet de mesurer les multiples dynamiques subméso-échelles (Ardhuin et al., 2008; Kim, 2010; Chavanne et al., 2010; Kim and Kosro, 2013).

Les RHFs sont des appareils de télédétection. Le signal électromagnétique émis se propage à la surface de l'eau. Il est rétro-diffusé de manière cohérente lorsque la longueur d'onde des ondes de gravité de surface est égale à la moitié de la longueur d'onde de l'onde émise (figure 2). Si l'océan était complètement plat, il n'y aurait pas de signal retour. Le décalage entre la fréquence du signal retour et du signal émis permet de calculer la vitesse du courant dans la direction du RHF émetteur. Autrement dit, un RHF ne mesure qu'une composante du courant.

Il faut combiner les courants perçus par plusieurs RHFs pour estimer les deux compo-

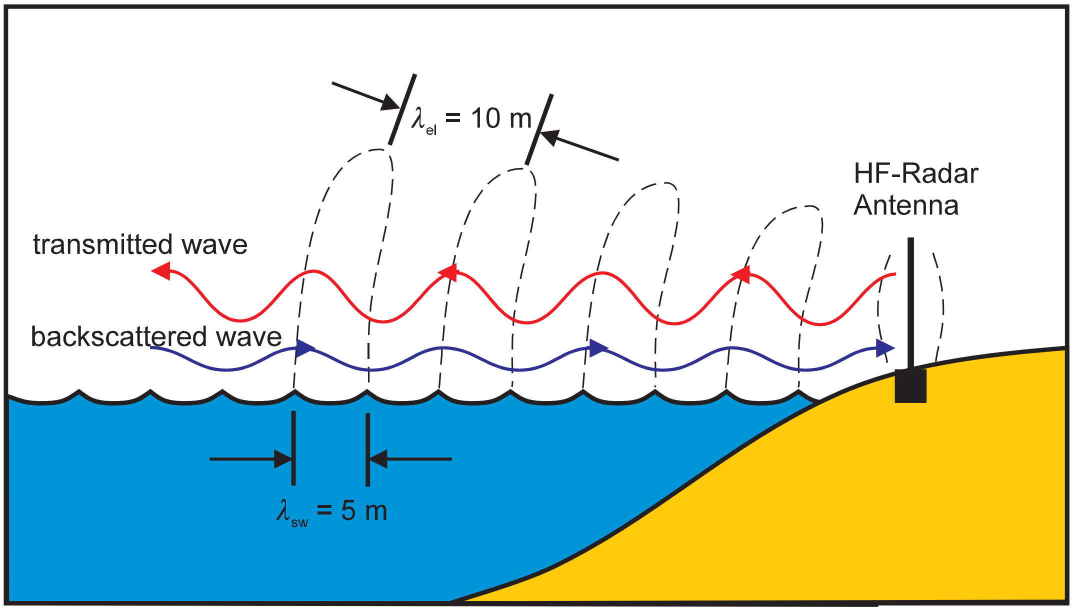

Figure 2: Schéma du fonctionnement des RHFs, par Klaus-Werner Gurgel, Université de Hambourg (Allemagne). La vitesse du courant dans la direction du radar est calculée à partir du décalage entre la fréquence du signal émis et du signal reçu. La fréquence du signal retour est modifiée par la vitesse de propagation des vagues par lesquelles laquelle l'onde émise est rétro-diffusée (effet Doppler).

santes du courant de surface. Il existe plusieurs méthodes de combinaison. La plus utilisée est la plus simple à mettre en oeuvre mais est la moins robuste aux diverses limitations de mesures. Ces limites sont : la portée, l'absence de données, le bruit de mesures, le problème de localisation. La portée d'un RHF augmente avec la longueur d'onde, et la résolution radiale augmente avec la bande passante. En théorie, ces deux grandeurs sont indépendantes, mais elles sont liées en pratique car la bande de fréquences utilisable est définie par la législation. La capacité de l'onde émise à se propager à la surface de l'eau dépend de la conductivité du milieu. L'aire observable diminue avec la diminution de la salinité et en présence de glace de mer (Gurgel et al., 1999; Kamli et al., 2016). Il existe aussi des trous dans les mesures car certaines directions sont mal ou peu observées. Le nettoyage des mesures brutes élimine aussi beaucoup de mesures suspectes. Ce nettoyage dépend des contrôles mis en place par l'utilisateur. Le dernier point délicat est la détermination de la direction du signal retour. Nous utilisons les CODARs en ”*direction finding*” et en ayant de multiples antennes réceptrices avec des sensibilités plus grandes dans certaines directions que dans d’autres. Les WERAs opérent en ”*beamforming*”, ce qui consiste à utiliser un réseau d’antenne récepteur régulièrement espacé de manière à ce que les signaux reçus soient en phase dans certaines directions uniquement.

0.3 L’estuaire maritime du Saint-Laurent

L’aire d’étude est l’estuaire maritime du Saint Laurent (LSLE).La longueur de ce canal est de 200 km et sa largeur varie entre 30 km et 60 km. La largeur de l’estuaire, de plusieurs rayons de déformation de Rossby $L_d \sim 10$ km (Mertz et al., 1988) est suffisante pour que les effets de la force de Coriolis soient significatifs et pour permettre le développement d’ondes instables et de tourbillons à méso-échelle Mertz et al. (1990).

La bathymétrie accidentée du LSLE (figure 3) est propice à la génération d’ondes de gravité internes (IGWs), ce qui peut extraire de l’énergie cinétique d’un courant en équilibre géostrophique (Nikurashin and Ferrari, 2010; Nikurashin et al., 2013). Le LSLE est également soumis à de multiples forçages tels que les marées (Koutitonsky et al., 1990; Koutitonsky and Bugden, 1991; Ingram and El-Sabh, 1992), les vents (Koutitonsky and Bugden, 1991; Mertz and Koutitonsky, 1992; Ingram and El-Sabh, 1992), et les apports d’eaux douces (Mertz, 1989; Koutitonsky et al., 1990).

Le LSLE est également soumis à une forte variabilité saisonnière, avec la présence d’une couche de glace partielle en hiver. Cette variabilité saisonnière se traduit par une stratification typique des milieux subarctiques. Au dégel, la couche de surface est recouverte par les eaux de la fonte provenant du bassin versant. Ceci créé un système à trois couches au printemps, qui s’érode durant l’été et l’automne. La couche intermédiaire est plus froide que la couche de surface et que la couche de fond, alors que la salinité va en augmentant avec la profondeur (Cyr et al., 2011). Cette disposition est favorable aux instabilités baroclines.

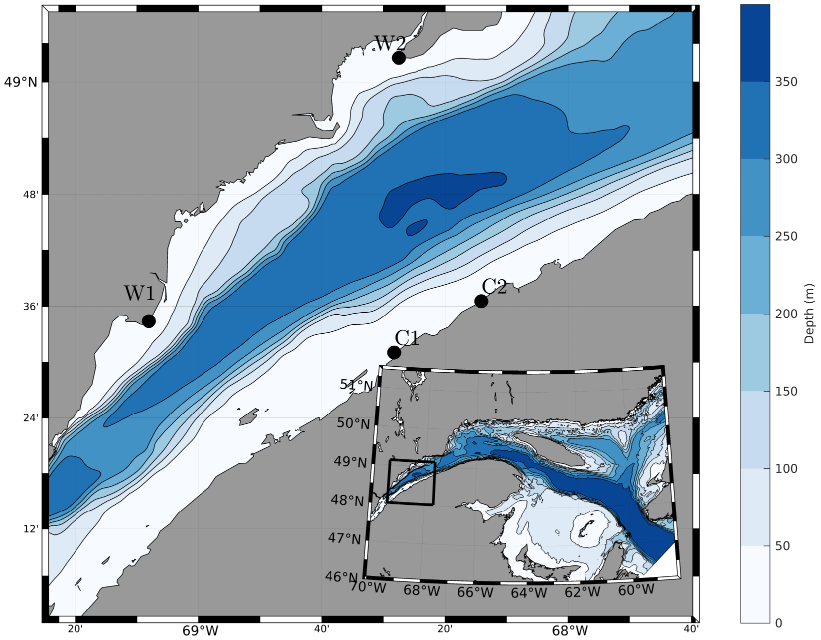

Figure 3: Bathymétrie du Golfe et de l'estuaire du Saint Laurent.

Les RHFs, placés au niveau des points noir sur la figure 3, permettent aussi de mesurer une partie des IGWs et les ondes quasi-inertielles (NIWs) qui peuvent aussi extraire de l'énergie cinétique du courant géostrophique. En comparaison, il est impossible de mesurer les courants de ces ondes avec des altimètres.

Nous utilisons tout au long du doctorat les sorties du modèle régional GSL développé par Environnement et Changement Climatique Canada. Le modèle est une simulation NEMO (http ://www.nemo-ocean.eu) avec une résolution horizontale de 500 m et une résolution verticale de 1 m proche de la surface. Le domaine du modèle régional s'étend de l'extrémité ouest de l'estuaire du Saint-Laurent à Belle-Île et au détroit de Cabot. Cependant nous ne nous servons que des simulations que dans une zone relativement petite, située relativement près de l'extremité ouest du modèle. Les paramètres utilisés sont les mêmes que ceux décrit dans (Paquin et al., 2020).

0.4 Problématique et objectifs

En théorie, les flux de KE estimés à partir de multiples RHFs permettent d'étudier les échelles spatiales et temporelles non résolvables par les altimètres. Et en pratique ? C'est toute la question de ce doctorat. Ce doctorat est essentiellement une étude de faisabilité. Nous cherchons à déterminer *à priori* le cadre dans lequel les flux spectraux peuvent être inférés. À titre de comparaison, les premières estimations de flux à partir d'altimètres datent de 2005 (Scott and Wang, 2005) mais les études de faisabilité sont bien plus récentes (Arbic et al., 2013; Amores et al., 2018) pour tenter d'expliquer *à posteriori* les estimations de flux spectraux et en particulier l'échelle de transition.

Puisque les estimations de flux spectraux à partir d'altimètres ont permis de grandes avancées bien qu'étant partiellement fausses, nous espérons que les estimations faites à partir de mesures radars dans un cadre bien défini permettront des avancées majeures dans l'étude des processus physiques et des transferts d'énergie aux subméso-échelles. Comme la prochaine generation d'altimètres pourra observer les régions côtières, il sera possible de combiner localement mesures altimétriques et mesures radars. Ce doctorat constitue une étude pionnière en répondant aux trois questions suivantes :

1. Peut-on bien estimer les flux spectraux de KE du courant rotationnel à partir de mesures radars ?
2. Peut-on estimer les flux spectraux de KE des autres modes de courants, ainsi que leur interactions à partir de mesures radars ?
3. Les flux spectraux de KE estimés à partir des radars installés dans le LSLE sont ils en accord avec ceux du modèle régional GSL (résolution spatiale de 500 m) ?

La première problématique est répondue dans le premier article, les deux autres problématiques sont posées dans les deux articles suivants. En fond du deuxième et du troisième article, il y a le retraitement complet des procédures de mesures des RHFs. La majorité de ce doctorat consiste non pas à comprendre la dynamique dans le LSLE mais à identifier et corriger au mieux les différentes sources d'erreurs possibles.

Chapitre I Dans le premier chapitre du doctorat, nous utilisons un modèle quasi-géostrophique doublement périodique pour estimer les conditions d'observations des RHFs et les conditions dans lesquelles les flux spectraux peuvent être correctement estimés. Une attention particulière est portée sur la combinaison des courants des RHFs, le bruit dans les mesures ainsi que les trous. Le résultat essentiel est que la méthode de combinaison la plus adaptée est le 2Dvar (méthode non locale). Des seuils d'acceptabilité du niveau de bruit et du manque de mesures sont définis dans le but d'écarter les courants totaux suspects.

Chapitre II Dans le deuxième chapitre du doctorat, nous utilisons un modèle aux équations primitives fourni par Environnement Canada avec une résolution spatiale de 0.5 km. Nous montrons que le flux spectral de KE est très variable (distribution non gaussienne très étendue), ce qui a deux conséquences importantes. D'abord la moyenne est biaisée par les valeurs extrêmes, ensuite il est nécessaire d'intégrer suffisamment de mesures pour avoir un résultat statistiquement significatif. Nous trouvons que ce temps d'intégration doit être d'au moins 3 mois, permettant donc d'étudier ensuite l'évolution saisonnière. Le courant de surface est décomposé en courant de marées, en courant rotationnel et en courant divergent. Nous montrons ensuite que les problèmes d'observations (bruits, absence de données et erreurs de localisation) affectent essentiellement les flux du courant divergent et les interactions entre le courant divergent et le courant rotationel. Imposer des seuils d'acceptation sur les mesures et moyenner en temps aident à atténuer partiellement les effets de ces erreurs sur les flux spectraux. Le moyennage en temps doit se faire en évitant de filtrer la dynamique hors équilibre.

Chapitre III Dans le troisième chapitre, nous cherchons à comparer le modèle régional et les observations. Le modèle régional montre une très faible variabilité saisonnière en surface contrairement aux observations. Modèle et observations concordent sur l'absence d'un pic d'énergie aux fréquences quasi-inertielles et sur l'absence d'ondes d'inertie-gravité. Ce chapitre n’est, en l’état, pas prêt à la publication. Surtout, ce chapitre montre combien l’objectif de ce doctorat, à savoir estimer les transferts d’énergie cinétique à partir de mesures de RHFs, est délicat, car les observations et le modèle régional restent en désaccord malgré tous les efforts de contrôle qualité faits sur l’ensemble du doctorat.

ARTICLE 1

EFFETS DES LIMITATIONS DES MESURES DE RADARS À HAUTE FRÉQUENCE SUR LES FLUX SPECTRAUX D'ÉNERGIE

Ce premier article "*The Effect of Measurement Limitations on High-Frequency Radar-Derived Spectral Energy Fluxes*" a été soumis en Décembre 2018 au Journal of Atmospheric and Oceanic Technology, et a été accepté sous sa forme finale en Août 2019. L'idée originale provient de Xavier Capet. La plupart des résultats ont été présentés en session poster au Colloque de Liège Colloquium en 2017 par mon directeur (j'avais des soucis avec les services d'immigration canadiens) et durant l'Ocean Science à Portland en février 2018. En tant que premier auteur, mon travail consiste à produire les analyses nécessaires, développer et/ou comparer diverses méthodes de calcul, et à rédiger la première version de l'article. Le modèle utilisé est celui du premier co-auteur, Louis-Philippe Nadeau, le savoir théorique et pratique concernant les radars à haute fréquences ainsi que les vraies mesures utilisées appartiennent au troisième co-auteur, Cédric Chavanne.

Résumé en français

Les transferts d'énergie cinétique sont observées aux grandes échelles par les altimètres et sont étudiées numériquement sur presque toutes les échelles spatiales existante dans l'océan. Malheureusement, il est très compliqué d'étudier ces transferts aux échelles spatiales et temporelles non résolues par les altimètres en raison des conditions requises. Nous montrons ici que les radars à haute fréquence peuvent remplir ce manque observationnel suivant certaines conditions. Premièrement, nous comparons plusieurs méthodes de recombinaison des mesures et montrons clairement que la méthode la plus couramment utilisée dans la monde et celle qui introduit les plus grands biais. Deuxièmement, nous montrons que l'échelle de

transition d'un transfert vers les petites échelles à un transfert vers les grandes échelles est particulièrement robuste au multiples limites observationnelles. Nous proposons néanmoins un seuil minimal de mesures pour considérer que les courants recombinés sont robustes. Enfin, nous validons qualitativement ces résultats pour un modèle PE bien plus réaliste que le modèle QG doublement périodique.

ABSTRACT

The ocean's inverse cascade of energy from small to large scales has been confirmed from satellite altimetry for scales larger than 100 km. However, measurements of the direct energy cascade to smaller scales have remained difficult to obtain. Here, the possibility of estimating these energy transfers to smaller scales from observations by high frequency radars is investigated using numerical simulations. Synthetic measurements are first extracted from a quasigeostrophic simulation of freely decaying turbulence for which the reference energy flux is characterized by the transition from positive to negative values. Fluxes obtained from synthetic data are compared to this reference flux in order to assess the robustness to various measurements limitations. The geometry of the observational domain (non-periodicity, domain size and aspect ratio) affects mostly large scales, while the spatial resolution of the instruments affects mostly small scales. In contrast, measurement noise and missing data affect both large and small scales. Despite resulting significant biases in the amplitude of the fluxes, the transition scale between the positive to negative fluxes is relatively robust to measurement limitations. These results are also confirmed using a simulation from a primitive equations model in a realistic coastal geometry.

1.1 Introduction

The bulk of the energy input in the ocean is injected at large scales ($L > 1000$km) by lunisolar tides and atmospheric fluxes of momentum and buoyancy. In contrast, energy dissipation occurs at small scales ($L < 1$mm). Major gaps still exist in our understanding of how the ocean circulation closes this energy budget. In recent decades, it became clear that the dynamics of scales larger than the deformation scale is fundamentally different from those of the smaller scales.

At large scales, Earth's rotation constrains horizontal motions to be approximately in geostrophic balance (hereafter balanced motions). For relatively weak background potential vorticity (PV) gradient, these balanced motions are characterized by an inverse kinetic energy (KE) cascade (Charney, 1971; Salmon, 1980, 1998), for which energy is transferred from smaller to larger scales. Direct transfer of KE from larger to smaller scales can also occur locally in regions of strong background PV gradients, such as in western boundary currents (Straub and Nadiga, 2014). Nevertheless, balanced dynamics requires parameterizations of motions smaller than the deformation scale in order to close the energy budget.

Earth's rotation plays a lesser relative role for scales smaller than the deformation radius, allowing dynamics to depart far from geostrophic balance (hereafter unbalanced motions). These unbalanced motions are generally characterized by a direct KE cascade from larger to smaller scales, en route to dissipation (McWilliams et al., 2001; Molemaker et al., 2005; Klein et al., 2008; Molemaker et al., 2010). Understanding how unbalanced motions are generated and interact with balanced motions is crucial to parameterize their role in closing the energy budget.

While significant progress has been achieved on understanding these mechanisms from a numerical standpoint (e.g., Vanneste and Yavneh, 2004; Molemaker et al., 2005, 2010; Scott et al., 2011; Vanneste, 2013; Nikurashin et al., 2013; Xie and Vanneste, 2015; Taylor and Straub, 2016), observations have remained scarce due to the high spatial and temporal resolution required. From an observational standpoint, most of our understanding of the ocean KE budget is derived from altimetry data (Scott and Wang, 2005; Arbic et al., 2013, 2014), which has confirmed the existence of an inverse KE cascade of balanced motions at scales larger than 100 km. However, exploration of the unbalanced small scale motions from altimetry alone is not possible with the present day spatial and temporal resolution of the satellite sensors. In addition, even with the expected increase in spatial resolution of future satellite missions, it is unclear how the unbalanced motions project on the sea surface height.

Recently, attempts to gain insight into KE transfer at scales smaller than the deformation radius has been made using measurements of surface currents from GPS tracked drifters (e.g., Poje et al., 2017; Mensa et al., 2018). Using classical Kolmogorov scaling arguments, they show observational evidence for a direct energy cascade at scales smaller than 1km to 10km and an inverse cascade at larger scales. However, Pearson et al. (2019) pointed out that the transition scale obtained using surface drifters is underestimated due to statistical biases.

A direct estimation of KE fluxes has been recently attempted using coastal surface currents from High Frequency Radars (HFR, Soh and Kim, 2018). HFR have a spatial resolution of roughly 1-5 km, with a range of about 100km and a temporal resolution of about 1 hour, enabling to capture both balanced and unbalanced motions (e.g., Ardhuin et al., 2008; Kim, 2010; Chavanne et al., 2010; Kim and Kosro, 2013). Soh and Kim (2018) applied standard spectral methods to HFR currents to estimate energy fluxes for horizontal scales ranging from 2 km to 25 km and observed a wide range of behaviors including inverse and direct cascades. While promising, interpreting the signification of these results in the context of the ocean's KE budgetWhile promising, interpreting the signification of these results in the context of the ocean's KE budget is made challenging due to the unknown effects of various sources of observational errors on the estimation of KE spectra and fluxes.

Here, we systematically investigate the effect of the main sources of errors on estimating KE spectral fluxes using HFR measurements. To constrain the errors, we use model data instead of observations in order to derive an "ideal" reference flux. Synthetic observations with various sources of errors are then generated from this model data. Fluxes estimated from these synthetic observations are compared to the reference to quantify the effect of each source of error. In Section 2, we present the numerical model and its energy budget, from which we define the reference KE flux. Then, in Section 3, we estimate the effect of each source of errors on the "observed" KE flux by comparing to the reference. Implications for estimating KE fluxes from actual HFR data are discussed in Section 4.

1.2 Reference Kinetic Energy Flux

Most recent numerical studies (e.g., Capet et al., 2008a,c; Klein et al., 2008; Tulloch et al., 2011; Straub and Nadiga, 2014; Arbic et al., 2014) predict KE fluxes that share the same essential qualitative structures: (i) an inverse cascade at large scales, (ii) a direct cascade at small scales, and (iii) a transition scale that coincides roughly with the deformation radius. We seek a reference flux that displays this basic structure, but with minimum complexity of the underlying physical model. The simplest configuration that yields these essential features is the quasigeostrophic model (Emery, 2001). Although small scale unbalanced motions are parametrized by sub-grid scale dissipation in this model, a range of positive fluxes results from its dynamics (see below) and occurs at similar scales than more complex primitive equations models (e.g., Klein et al., 2008; Capet et al., 2008c; Arbic et al., 2013).

The simulations are performed using a simplified version of the numerical model described in Nadeau and Straub (2009). In the configuration used here, the model solves the two-layer quasigeostrophic potential vorticity equation, under the rigid lid approximation. The thicknesses of the upper and lower layers are $H_1 = 1000$ m and $H_2 = 5000$ m, respectively. In order to facilitate the Fourier analysis required to compute the reference flux, the model geometry is a doubly periodic domain of equal length and width, $L_{domain} = 2000$ km. The horizontal resolution is dx =1.95 km. Biharmonic dissipation, with $A_h = 15\times10^6$ m^4 s^{-2}, is applied in both layers (see Appendix A). Bottom drag is set to zero. The Coriolis parameter is $f_0 = 10^{-4}$ s^{-1} and the Rossby deformation radius is defined as $\mathrm{R}_d = \sqrt{g' H_1 H_2 / H f_0^2}$, where g' is the reduced gravity and $H = H_1 + H_2$ is the total depth, and $\mathrm{R}_d = 30$ km. Model outputs are saved every 3 days and interval time $\Delta_t = t_f - t_i$ is 360 days.

The reference simulation is a standard freely decaying turbulence experiment (as in, e.g., Held et al., 1995; Scott, 2001; Arbic and Flierl, 2003). In addition to its simplicity, this configuration allows for spatially homogeneous turbulence statistics, which is required by our analysis of the effect of measurement errors on "observed" KE fluxes (see section

31.3.1). The model is initialized using a baroclinically unstable vertical shear, sinusoidal in the meridional direction. Small random perturbations with wavenumbers $K = 8K_1$ to $K = 10K_1$, where $K_1 = 2\pi/L_{domain}$, are also added to this background shear in order to accelerate baroclinic instability.

Figure 4a shows a time series of KE in each layer, available potential energy (APE), and total energy in the reference simulation. The onset of baroclinic instability occurs at about ~ 250 days, after which APE is progressively converted into KE. This transfer continues for a period of roughly 400 days, from which we arbitrarily select a time period on which the analysis is performed. Although fluxes depend on the specific choice of time period, results from the error analysis of next sections are independent from this choice as long as the time period is fixed (not shown). Examples of snapshots of upper layer relative vorticity at the beginning and end of this time period are shown in Figs. 4b and 4c, respectively.

To describe the depth-averaged energy budget at a given spatial scale, we first express this budget in Fourier components

$$-\frac{\partial}{\partial t}\left(\widehat{KE}+\widehat{APE}\right)+\widehat{\Pi_{KE}}+\widehat{\Pi_{APE}}+\widehat{D}=0, \tag{1.1}$$

where $\widehat{KE}$ and $\widehat{APE}$ are Fourier spectra, $\widehat{\Pi_{KE}}$ and $\widehat{\Pi_{APE}}$ are transfer functions and $\widehat{D}$ is the parameterized biharmonic dissipation. Each term of the energy budget (1) is detailed in Table 1 in Appendix A. How the depth-averaged KE spectra evolve during the considered time period is shown in Fig. 5a. Each spectrum displays the typical -3 slope of geostrophic turbulence in the direct enstrophy cascade regime (Charney, 1971). $\widehat{KE}$ increases at the largest and smallest scales of the domain, while decreasing at all other scales, indicating the presence of both an inverse and a direct energy transfer. To explain this behavior in more details we integrate each term of the energy budget (equation 1.1) over time, t, and wavenumber, K, as follows:

$$F(K)=\frac{1}{\Delta t}\int_{t_i}^{t_f}\int_{K}^{K_{\max}}\hat{F}(K')dK'dt', \tag{1.2}$$

where $\Delta t = t_f - t_i$ and $\hat{F}$ represent a term in equation (1.1). This yields an integrated spectral energy budget

$$\frac{-1}{\Delta t}(\Delta KE + \Delta APE) + \Pi_{KE} + \Pi_{APE} + D = 0, \tag{1.3}$$

where Δ indicates differences between t_f and t_i, Π indicate energy fluxes and D is the energy sink due to dissipation. Each term of this integrated spectral energy budget is shown in Fig. 5b, along with their sum (error), which shows that the budget (equation 1.3) is closed to a good accuracy. Notice that each term is multiplied by K, such that the area under the curves in Fig. 5b represents the variance [1]. In order to recover fluxes with units of $m^2 s^{-3}$ and facilitate comparisons with other studies, they will be displayed as $(2\pi R_d KH/H_1)\Pi_{KE_1}$ in subsequent figures.

The interpretation of each term in Fig. 5b depends on its role in the energy budget. For the difference terms, $-\Delta$, the interpretation is straightforward: at a given scale, K, a positive value indicates that the energy integrated over smaller scales decreased over Δt (and vice versa for negative values). For the fluxes, Π, a positive value indicates a forward transfer from larger to smaller scales (and vice versa for negative values). For both the difference and the transfer terms, local energy evolution at a certain scale K is given by the slope of the curve. A positive slope indicates an increase of energy for the difference terms, but a decrease of energy for the transfer terms (and vice versa for a negative slope).

We choose Π_{KE_1} (Fig. 5b) as our reference flux, as it shares the same essential qualitative structures than those obtained with more complex Primitive Equations (PE) models: (i) a range of negative values is observed at large scales, (ii) a range of positive values is observed at small scales, and (iii) a transition occurs around $\lambda = 2R_d$. Notice that in this model, the range of positive values results from the parametrization of sub-grid scale dissipation, as Π_{KE_1} and D almost balance each other at small scales.

---

[1] In a log-linear plot, the area under a curve is conserved when multiplying by the abscissa variable.

1.3 Effects of measurement limitations

We now systematically investigate conditions in which KE spectral fluxes can be estimated from HFRs measurements. Intuitively, we can expect that errors at large scales will arise from the geometry of the domain (limited extent, aspect ratio, non-periodicity, etc...), while errors at small scales arise from measurement limitations (resolution, noise, missing data, etc...). Together, these two limits will define the range of scales over which KE fluxes can be estimated.

1.3.1 Effects of domain geometry

For oceanic observations, which are non-periodic, estimating Fourier spectra requires the application of a window in order to reduce spectral leakage (Harris, 1978). It is also common to remove the linear trend in order to reduce spurious energy at the largest scale (Emery, 2001). The effect of windowing on non-periodic subdomains of arbitrary size 30 R_d (with horizontal resolution dx =1.95 km)is shown in Fig. 6a. In order to compare to the reference, we average fluxes obtained from overlapping subdomains that cover the entire model domain. For non-periodic subdomains, both large and small scales are affected if no window is applied (red curve). Applying a Hamming or a Hanning window reduces the errors at both large and small scales, but errors remain at small scales with the Hamming window, since periodicity is not fully enforced at the boundaries [2]. We further tested other windows such as Blackman and Kaiser-Bessel and confirm that they yield similar results to Hanning, which will be used for the remaining of this study.

The effect of the subdomain size from 30 to 10 R_d is shown in Fig. 6b. For all subdomain sizes, errors at small scales remain negligible. However, errors at large scales increase as the horizontal extent decreases. In particular, for 10 R_d, the peak of negative flux is shifted

---

[2] Hamming coefficients do not tend to zero at the boundary.

to smaller scales, without however affecting the transition scale.

Above, we have only considered squared subdomains, for which the integration in Fourier space is isotropic. How the anisotropy introduced by a rectangular subdomain affects the spectral fluxes is shown in Fig. 6c, for a fixed width of 10 R$_d$. Increasing the aspect ratio of the subdomain decreases the magnitude of the negative peak. Paradoxically, since the latter is overestimated for a squared subdomain of 10 R$_d$, increasing the aspect ratio reduces the error initially for a ratio of 2 (red curve) but increases the error for larger ratios.

1.3.2 Synthetic radar measurements

So far, we estimated spectral fluxes directly from the model data. We now investigate the effects of the various measurements limitations by mimicking radar data from the numerical model. In order to simulate the effect of the radar measurement, two fundamental steps must be followed: i) for each radar, model currents must be projected onto the radial axes of a polar grid (hereafter "current measurement"), and ii) radial currents from multiple radars must be mapped onto a common Cartesian grid (hereafter "current mapping"). This yields the two components of the surface currents, $\mathbf{u}_h = (u, v)$, from which we can compute the spectral fluxes as follows:

$$\Pi(K) = -\frac{1}{\Delta t}\int_{t_i}^{t_f}\int_{K}^{K_{max}} Re\left[\widehat{\mathbf{u_h}}^{*} \cdot \mathbf{u_h} \cdot \widehat{\nabla_h \mathbf{u_h}}\right] dK dt, \tag{1.4}$$

where $\nabla_h = (\partial_x, \partial_y)$ is the horizontal 2D gradient operator.

In order to disentangle the effects of the radar measurement from those of the domain geometry, we begin our investigation from an "ideal" but unrealistic configuration, which has the following characteristics:

— Four HFRs are monitoring the entire domain, with two on each of the south and north sides (black bullets in Fig. 4).

— The range and aperture of each HFR covers the entire domain.

— The radial resolution equals the numerical horizontal resolution of 2 km.

— The angular resolution equals $d\theta = 0.25°$.

— HFR measurements have no noise nor missing data.

In this ideal configuration, we assume that the measurements range is unlimited, allowing us to test the effect of current mapping on the doubly periodic domain. Since the aspect ratio of the radar grid cells increases with the range, this implies strong deformations away from the radar. To keep a reasonable aspect ratio at the furthest distance from each radar, we use an angular resolution $d\theta = d\theta_r L_r / L_{domain}$, where $L_r = 100$ km and $d\theta_r = 5°$ are standard HFR range and angular resolution, respectively.

Subdomains from this ideal configuration will be later considered that are meant to represent HFR stations monitoring an estuary or a coastline with offshore islands. In this latter configuration, realistic range and angular resolutions will be used. Mapping currents from HFRs requires a minimum of two HFRs at different locations, but additional HFRs monitoring a given area can improve the current mapping accuracy.

Current measurement requires averaging as HFRs perform an averaging over range and azimuth when measuring surface velocities (Ohlmann et al., 2007). Averaging depends on the range and resolution of the radar. Here in practice, the Cartesian grid of the numerical model has a finite resolution and some of the radar grid cells near the radar do not contain any Cartesian grid points. For the area corresponding to those grid points, an interpolation is needed, while an averaging is needed over the rest of the domain. In order to go around this issue, we first interpolate by nearest neighbor each component of the surface velocity onto a high azimuthal resolution polar grid centered at the HFR. The azimuthal resolution is chosen such that the grid cells furthest away from the radar have a size matching that of the Cartesian grid cells. This high resolution data is then averaged onto the radar grid with a simple azimuthal Boxcar filter. To obtain the current measurement, the averaged velocity is projected into the direction of the radar. Finally, all radar measurements are mapped onto a Cartesian grid of resolution equal to the radars radial resolution.

1.3.3 Effects of current mapping

Several methods are available to perform current mapping of the radar measurements. Figure 7 shows the effect of four standard methods on the current mapping accuracy. The methods are: a) unweighted least squares (UWLS, Lipa and Barrick, 1983), b) weighted least squares (WLS, Kim et al., 2008), c) optimal interpolation (OI, Kim et al., 2008) and d) variational interpolation (2Dvar, Yaremchuk and Sentchev, 2009). Of all the tested methods, the variational interpolation method yields the smallest errors. This method requires, however, to carefully set a number of smoothing parameters (see appendix B). In contrast, all the other methods tested require to set a single parameter (corresponding to a decorrelation scale) but yield larger errors. Among them, the OI method performs almost as well as 2Dvar, offering a good compromise between accuracy and robustness to the choice of parameters. OI also require a signal-to-noise ratio. Default signal-to noise ratio was set to 0.01.

Figure 8a shows the effect of using each of the four mapping methods on the spectral fluxes computed from (1.4). As expected from the vorticity errors shown in Fig. 7, both least squares methods introduce significant biases in the spectral fluxes. The variational method recovers almost perfectly the reference flux, followed closely by the OI method. In the following, we will now consider errors related to the "current measurement" step, choosing the variational mapping method.

1.3.4 Effects of radar resolution

We investigate the influence of measurement resolution on the energy fluxes by varying independently the radial resolution (tied with the Cartesian grid resolution) and the azimuthal resolution (Fig. 8b). As expected, the effect of resolution has very limited impact on the large scales, but induces biases at small scales. In particular, decreasing the resolution shifts the transition from positive to negative fluxes to larger scales (similarly to an averaging as in Arbic et al., 2013). This effect is observed both for decreasing the radial resolution and the azimuthal resolution independently. Larger biases are observed for combined changes in resolution.

1.3.5 Effects of measurement noise

Following Forget (2015), we mimic measurement noise by adding white noise to the radial currents obtained in our “ideal” configuration, U_{ideal}: $U_{obs} = U_{ideal} + \nu V w$, where V is the root mean square magnitude of the current, w is a random number between -1 and 1 taken from a uniform distribution, and ν sets the signal-to-noise ratio SNR = $3\nu^{-2}$.

Examples of vorticity fields for different noise levels are shown in Fig. 9. Noise mostly affects small scales, but its effects on energy fluxes spread to large scales as well (Fig. 8c). Specifically, adding noise has only a limited impact on the transition scale, but affects the amplitude of the two main lobes. In particular, the amplitude of the negative lobe is strongly decreased for a noise level above 20%.

1.3.6 Effects of missing measurements

HFR measurements are not only limited by resolution and noise, but also by gaps and by radar shutdowns, which can strongly affect the current mapping accuracy. In general, gaps in radar coverage are caused by electro-magnetic interferences, by low signal to noise ratios, and by the type of algorithm used to retrieve the signal direction (beam-forming or direction-finding).

To account for realistic gap distributions, spatial structures originating from actual radar measurements have been imposed on the synthetic radar data. An example is shown in Fig. 10a. Different gap distributions, such as the one shown in Fig. 10a, are then randomly selected for each of the four HFRs. Figure 10b shows an example of radar coverage where each Cartesian grid point is assigned a number ranging from 0 to 4, depending on the number of radial currents measurements from different HFRs falling in the Cartesian grid cell. To quantify the amount of missing data, we define a percentage of the total area covered by the radars, P. As at least two independent measurements are necessary to map the currents at a given grid point, this percentage is defined as follows: $P = 1 - (2 \times N_0 + N_1)/(2 \times M)$, where N_0 is the number of grid points with zero measurement, N_1 is the number of grid points with only one measurement and M is the total number of grid points.[3] For the example of Fig 10b, the data coverage is $P = 0.735$.

The effect of varying the area covered by the radars on the spectral fluxes is shown in Fig. 8d. As for the measurement noise, the effect of gaps is limited essentially to the amplitude of the lobes, although the transition scale is less robust to missing data (for $P <$ 70%) than to noise.

1.3.7 Effects of radar shutdowns

In addition to spatial gaps, we also consider the case of radar shutdown. To separate both effects, we assume that the available radars have no gap, while data from one or two radars are completely missing. When only one radar is shutdown, the currents are still well mapped from the measurements of the three other radars (Fig. 11a), with minimal impact on the KE flux (figure 8e).

When two radars are shutdown, the two available radars are either 1) on the same side, 2) facing each other, or 3) diagonally aligned. These configurations have different impacts on the current mapping accuracy (Fig. 11). In particular, large errors occur where the angle between the two radial directions is close to 0° or 180°, a phenomenon known as geometric dilution of precision (GDOP, Chapman et al. (1997)). GDOP is clearly visible on the cases where radars are on opposite sides of the domain, where large errors appear along the line

---

[3] Notice however that this definition is non unique as many combinations of N_0 and N_1 can lead to the same value of P.

joining the radars. When the radars are on the same side, GDOP effects are minimized on the line joining the radars but amplified away from the radars (see Fig. 11b). The effects of GDOP on the KE flux are shown in Fig. 8e. As expected, strong biases exist in the cases where the radars are on opposite sides. Fluxes are better estimated for the case where radars are on the same side since the bulk of the mapping errors are reduced by windowing near the boundaries. Notice, however, that other limitations such as missing data (resulting from e.g. insufficient range) and noise are not taken into account here, and their effects may be exacerbated when only two radars are used.

1.3.8 Combination of Errors

We now attempt to combine the above measurement limitations. Here we choose to consider only a limited set of combinations that are most likely to be relevant for the real HFR measurements. We first select a rectangular subdomain of 20 R_d in length by 10 R_d in width. The effect of this domain geometry alone (without any radar measurement effects) on the spectral fluxes is reproduced on Fig. 8f (purple curve). As shown previously, only the largest scales are affected by the domain geometry. The effect of current mapping of this subdomain using noise-free synthetic radar measurements is shown in pink. Here, biases are induced at both small and large scales, although the transition scale is still captured adequately. The addition of 30% of measurement noise and 25% of missing data adds additional biases, but still captures the transition scale (red curve). Finally, degrading the radial resolution from 2 to 6 km shifts the transition scale to larger values and increases the amplitude of the positive lobe (yellow curve).

1.4 Discussion and Conclusions

One of the main appeal of using HFR data to compute spectral energy fluxes is to identify the limit between large scale balanced dynamics and smaller scales unbalanced motions.

Here, we show that despite the introduction of significant biases in the general structure of the positive and negative lobes, the transition scale between these lobes is relatively robust to measurement limitations. The main effect comes from the HFRs resolution which shifted the transition scale to larger scales due to the implicit averaging by the radar sampling. Similar results were previously observed by Arbic et al. (2013) using a PE model to mimic the averaging performed when mapping satellite altimetric data. Nevertheless, in all cases considered in this study, this shift remained much smaller than an order of magnitude from the reference value. This suggests that the transition scale could be reasonably captured using HFR measurements.

However, our experimental design suffers from two main caveats that could modify the main conclusions of this study. First, the statistical properties of the upper layer circulation considered in our freely decaying experiments do not undergo fast variations in time, in contrast to the real ocean circulation. In practice, this implies an upper limit on the time interval that can be used for averaging. Our results using the simple idealized configuration show that the transition scale quickly converges within a factor 5 of the typical turbulent turnover timescale (not shown). This convergence could be significantly delayed or even nonexistent when considering oceanic data. The second important limitation of our configuration is the choice of a quasigeostrophic framework, which does not allow for an explicit representation of the small scale unbalanced motions. As such, the effects of measurements errors could differ when a new type of dynamics is included.

In order to evaluate the effects of the above caveats, we briefly describe results from a primitive equations model used in a regional configuration with realistic forcing[4]. Figure 12a shows a snapshot of surface relative vorticity over the gulf and estuary of Saint Lawrence. Tidal frequencies from this surface velocity fields have been removed using harmonic analysis

---

[4] The PE simulation originates from a nested high resolution (~500 m) version of the NEMO model covering the Gulf of Saint Lawrence, provided by Environment and Climate Change Canada at Dorval (personal communications with François Roy). The model is forced with open boundaries at the interface with the Atlantic and atmospheric forcing from the Global Environmental Model (GEM).

(Pawlowicz et al., 2002) to filter out the strong tidal components of the currents in the Saint Lawrence estuary. In order to compute spectral fluxes from the model data, we first select a subdomain in the lower Saint Lawrence estuary (Fig. 12b), where actual radar stations are operated (black dots, Kamli et al. (2016)). We also focus on a time period corresponding to November 2015, for which the averaged stratification yields a first internal Rossby radius $R_d \approx 7$ km. Geostrophic currents are extracted from the filtered surface fields by computing the non-divergent component via Helmholtz decomposition. Panel c shows a time-mean KE spectrum obtained using these geostrophic currents. For comparison, we also show the QG spectrum and normalize the wavenumbers of each model by their respective domain size. Both spectra yield roughly the same -3 slope. The reference flux obtained directly from the PE model geostrophic currents (red curve in Fig. 12c) shares the same qualitative structure as the one obtained from the QG model (black curve in Fig. 6a). The transition scale corresponds approximately to $\lambda = R_d/2$, four times smaller than the value obtained from the QG model. The effect of radar current mapping using radial and azimuthal resolutions corresponding roughly to those of the actual radars are shown in black and blue. The averaging performed by the radar sampling shifts the transition scale to larger values, consistent with the results obtained with the QG model (Fig. 8b). Contrary to what is shown in Fig 12d, averaging also increases the positive lobe amplitude of KE fluxes, as shown in previous studies (e.g., Arbic et al., 2013). Recall that in order to conserve the area under the curve, the fluxes are multiplied by K, which magnifies the high wavenumbers.

The results shown in Figure 12 should be viewed as a preliminary best case scenario, where only the effects of mapping and resolution are considered. A more thorough investigation including comparison with actual radar data will be presented in a subsequent study. Yet, these preliminary results suggest that it appears possible to estimate KE fluxes from HF radar measurements of surface currents over a limited range of scales. The largest scale is limited by the radars range, which can reach a few hundreds of kilometers at the lowest HF frequencies. The smallest scale is limited by the radars radial and azimuthal resolutions, and noise level. Radial resolution can reach a few hundreds of meters at the highest HF frequencies. The observable scales therefore typically range from a few kilometers to a few tens of kilometers, which fortunately corresponds to the transition scale between the direct and inverse KE cascade. However, measurements constraints introduce biases in the estimation of the positive and negative flux lobe amplitudes.

By allowing to estimate the transition scale from negative to positive fluxes in coastal areas, HFRs could be a useful tool to gain information on the observed KE budget in a range of scales relevant for the small unbalanced motions. To extend this estimation to the open ocean would however require a different type of instrument such as a spaceborne high resolution altimeter or a synthetic aperture radar. Yet, even in the best case scenario where their horizontal resolution allows for flux estimates well beyond the transition scale, these types of measurements will remain limited in their temporal resolution. We anticipate that hourly HFR measurements could be used to interpret and validate spaceborne flux estimates.

1.5 acknowledgments

Financial support to J. Clary was provided by NSERC, ISMER and Québec Océan. We thank François Roy and Simon Senneville for providing regional model data and James Caveen for his technical support. We also thank Alexei Sentchev and Max Yaremchuck for providing the 2Dvar code and Sung Yong Kim for providing the optimal interpolation code.

ANNEXE I

DEPTH-AVERAGED ENERGY BUDGET

The two layer quasigeostrophic potential vorticity equations (Vallis, 2006) are :

$$\partial_t q_1 + J(\psi_1, q_1) = A_h \nabla^4 \psi_1, \tag{1.5}$$

$$\partial_t q_2 + J(\psi_2, q_2) = A_h \nabla^4 \psi_2, \tag{1.6}$$

where the potential vorticity in each layer, q_i, is given by:

$$q_1 = \nabla^2 \psi_1 + \frac{f_0^2}{g' H_1} (\psi_2 - \psi_1), \tag{1.7}$$

$$q_2 = \nabla^2 \psi_2 + \frac{f_0^2}{g' H_2} (\psi_1 - \psi_2). \tag{1.8}$$

ψ is the streamfunction, A_h is the horizontal biharmonic viscosity coefficient, H_1 and H_2 are the layer thicknesses, f_0 is the Coriolis parameter, g' is the reduced gravity and $J()$ is the Jacobian operator.

The equation for the depth averaged energy budget is obtained by multiplying equations (1.5) and (1.6) by $(H_1/H)\psi_1$ and $(H_2/H)\psi_2$ respectively, where $H = H_1 + H_2$, and then adding them together. Applying the Fourier transform on the depth averaged energy equation yields equation (1.1), for which each term is detailed in Table 1.

ANNEXE II

2DVAR PARAMETRIZATION

Current mapping with the variational method (2Dvar) is performed by minimizing the following quadratic cost function (Yaremchuk and Sentchev, 2009, 2011):

$$J = \sum_{k=1}^{K} \left[(\hat{P}_k \mathbf{u}) \cdot \mathbf{r}_k - u_k \right]^2 + \sum_{i,j} \left[W_c (\nabla^2 \operatorname{curl} \mathbf{u})_{ij}^2 + W_d (\nabla^2 \operatorname{div} \mathbf{u})_{ij}^2 + W_u (\nabla^2 \mathbf{u})_{ij}^2 \right], \tag{1.9}$$

where K is the number of observed radial currents u_k, $\hat{P}_k \mathbf{u}$ is the interpolation operator of the 2D velocity field $\mathbf{u}$ on the observation point $\mathbf{x}_k$, $\mathbf{r}_k$ is the unit vector pointing towards the radar, and (W_c, W_d, W_u) are the weights used to enforce smoothness in the fields of curl, divergence and velocity, respectively. We parameterize these weights as:

$$W_u = \frac{K \nu^2}{2N \delta x^2}, \quad W_c = L_c^2 W_u, \quad W_d = L_d^2 W_u, \tag{1.10}$$

where ν^{-2} is the signal-to-noise ratio, N is the number of Cartesian grid points where the velocity field is mapped, δx is the Cartesian grid spacing in both x and y directions, and L_c and L_d are typical wavelengths of the curl and divergence fields, respectively. These latter scales are estimated from a preliminary mapping of the velocity field using an optimal interpolation method (Kim et al., 2008). Our weights parameterization differs from that proposed by Yaremchuk and Sentchev (2009) because we scale the typical magnitude of $\nabla^2 \operatorname{curl} \mathbf{u}$ as $U/(L_c \delta x^2)$ instead of $U/(L_c^2 \delta x)$, where U is a typical magnitude of the velocity. The main consequence of this scaling is to allow for more small scale structures to exist in the velocity field by significantly reducing the amplitude of the smoothing parameters. Data weights were set to 1 m^{-6}.

Table 1: Depth averaged spectral energy terms.

NAME	EXPRESSION
$\widehat{KE}$	$\left(H_1 \,\mathrm{Re}[\widehat{\psi_1}^* \widehat{\nabla^2\psi_1}] + H_2 \,\mathrm{Re}[\widehat{\psi_2}^* \widehat{\nabla^2\psi_2}]\right)/H$
$\widehat{APE}$	$-\frac{f_0^2}{g'H}(\mathrm{Re}[\widehat{(\psi_1 - \psi_2)}^2/2]$
$\widehat{\Pi_{KE}}$	$\left(H_1 \,\mathrm{Re}\left[\widehat{\psi_1}^* \widehat{J(\psi_1, \nabla^2\psi_1)}\right] + H_2 \,\mathrm{Re}\left[\widehat{\psi_2}^* \widehat{J(\psi_2, \nabla^2\psi_2)}\right]\right)/H$
$\widehat{\Pi_{APE}}$	$-\frac{f_0^2}{g'H}\,\mathrm{Re}\left[\widehat{(\psi_1 - \psi_2)}^* \widehat{J(\psi_1, \psi_2)}\right]$
$\widehat{D}$	$-A_h \,\mathrm{Re}\left[H_1\widehat{\psi_1}^* \widehat{\nabla^4\psi_1} + H_2\widehat{\psi_2}^* \widehat{\nabla^4\psi_2}\right]/H$

Re is the real part, $\widehat{a}$ is the Fourier transform of a and the asterisk denotes the complex conjugate.

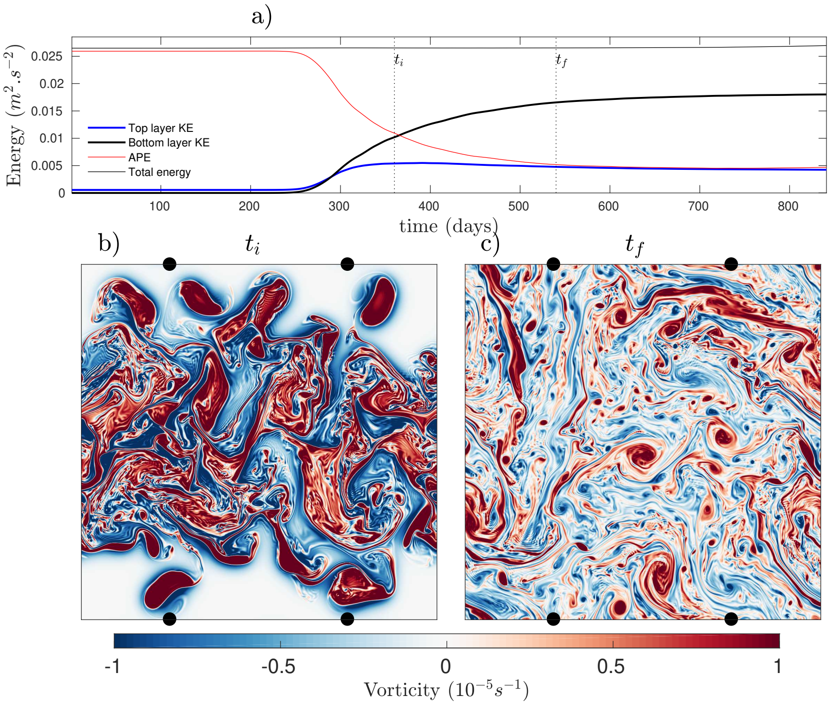

Figure 4: (a) Times series of upper layer kinetic energy (blue), bottom layer kinetic energy (thick black), available potential energy (red) and total energy (thin black). Upper layer relative vorticity at (b) t$_i$ and (c) t$_f$. Black dots represent synthetic radar positions.

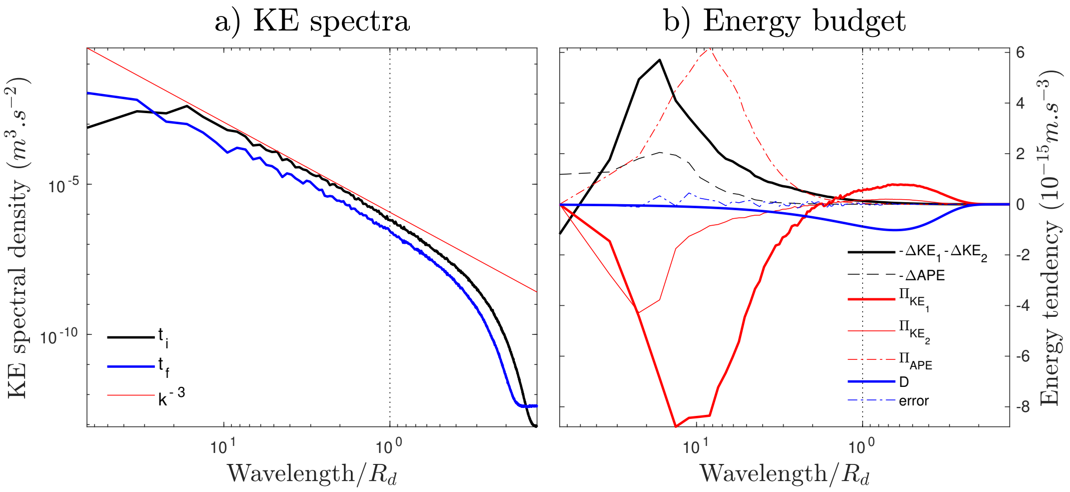

Figure 5: (a) Upper layer KE spectra at time t_i (black) and t_f (blue). (b) Spectral integral energy budget (Equation 1.3). Terms in panel b are multiplied by the wavenumber such that the area under the curves represents the variance.

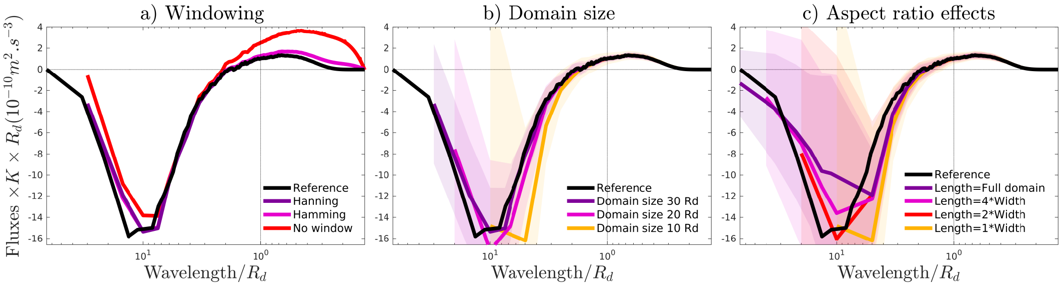

Figure 6: Effect of the domain geometry on the spectral energy fluxes. (a) Windowing effect for non periodic subdomains of size 30 R_d. (b) Effect of the size of square subdomains. (c) Effect of anisotropy for rectangular subdomains. In each panel, the reference flux of Fig. 5b is shown in black, and fluxes are multiplied by $2\pi R_d K$. Shaded areas show the standard deviations over time, between t_f and t_i .

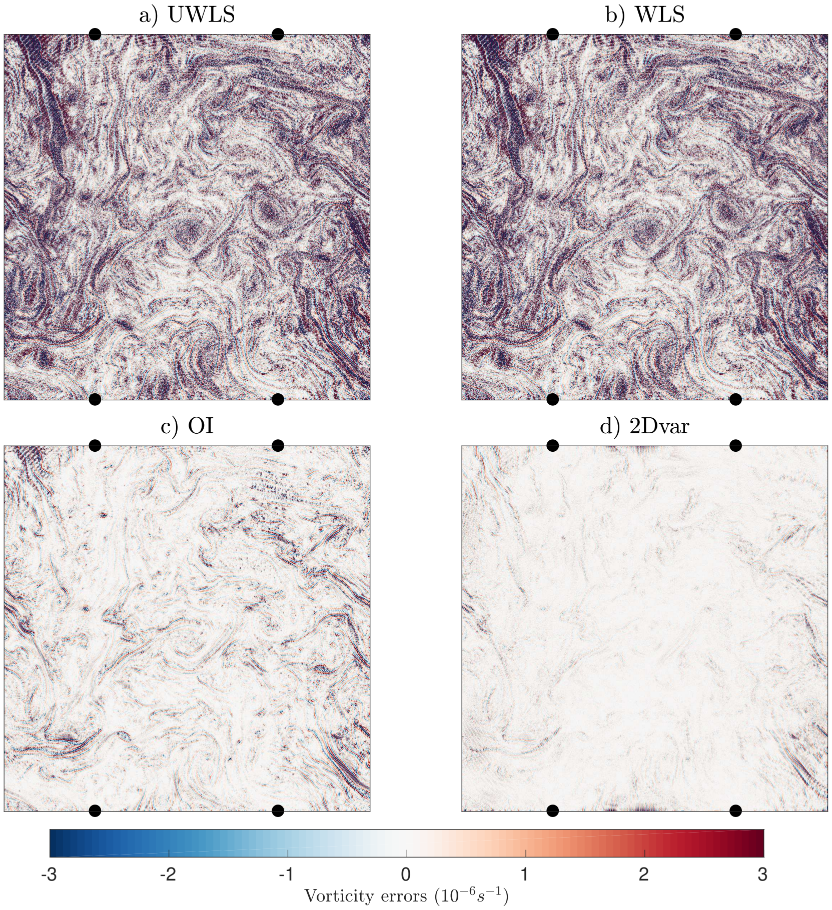

Figure 7: Errors in relative vorticity (s^{-1}) for a snapshot sampled with different mapping methods: (a) unweighted least-squares, (b) weighted least-squares, (c) optimal interpolation, and (d) variational interpolation. Black dots represent synthetic radar positions.

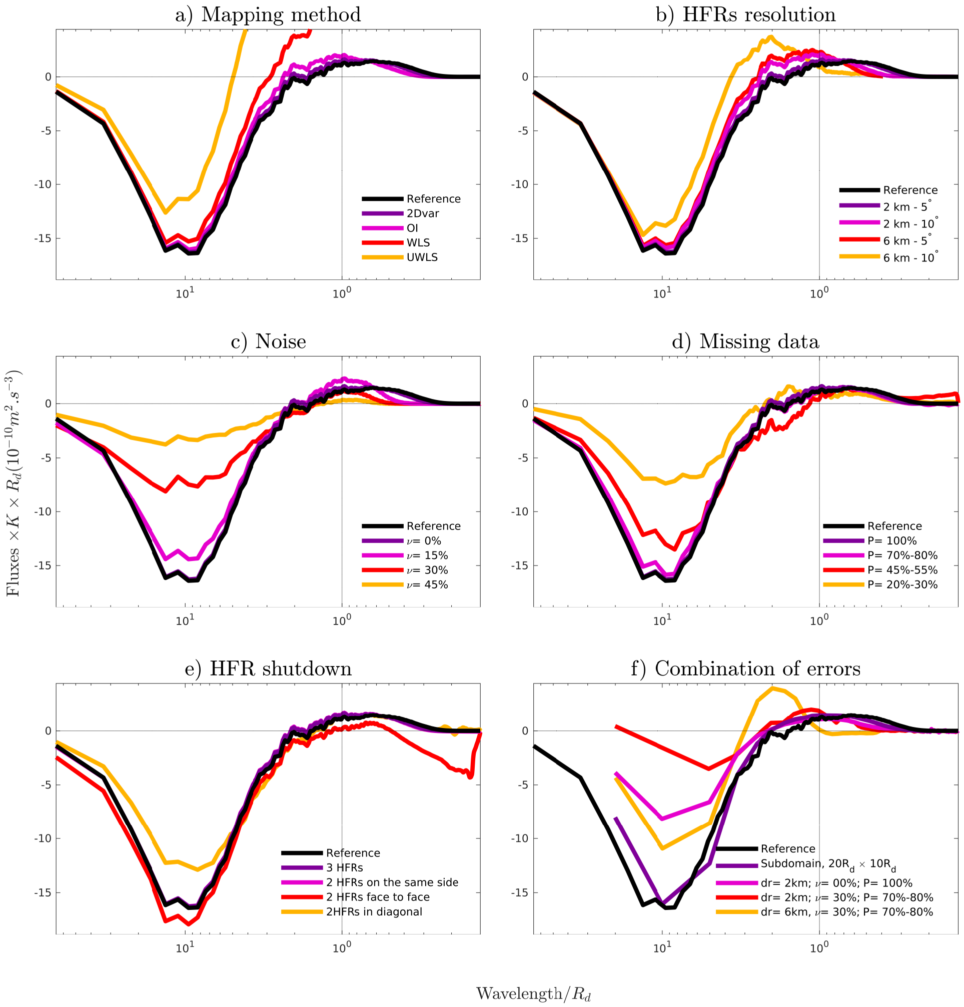

Figure 8: Effects of current measurement and mapping on the spectral energy fluxes. a) Effect of current mapping in the “ideal” configuration (see text). The 2Dvar mapping method is used for all other panels. b) Effects of radar resolution. c) Effects of measurement noise using the “ideal” resolution. d) Effects of missing measurements. e) Effects of radar shutdowns. f) Effects of measurement and mapping error combinations for subdomains of size $20\,R_d \times 10 R_d$. In each panel, the reference flux of Fig. 5b is shown in black, and fluxes are multiplied by $2\pi R_d K$.

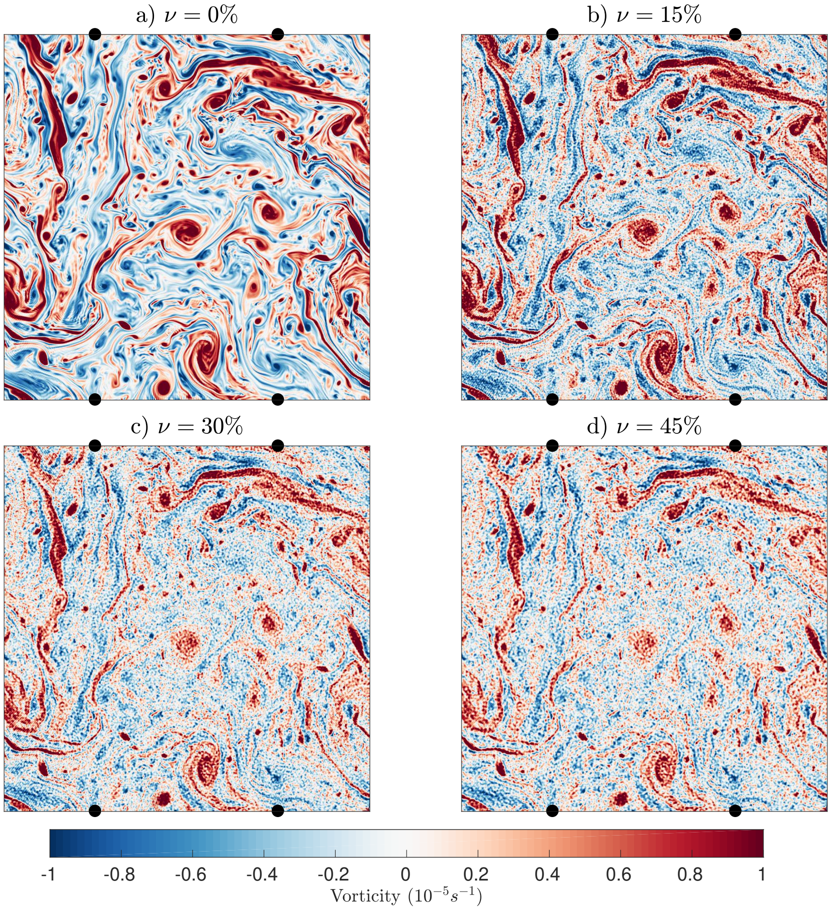

Figure 9: Measurement noise effect on relative vorticity mapping for noise levels of (a) $\nu = 0\%$, (b) $\nu = 15\%$, (c) $\nu = 30\%$ and (d) $\nu = 45\%$. Currents are mapped with the 2Dvar method.

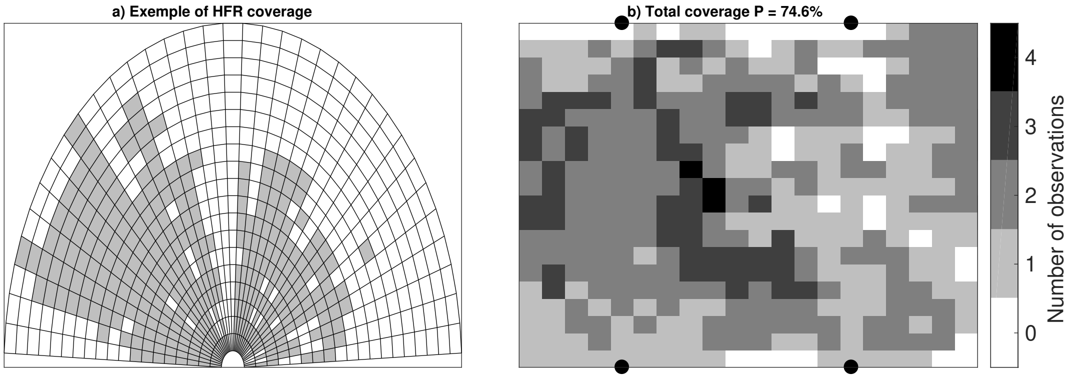

Figure 10: Example of hourly data coverage from (a) an actual HFR (CODAR station in the St. Lawrence Estuary), and (b) four synthetic HFRs with random individual data coverage similar to that shown in panel a.

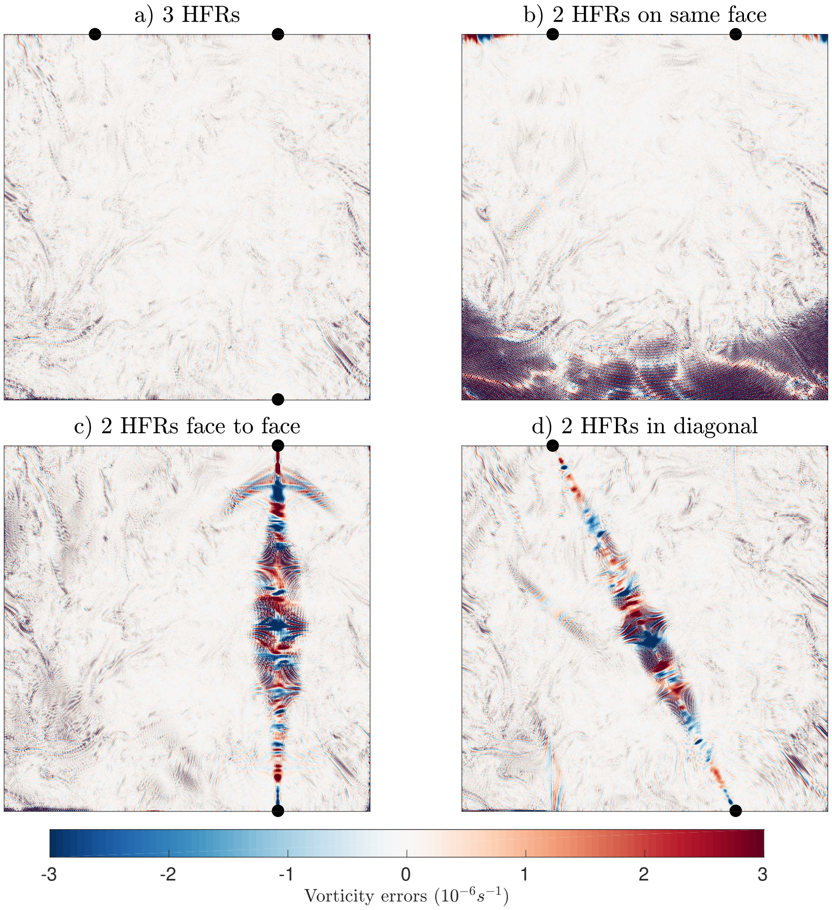

Figure 11: Errors in relative vorticity for a snapshot sampled with (a) 3 HFRs, (b) 2 HFRs on the same side of the domain, and (c, d) 2 HFRs on opposite sides. Currents are mapped with the 2Dvar method.

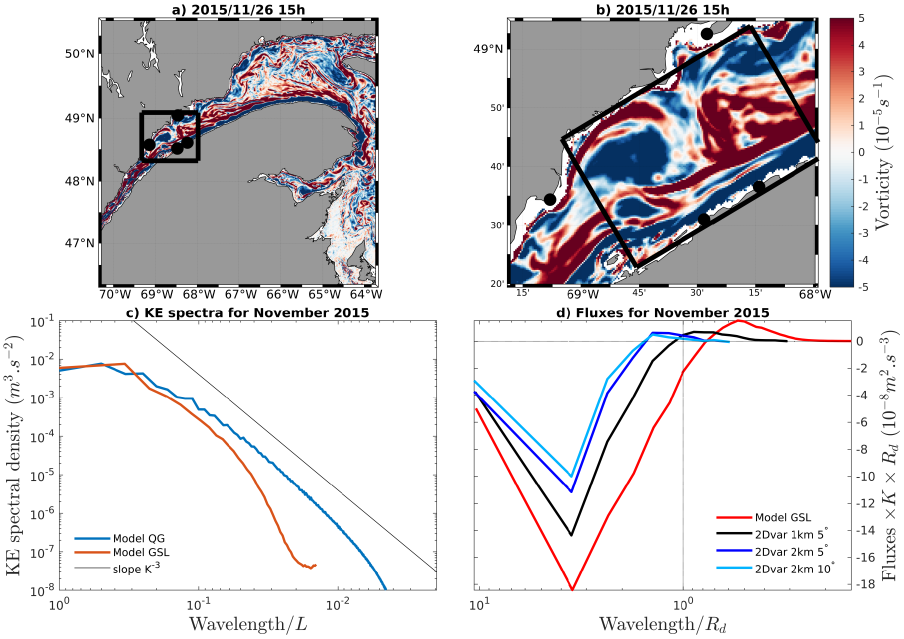

Figure 12: Results from the primitive equations model simulation in a regional configuration (GSL run). (a) Example of a snapshot of detided surface relative vorticity in the estuary and the gulf of Saint Lawrence. Black dots show the positions where actual HFRs are operated. (b) Zoom in the black rectangle region of panel a. The white rectangle shows the area used for the analysis. (c) Time averaged KE spectrum using the geostrophic currents from the GSL run for the month of November 2015 (red). The spectrum is compared to that of the QG model at time t_f (blue). Wavelength are normalized by each model domain size. (d) Effect of radar resolution on the reference KE flux of the GSL run (red). Fluxes are obtained from noise-free synthetic HFR measurements at various radial and azimuthal resolutions (black and blue).

ARTICLE 2

JUSQU'À QUEL POINT LES FLUX SPECTRAUX DE KE PEUVENT-ILS ÊTRE ESTIMÉS À PARTIR DE MESURES RADARS?

Ce deuxième article *How well can surface KE spectral fluxes be estimated from HFRs?* doit être très prochainement soumis à Journal of Atmospheric and Oceanic Technology. Il reste quelques éléments de discussion à reformuler. L'idée principale est de tester les conditions de mesures des radars sur une circulation plus réaliste que celle du modèle QG. Nous considérons aussi les erreurs d'angles des mesures HFRs, qui ont été formulées pour la première fois en 2019 pour des radars en direction-finding. Le modèle numérique utilisé possède une résolution horizontale de 500 m et provient d'Environnement Canada. Le résultat essentiel est que les erreurs de mesures impactent surtout les courants divergent, ce qui fausse les flux spectraux du courant divergent et les transferts de KE dû aux interactions entre le courant divergent et le courant rotationnel. Imposer des seuils d'acceptation sur les mesures et moyenner en temps aident à atténuer partiellement les effets de ces erreurs sur les flux spectraux. Le moyennage en temps doit se faire en évitant de filtrer la dynamique hors équilibre.

Résumé en français

La distribution des flux spectraux est fortement asymétrique, et elle sélargit à mesure que les erreurs s'accumulent. Les biais dans les flux spectraux du courant divergent contaminent les interactions entre courant rotationnel et courant divergent car les flux sont non linéaire

Dans notre précédente étude (Clary et al., 2019), nous montrons la possibilité, avec un modèle QG, d'estimer les transfert d'énergie cinétique entre les subméso-échelles et les

méso-échelles en utilisant des radars à haute fréquence. Dans cet article, nous élargissons l'étude en utilisant un modèle régional aux équations primitive dans l'estuaire du bas Saint-Laurent, où quatre radars sont en fonctionnement depuis 2013. Les courants du modèle et les courants observés sont décomposés en courant de marées, en courant rotationnel sans marées et en courant divergent sans marées. Le courant rotationnel sans marées sert de proxy au courant en équilibre, alors que la somme du courant divergent sans marées et du courant de marée correspond au courant hors équilibre. Les flux de référence sont estimés pour tous les types de courants, ainsi que leur interactions non-linéaire. Les mesures synthétiques sont obtenus à partir des simulations en reproduisant les conditions de mesures par les radarsà haute fréquence (absence de données et erreurs d'angles). Les flux obtenus à partir des mesures synthétiques sont comparés aux flux de référence afin de déterminer la résilience des flux aux limitations des mesures. Contrairement aux courant rotationnel, les courants divergent sont très sensibles aux erreurs de mesures, ce qui affecte fortement l'estimation des flux de KE du courant divergent. Les flux de KE du courant total sont dominés par les interactions entre le courant en équilibre et le courant hors équilibre. Ces flux de KE du courant total sont donc fortement affectés par les erreurs de mesures. Ces résultats expliquent en partie les différences entre les flux simulés et ceux observés. Par conséquent, il est nécessaire d'observer avec précision les courant divergent avant de pouvoir les utiliser pour l'estimation des flux de KE dans les régions côtières ayant de fortes dynamique hors-équilibre.

ABSTRACT

In a previous study (Clary et al., 2019), the possibility of estimating the ocean's surface kinetic energy transfers between mesoscale and submesoscales from observations by high-frequency radars was investigated using idealized quasi-geostrophic numerical simulations. Here, this possibility is further investigated using a realistic simulation from a regional primitive-equations model in the lower Saint Lawrence estuary, Canada, where four high-frequency radars have been operated since 2013. Both simulated and observed surface current fields are decomposed into detided rotational and divergent components, plus a tidal component. The detided rotational component is taken as a proxy for balanced motions, while the detided divergent and tidal components account for the unbalanced motions. Reference fluxes are extracted from the simulation for all components as well as their nonlinear interactions. Synthetic measurements are obtained from the simulation by mimicking radial currents measured by the four high-frequency radars with the observed measurement errors (gaps in the data coverage and direction-of-arrival errors). Fluxes obtained from the synthetic data are compared to the reference fluxes in order to assess the robustness to the measurement limitations. Contrary to rotational currents, divergent currents are particularly sensitive to measurement errors, which strongly affect the estimation of the weak divergent KE fluxes. Total KE fluxes are dominated by the nonlinear interactions between the balanced and unbalanced motions, and are therefore also strongly affected by measurement errors. These results explain the discrepancies obtained between the reference simulated fluxes and the observed fluxes. It therefore appears necessary to accurately resolve the current divergence with high-frequency radars before they can be used to estimate spectral KE fluxes in coastal areas featuring strong unbalanced dynamics.

2.1 Introduction

In Clary et al. (2019, hereinafter CNC19), the possibility of estimating spectral kinetic energy (KE) fluxes from observations of surface currents by high-frequency radars (HFR) was investigated using numerical simulations. Synthetic HFR measurements were obtained from a quasigeostrophic (QG) simulation of freely decaying turbulence for which the reference spectral KE flux is characterized by a transition from positive values at small scales to negative values at large scales, the transition occurring at roughly twice the Rossby deformation radius R_d. Fluxes obtained from the synthetic data were compared to the reference flux in order to assess the robustness to various measurement limitations, such as the nonperiodicity of the observational domain, the finite horizontal resolution of the instruments, measurement noise and missing data. The transition scale between the positive and negative fluxes was found to be relatively robust to those measurement limitations, despite their causing significant biases in the amplitude of the fluxes.

While these results suggest that it appears possible to estimate spectral KE fluxes from HFR measurements of surface currents over a range of scales encompassing the transition scale between positive and negative fluxes, HFRs are mostly installed along coastlines, and coastal ocean dynamics are not in QG balance. CNC19 presented some preliminary results using synthetic HFR measurements obtained from a primitive-equations simulation of the Gulf of Saint Lawrence encompassing an area in the lower Saint Lawrence estuary monitored by four HFRs since 2013 (Kamli et al., 2016). Focusing on the nondivergent component of the detided currents, they showed that the surface KE fluxes transitioned from positive to negative values at a scale of $0.8R_d$, about 2.5 times smaller than the value obtained from the QG model. The finite horizontal resolution of the instruments resulted in a shift of the transition scale to larger values ($\sim 1.5R_d$).

Here, we further investigate the effects of HFR measurement limitations on the estimation of spectral KE fluxes using synthetic data obtained from the primitive-equations simulation of the Gulf of Saint Lawrence used by CNC19. In addition to the effects of the finite horizontal resolution of the instruments, we also investigate the effects of realistic measurement noise and missing data taken from actual observations from the four HFRs installed in the lower Saint Lawrence estuary. One of the major sources of error in HFR measurements is the uncertainty in the estimation of the direction of arrival (DOA) of the signals backscattered by the sea surface toward the radar (Emery and Washburn, 2019). We also investigate the effects of realistic DOA errors estimated from the two HFRs (CODAR Seasondes) installed on the south shore of the lower Saint Lawrence estuary. Contrary to CNC19, we do not focus on the nondivergent component of the detided currents, but consider the contributions of both the divergent and nondivergent components of the detided currents, as well as the tidal currents, and their interactions, to the total surface KE fluxes. Spectral KE fluxes obtained with the synthetic data are finally compared with those obtained from the actual HFR observations.

The numerical simulation, HFR data, and the decomposition of currents into different components are detailed in section 2.2. Results are presented in section 2.3. Finally, section 2.4 offers some discussions and conclusions.

2.2 Methods

2.2.1 Numerical model

The ocean model results were taken from a NEMO (http://www.nemo-ocean.eu) simulation on a 500 m resolution horizontal grid. The domain extends from the western extremity of the Saint Lawrence estuary (west of Île-d'Orléans) to Belle-Isle and Cabot straits. The vertical grid has 75 vertical levels with a resolution near the surface of about 1 m. The bathymetry was built based on the latest available data from the Canadian Hydrographic Service. Except for the details described herein, the NEMO model setup and parameters are the same as described in Paquin et al. (2020). The model is spun up from rest on November 1st 2014 and run until October 20th 2017. The first 2 months of data were discarded to allow the simulation to adjust to the boundary conditions and forcing. The initial temperature and salinity fields were taken from the operational 5 km resolution Gulf of St. Lawrence system (Smith et al., 2013). The daily Saint-Lawrence River runoff was prescribed at the western boundary using results from Lefaivre et al. (2016). Tides prescribed at the eastern boundaries were computed from the Oregon State University Tidal Prediction Software (Egbert and Erofeeva, 2002). Temperatures and salinities were prescribed at the eastern boundaries from the global ocean prediction system described in (Smith et al., 2018). The 2.5 km resolution atmospheric forcing came from the operational system described in Milbrandt et al. (2016).

A subset of the model domain encompassing the Gaspé current is shown in Figure 13a. We restrict our analyses on a smaller subdomain where HFRs have been operating since 2013 (see boxes in Figure 13a and b). This area features a combination of internal tides, mesoscale features (Ingram and El-Sabh, 1992), freshwater input (Mertz, 1989; Koutitonsky et al., 1990). Internal gravity waves are also expected (Mertz and Koutitonsky, 1992). The Rossby radius of deformation ranges from 6 km to 10 km in the subdomain during the 3-year model run.

2.2.2 High-frequency radars

Four HFRs were deployed in the lower Saint Lawrence estuary in late 2012 (Fig. 13b): two Coastal Ocean Dynamics Application Radar (CODAR) Seasondes on the south shore at Pointe-aux-Père (C1, 48.52°N 68.47°W) and at Sainte-Flavie (C2, 48.5°N 68.47°W), and two Wellen Radars (WERA) on the north shore at Pointe-à-Boisvert (W1, 48.57°N 69.13°W) and at Pointe-aux-Outardes (W2, 49.04°N 68.46°W). The characteristics of the HFRs are given in Table 2.

Different techniques for estimating the DOA of radial currents are used: direction finding for CODARs and beamforming for WERAs. Radial currents for CODARs were computed using the processing toolbox developed by Brian Emery (Emery, 2018), based on the Multiple Signal Classification (MUSIC) algorithm (Schmidt, 1986). Antenna patterns measured on September 09, 2016 were used for reprocessing the data for the year 2015 to 2017 for both CODARs. Radial currents were output in 1 degree directional bins. Radial currents for WERAs were computed using the software developed by Klaus-Werner Gurgel (Gurgel et al., 1999), based on the beamforming technique with an array of 12 receiving antennas. For each WERA site, beamforming patterns were calculated with an ultra-spherical window and using positions of the antennas measured with an accuracy $\sim$ 1 cm with a differential Global Positioning System (GPS). Phase differences due to receiving cables were calibrated on October 22 (for W1) and 23 (for W2), 2012, and were used for processing the data since 2013. Radial currents were output on a polar grid with 1° azimuthal spacing, although this does not correspond to the azimuthal resolution of beamforming since the width of the beams is typically much larger ($> 10^\circ$).

All measurements were carefully quality controlled (see Annexe III), and radial currents were averaged over 3 hours and within 4° azimuth bins to reduce noise and fill data gaps. The 3-hour temporal averaging was chosen to resolve the semi-diurnal tidal variability while reducing noise as much as possible. The standard CODAR azimuthal averaging within 10° bins ($\pm 5^\circ$) was deemed too large since it yields a grid cell size of 9 km at 50 km range, which is the same order as the Rossby radius of deformation.

2.2.3 Energy budget diagnostics

From a simplified perspective, the model's surface currents can be thought of a combination of balanced and unbalanced motions. Given their nonlinear interaction, it can be arduous to design a simple filter to extract each component and multiple methods have been suggested (McWilliams, 1985; Capet et al., 2008c; **?**).Here, we remove diurnal frequencies using harmonic analysis (Pawlowicz et al., 2002) and semi-diurnal frequencies with an 11h to 13.5h bandpass filter. Harmonic analysis is not advised for semi-diurnal tides as they are partially non-coherent. The detided currents are then further decomposed into rotational ($\mathbf{u_{rot}}$) and divergent ($\mathbf{u_{div}}$) components ($\mathbf{u_{nt}} = \mathbf{u_{rot}} + \mathbf{u_{div}}$) via a Helmoltz decomposition. The total surface current is then given by:

$$\mathbf{u} = \mathbf{u_{rot}} + \mathbf{u_{div}} + \mathbf{u_t}. \tag{2.1}$$

An example of such a decomposition is given in Fig. 13c-f. Detided rotational current (panel e) show local Rossby number higher than one (colors are saturated at ±1) and dominate detided non-rotational current as well as tidal currents. Here, we define the balanced component as the detided rotational contribution and the unbalanced component as the addition of the detided non-rotational contribution and the tides.

From the KE budget, the only term that can redistribute kinetic energy between spatial scales is the triad interaction term, defined as :

$$T(\mathbf{u}, \mathbf{u}, \mathbf{u}) = \widehat{\mathbf{u}^*}.\mathbf{u}.\widehat{\nabla_{\mathbf{h}}\mathbf{u}} \tag{2.2}$$

As total currents is decomposed into balanced and unbalanced currents $\mathbf{u} = \mathbf{u_{bal}} + \mathbf{u_{unb}}$, transfer can be rewritten as :

$$\begin{aligned} T(\mathbf{u}, \mathbf{u}, \mathbf{u}) = & T(u_{bal}, u_{bal}, u_{bal}) + T(u_{unb}, u_{unb}, u_{unb}) + \\ & T(u_{bal}, u_{bal}, u_{unb}) + T(u_{bal}, u_{unb}, u_{unb}) + T(u_{bal}, u_{unb}, u_{bal}) + \\ & T(u_{unb}, u_{unb}, u_{bal}) + T(u_{unb}, u_{bal}, u_{bal}) + T(u_{unb}, u_{bal}, u_{unb}) \\ & = T_{bal} + T_{unb} + T_{interactions} \end{aligned}$$

Where

$$T_{interactions} = T(u_{bal}, u_{bal}, u_{unb}) + T(u_{bal}, u_{unb}, u_{unb}) + T(u_{bal}, u_{unb}, u_{bal}) + \\ T(u_{unb}, u_{unb}, u_{bal}) + T(u_{unb}, u_{bal}, u_{bal}) + T(u_{unb}, u_{bal}, u_{unb})$$

As the transfer T reveal the source and sinks of KE at a given wavenumber, the KE passing through a wavenumber K from the higher wavenumber is then defined by the spectral KE flux :

$$\Pi(k) = -\int_{k}^{k_{\max}} T dk \tag{2.3}$$

As total currents is decomposed into balanced and unbalanced currents, the KE spectral flux at a given waveenumber k can be rewritten :

$$\Pi_{tot}(k) = \Pi_{bal}(k) + \Pi_{unb}(k) + Interactions. \tag{2.4}$$

Where the $Interactions = \int_{k}^{k_{\max}} T_{interactions} dk$ is the integral of the transfers due to balanced-unbalanced interactions.

2.3 Results

2.3.1 Reference kinetic energy fluxes

Before investigating the effects of measurement errors from HFRs on the estimation of spectral KE fluxes, we first need to characterize the simulated fluxes and their variability. Figure 14 shows the spectral KE fluxes from the total model currents. Shadings indicate the distribution of fluxes over the whole model run of 3 years, which displays a high variability.

In order to extract a reference flux at a given wavenumber, one can either choose the mean (white line) or the median (solid black line). However, they can differ by a factor of two, resulting from the skewness of the distribution. Thereinafter, we choose to show the median as it is not affected by extreme values, and we characterize the variability of fluxes with their 25th and 75th percentiles (dashed lines).

We investigated the sensitivity of the median value and the variability of fluxes to the averaging period. A minimum period of 3 months is required in order for the fluxes distribution to converge (not shown), allowing to resolve the seasonal cycle of fluxes. However, as will be shown in the next section, measurement errors cause significant discrepancies between simulated and observed KE fluxes. We therefore focus on the effect of measurement errors on yearly averaged fluxes for simplicity.

Figure 15a shows the model total KE spectrum (black line) corresponding to the median flux shown in Figure 14. The total KE spectrum has a slope of k^{-3} typical of the QG direct enstrophy cascade for wavelengths between roughly 4 and 20 km. However, the expected transition to a $k^{-5/3}$ slope at smaller scales due to internal waves (Callies et al., 2015, e.g.) is not observed, suggesting that the dissipative range occurs before this transition in this model. The spectra of the different components of the decomposition described in (2.1) are also shown in Fig. 15a. The rotational component dominates at scales above roughly 4 km, below which all components become comparable, as is expected from the Helmholtz decomposition for the rotational and divergent components (Callies et al., 2014). Although our study area is located in an estuary, tides do not dominate the KE spectrum at any scale.

The median fluxes of the different components are shown in Fig. 15c (tide-detided decomposition) and Fig. 15e (balanced-unbalanced decomposition). Shadings corresponding to the 25th and 75th percentiles show the large variability for all components and their interactions. On average, total KE fluxes are positive, corresponding to a transfer of KE from larger to smaller scales. Most previous numerical studies on the topic have neglected tides. Here, the middle panels show that although tidal contributions to the total KE fluxes in isolation are negligible, their nonlinear interactions with detided currents explain about half of the total KE fluxes. When tidal currents are combined with the detided divergent component to account for the unbalanced motions, they remain negligible compared to the total KE fluxes. Interestingly, the detided rotational component explaining the balanced motions is also negligible, and the bulk of the total KE fluxes is due to the nonlinear interactions between the balanced and unbalanced components. Although being negligible, the signs of the balanced and unbalanced fluxes are as expected : (i) for the balanced motions, fluxes transition from negative values at large scales to positive values at small scales, and (ii) for the unbalanced motions, fluxes are positive at all scales. In view of their weak amplitude and large variability, it seems pointless to focus on either of these two components in isolation. We thus focus on the total KE fluxes thereinafter.

2.3.2 Effects of measurement limitations

Following CNC19, we investigate the effects of three major measurements limitations on the estimation of KE fluxes by mimicking HF radar observations using the simulated currents. The three measurement limitations are: (i) the limited horizontal resolution, (ii) missing data, and (iii) DOA errors. The first two limitations were explicitly investigated by CNC19 using a QG simulation. We revisit them here using a realistic primitive-equations simulation, and also consider the important limitation of DOA errors, which are a major source of HFR measurement errors (Emery and Washburn, 2019). We briefly explain our procedure to produce synthetic HFR observations from the numerical simulation, and refer the reader to CNC19 for more details. Model currents are first interpolated by nearest neighbor onto a high resolution polar grid centered on each HF radar, and projected onto the radial axes to obtain radial currents, which are then averaged on a lower resolution polar grid (1.5 km in range and 1° in azimuth) to obtain synthetic ideal HF radar measurements. Finally, the latter are mapped onto a common Cartesian grid of 2 km resolution using a 2D variational algorithm. CNC19 showed that this algorithm avoids introducing significant mapping errors on fluxes other than the errors caused by the limited horizontal resolution inherent to the HF radars measurements.

The right panels of Fig. 15 show the KE spectra and fluxes obtained using the currents mapped from the synthetic ideal HF radar measurements. The main effects of the limited horizontal resolution on KE spectra are a reduction of rotational KE and an increase of divergent KE at scales smaller than 10 km, causing an artificial dominance of divergent motions at scales smaller than 7 km. The main effects on KE fluxes are a slight reduction of fluxes amplitudes and a shift of the positive peaks to slightly larger scales (e.g. from 10 to 15 km for the total KE fluxes), consistent with previous studies (Arbic et al., 2013).

However, these synthetic ideal HFR measurements are not representative of real HF radar measurements, which are affected by missing data and noise. Missing data in radar coverage can be caused by electromagnetic interferences, by low signal-to-noise ratios, by radar shutdowns, and by the type of algorithm used to retrieve the signal direction (beam-forming or direction-finding). Figure 16 shows the spatial and temporal coverage of our four HF radars for the whole month of December 2015. For all radars, the data return decreases with increasing distance from the radar. Furthermore, for the direction-finding radars (C1 and C2), the data return decreases for some particular azimuth sectors associated with distortions of the receive antenna patterns (Lipa et al., 2006). For all radars, the data return also strongly varies with time (panel e). Some of this variability is due to variations in the atmospheric forcing of Bragg waves (Kamli et al., 2016). To assess the effect of missing data on spectral KE fluxes, a mask was generated for each observed radial current map, with a value of 1 for existing data and a value of not-a-number (Matlab way of flagging missing data) for missing data. The synthetic ideal HFR measurements obtained from the numerical simulation were then multiplied by the masks corresponding to the same Julian time in each model year. To avoid strongly distorted 2D current fields mapped from insufficient radial current data, we discard results obtained with less than 70% of the total area covered by the HFRs, as defined in CNC19.

An important source of errors that was not explicitly considered by CNC19 are DOA errors. For beamforming radars, DOA errors can be caused by phase differences between receiving antennas that are not properly calibrated (e.g. Flores-vidal et al., 2013), and by beamforming side-lobes that could mix strong signals coming from the dominant Bragg waves direction with weaker signals from the main lobe coming from a different direction. While the former effect can be minimized by carefully calibrating phase differences between receiving antennas, as done for our WERAs, the latter effect is inevitable and depends on the coastal geometry and wind conditions. DOA errors for beamforming radars are therefore difficult to evaluate. For direction-finding radars using the MUSIC algorithm, DOA errors are mostly caused by distortions in the receive antenna patterns (Lipa et al., 2006; Emery and Washburn, 2019). For our CODARs, DOA uncertainties, σ_θ, and biases, θ_b, are estimated with the toolbox developed by Brian Emery (Emery, 2018). The DOA error, θ_e, is then defined as the euclidean norm of the DOA uncertainty and bias: $\theta_e = (\sigma_\theta^2 + \theta_b^2)^{1/2}$. The spatial distributions of DOA errors averaged over the year 2015 for both CODARs are shown in Fig. 17 (upper panels), and histograms of hourly DOA errors are shown in the bottom panels. The majority of DOA errors are smaller than 5°, but stronger DOA errors are found in particular azimuth sectors.

To assess the effect of DOA errors on spectral KE fluxes, we add to the DOA of each synthetic radial current a random error taken from a Gaussian distribution centered on θ_b with a standard deviation of σ_θ [1]. As θ_b and σ_θ were not estimated for the WERAs, we generated random DOA errors using θ_b and σ_θ estimated for the CODARs. This also meant we had to use the missing data distribution of the CODARs to synthesize the radial currents for the WERAs. So the effects of measurement errors on spectral KE fluxes obtained here are more representative of a configuration with 4 CODARs rather than our actual configuration of 2 CODARs and 2 WERAs.

---

[1] We also tested using a random error taken from a uniform distribution with the same standard deviation, which yielded similar results.

Before showing the effects of the various measurement errors on spectral KE fluxes, we first show in Fig. 18 the effect of gaps and of DOA errors on raw data (i.e. before averaging). Because of DOA errors, azimuthal averaging can propagate misplaced currents. Then, figure 19 is an example of the effects of the various measurement errors on the divergence of the surface currents for the same time shown in Fig. 13. Fig. 19a shows the effect of the limited horizontal resolution of the HFRs, yielding a low-resolution version of the high-resolution divergence field shown in Fig. 13f, without much distortion. Fig. 19b shows the additional effects of missing data, causing significant distortions in both the amplitude and pattern of the divergence field. Fig. 19c shows the additional effects of DOA errors, causing further distortions of the divergence field. These additional distortions were reduced by removing data with DOA errors stronger than 5° (filtered DOA errors, Fig. 19d), but the distortions due to missing data remained. In contrast, the rotational field was much less affected by the measurement errors (not shown).

Finally, the effects of the various measurement errors on spectral KE fluxes are shown in Fig. 20 for the balanced (panel a) and unbalanced (panel b) components, their interaction (panel c), and the total currents (panel d). The reference fluxes (in purple) are the low-resolution fluxes shown in Fig. f, and correspond to the fluxes that would be obtained by ideal HFR measurements. The effects of missing data are shown in pink, and the additional effect of DOA errors are shown in orange. For the balanced fluxes, the main effect of measurement errors is to shift the transition scale from positive to negative fluxes to slightly larger values (from 12 to 18 km). For the unbalanced fluxes, the main effect of measurement errors is to shift the positive peak to larger scales, while the positive peak of the interaction fluxes remains at the same scale but gets weaker. For the total fluxes, the positive peak both shifts to larger scales and gets weaker. Surprisingly, there is not much additional distortion of the median fluxes caused by the DOA errors, but there is a noticeable increase in the spreading of the distribution for the unbalanced fluxes.

2.3.3 Comparison with observations

We now compare the simulated and observed KE spectra and fluxes. Simulations and observations cover the 2015 to 2017 period. KE spectra for the different current components of Eq. (2.1) are compared in Fig. 21. The simulated and observed total KE spectra have the same energy level and slopes at scales larger than roughly 10 km, but the observed KE becomes weaker than the simulated KE at smaller scales, possibly due to the horizontal smoothing caused by the 2D variational mapping. A similar comparison is observed for the detided rotational and tidal KE, although the observed energy level is also weaker than that simulated at the largest scale for the latter, possibly due to the 3-h temporal averaging of the observed currents. The observed KE of the divergent detided currents is, however, stronger than that simulated for scales larger than 9 km, a consequence of the distortions of the divergence field caused by the measurement errors, as illustrated in Fig. 19.

Spectral KE fluxes are compared in Fig. 22. The distributions of the simulated and observed KE fluxes have similar spreading (except for the unbalanced fluxes), but different skewness, resulting in different median fluxes. While the simulated median total fluxes are positive at all scales, the observed median total fluxes are negative at scales larger than 20 km. This is not due to the median balanced fluxes, which are close to zero at all scales, but is rather due to the median unbalanced fluxes, and the median interaction fluxes, which are both negative at scales larger than 20 km, contrary to those simulated, which are both positive at all scales. The spreading of the observed unbalanced fluxes is larger than that simulated, and skewed toward negative values at scales larger than 20 km due to the distortions of the divergence field caused by the measurement errors. As a result, the fluxes of the interactions between the balanced and unbalanced motions are also biased, and since they dominate the total fluxes, the latter are biased as well.

2.4 Discussion and conclusion

The original motivation for this work and that of CNC19 was to estimate spectral KE fluxes from HFR observations to identify the limit between large-scale balanced dynamics and smaller-scale unbalanced motions. CNC19 showed that the transition scale between the positive and negative fluxes of the rotational motions is relatively robust to HFR measurement limitations, which cause a shift of the transition scale to slightly larger values. Here, we confirm this result, even when considering the important source of measurement noise due to DOA errors, which was not explicitly taken into account by CNC19. However, we show that in the particular coastal area investigated here (the lower Saint Lawrence estuary), the detided rotational motions (our proxy for the balanced motions) are a negligible contribution to the total KE fluxes, which are dominated by the nonlinear interactions between the balanced and unbalanced motions (Fig. 15e). To estimate the total KE fluxes, it is therefore necessary to accurately estimate both the balanced and the unbalanced motions. Unfortunately, the latter are dominated by the divergent component of the current field, which is highly sensitive to HFR measurement errors (Fig. 19). Consequently, the weak KE fluxes associated with the unbalanced motions are strongly affected by measurement errors (Fig. 20b), which in turn strongly affect the total KE fluxes (Fig. 20d). These results are confirmed by comparing the KE fluxes obtained from the ideal synthetic HFR observations (assumed noise-free and without missing data) with those obtained from real HFR observations (Fig. 22). The observations indeed fail to properly estimate median KE fluxes associated with the unbalanced motions, and therefore also fail to properly estimate median total KE fluxes. It is worth mentioning that the observed median KE fluxes associated with the balanced motions are closer to zero than the simulated fluxes, which have weakly negative values at scales larger than 20 km, but those median values are negligible compared to the spread of the fluxes distributions, which are similar for the observed and simulated balanced fluxes.

It therefore appears necessary to accurately resolve the current divergence with HFR measurements before they can be used to estimate spectral KE fluxes in coastal areas like the lower Saint Lawrence estuary, where the ocean dynamics are not in QG balance but rather feature strong unbalanced dynamics. We have shown that DOA errors can be mitigated by estimating them directly from the data and removing data with DOA errors larger than a certain threshold (5° was used here). An estimation of DOA errors has recently been proposed by Emery and Washburn (2019) for direction-finding HFRs, but such an estimation is still lacking for beamforming HFRs. Another important source of errors for accurately resolving the divergence field are missing data. Spatial gaps in HFR observations are more frequently obtained with direction-finding HFRs than with beamforming HFRs. The standard procedure for reducing spatial gaps is temporal and azimuthal averaging. The former causes a loss of temporal resolution while the latter causes a loss of spatial resolution. For estimating spectral KE fluxes at submesoscales, the loss of spatial resolution should be minimized, and we averaged our observations over 4° azimuth bins rather than the standard 10° bins typically used by CODAR Seasondes operators. The loss of temporal resolution may be problematic in coastal areas featuring significant tidal motions, such as the lower Saint Lawrence estuary. Although KE fluxes associated with tidal motions alone were negligible, the fluxes due to nonlinear interactions of tidal and non-tidal motions were a significant contribution to the total KE fluxes (Fig. 15c). In coastal areas with weak tidal motions, the temporal averaging could be increased to further reduce measurement noise and missing data, as long as the dominant unbalanced motions are not filtered out. It remains to be seen how well the divergent motions can be resolved in such conditions. It also remains to be seen how bathymetry influence the KE spectral fluxes distribution.

2.5 acknowledgments

We acknowledge the Fonds de recherche du Québec Nature et technologies (FRQNT), the Marine Environmental, Observation, Prediction and Response Network (MEOPAR), and Canada Economic Development for Quebec Regions for their financial support of the HFRs acquisition, installation and maintenance. Financial support to J. Clary was provided by

NSERC, ISMER and Québec Océan. We thank François Roy and Simon Senneville for providing regional model data and James Caveen for his technical support. We thank Alexei Sentchev and Max Yaremchuck for providing the 2Dvar code. We also thank Brian Emery for providing the code allowing the estimation of DOA uncertainties. This work is a contribution to the research program of Québec Océan.

Table 2: HFRs characteristics.

	CODAR		WERA	
	C1	C2	W1	W2
Radio frequency (MHz)	12.5	13.5	16.15	
Radio bandwidth (kHz)	100		100	
Radial resolution (km)	1.5		1.5	
Integration time (min)	12.8		15	
Receive antennas	3-elements colocated		12 monopoles	
Direction of arrival (method)	MUSIC		Beamforming	

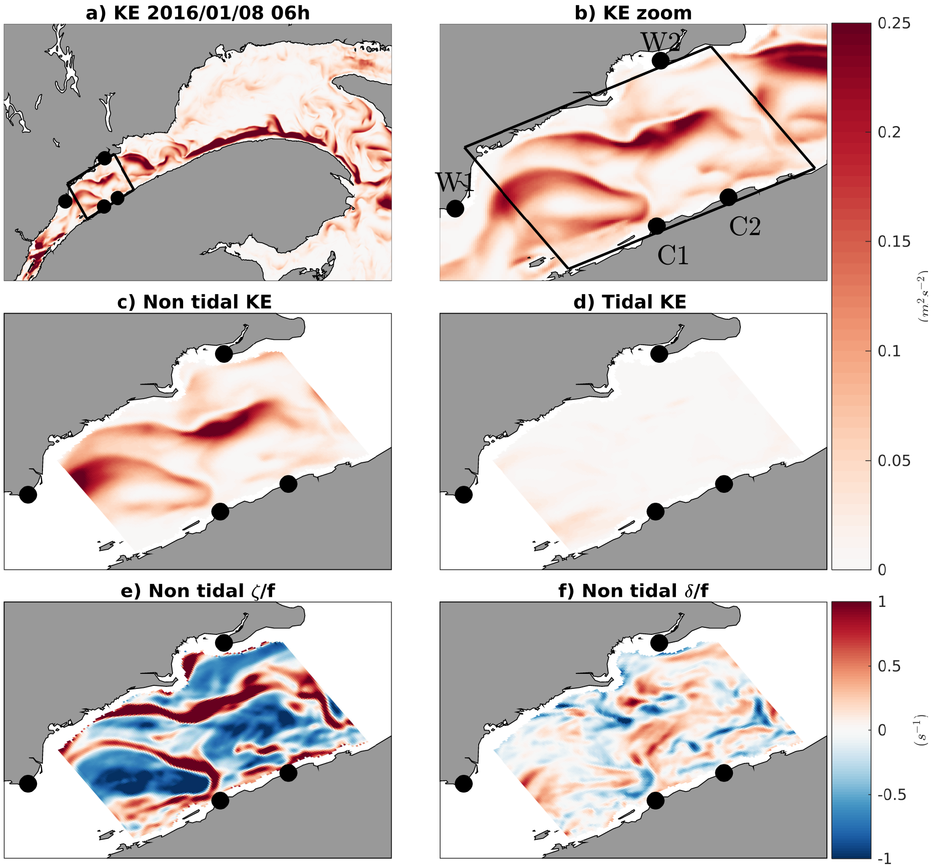

Figure 13: Example of currents decomposition from PE model. Black dots represent the HFR positions.

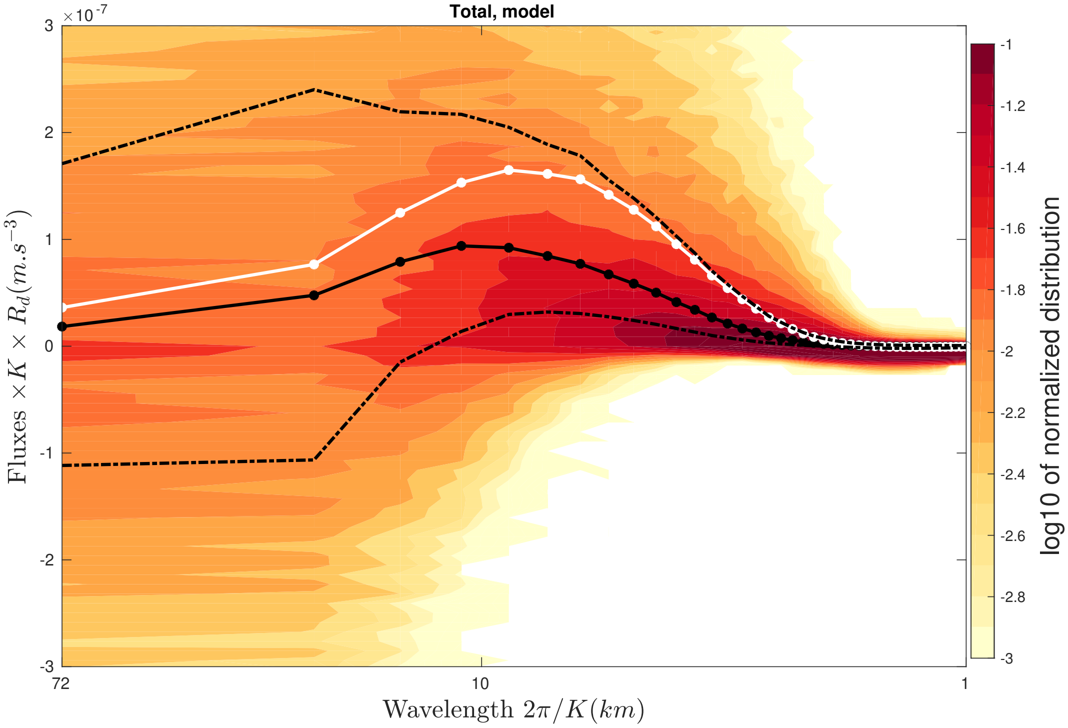

Figure 14: Spectral distribution of GSL model total currents. White line is the average, black line is the median and the two black dashed lines are the 25 and 75 percentiles. The normal distribution hypothesis is not valid here.

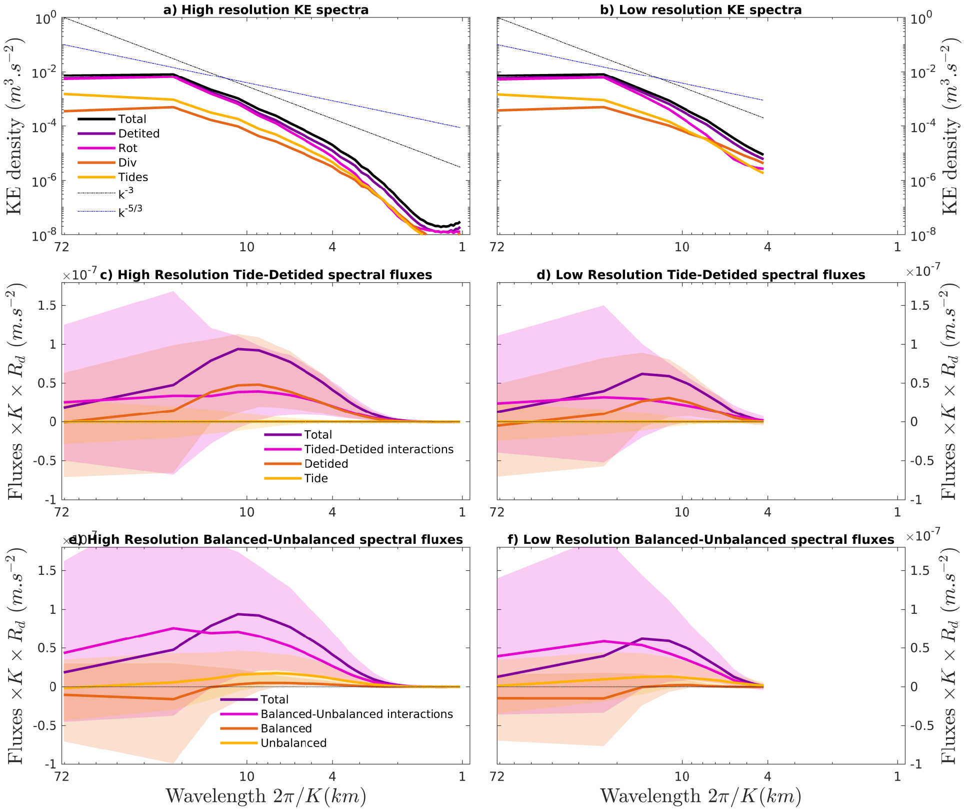

Figure 15: (upper panels) KE spectra at .5 km resolution (left panel) and 2 km resolution (right panel). (middle panels) KE spectral fluxes at .5 km resolution (left panel) and 2km resolution (right panel) for Tide-Detided current decomposition. (lower panels) Same as middle panel but for Balanced-Unbalanced current decomposition. For example, the rotational KE spectral flux is the rotational self-interaction (see section 2.2.3).

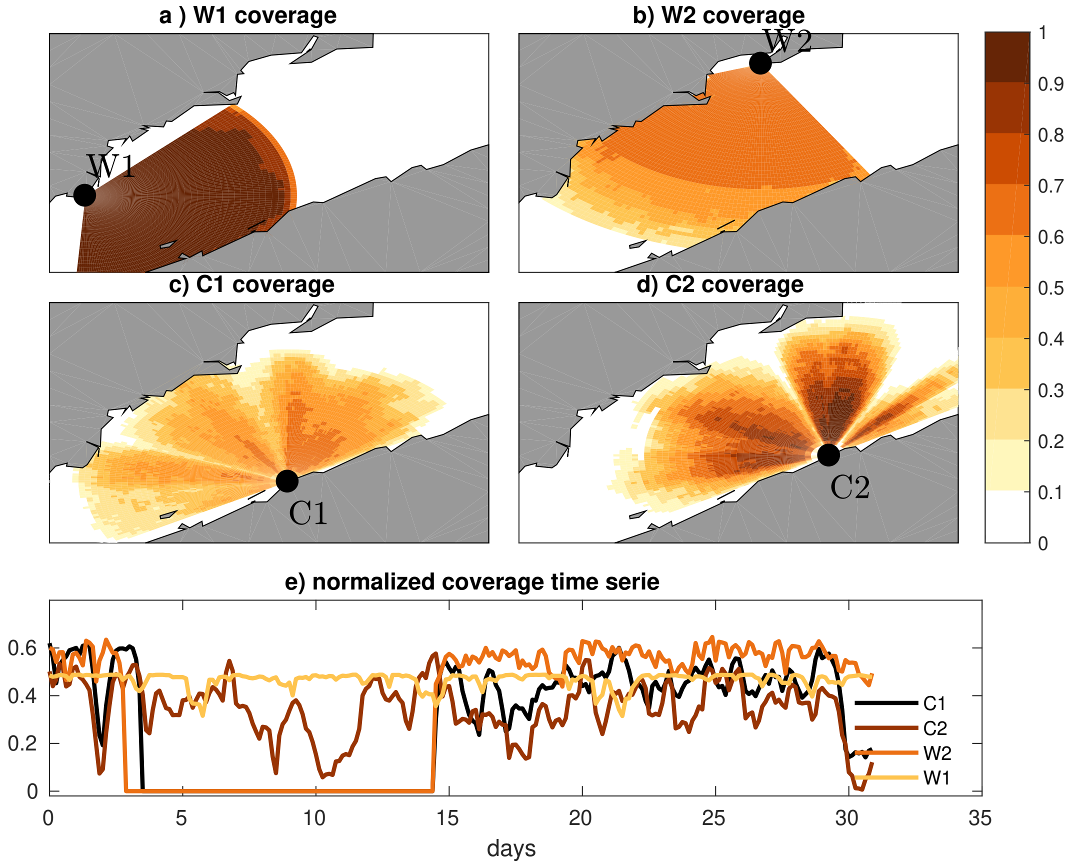

Figure 16: Example of 3 hour averaged measurements coverage in December 2015

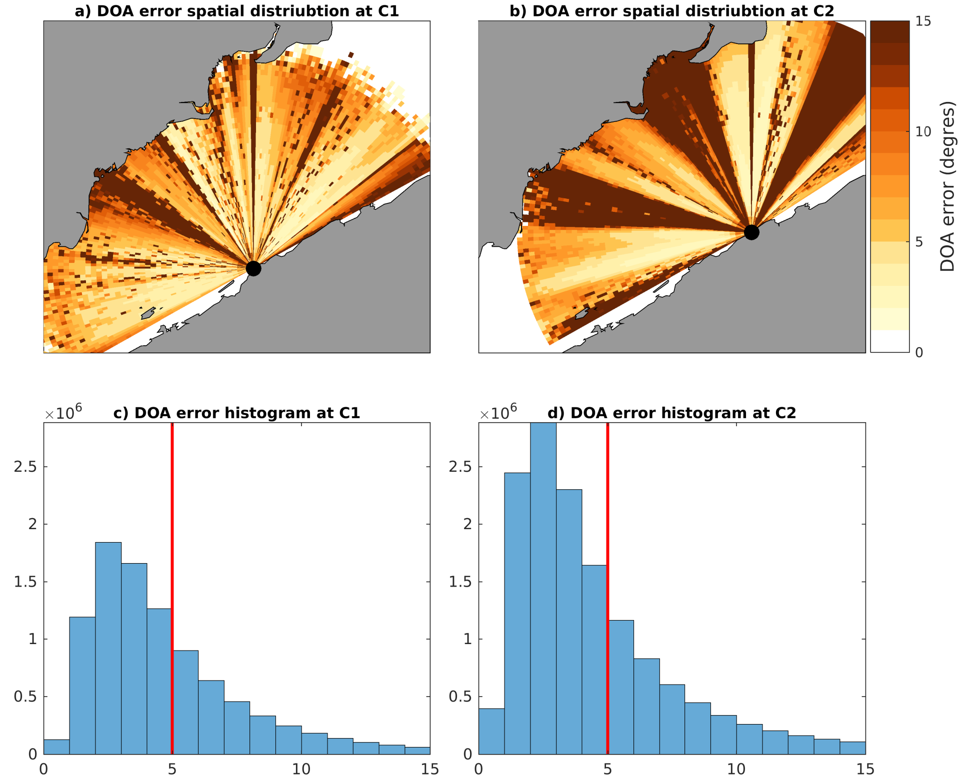

Figure 17: (upper panel) DOA error on year 2015 for the two codars. (lower panel) histogram of DOA errors. DOA error is the norm of DOA uncertainties and DOA biases.

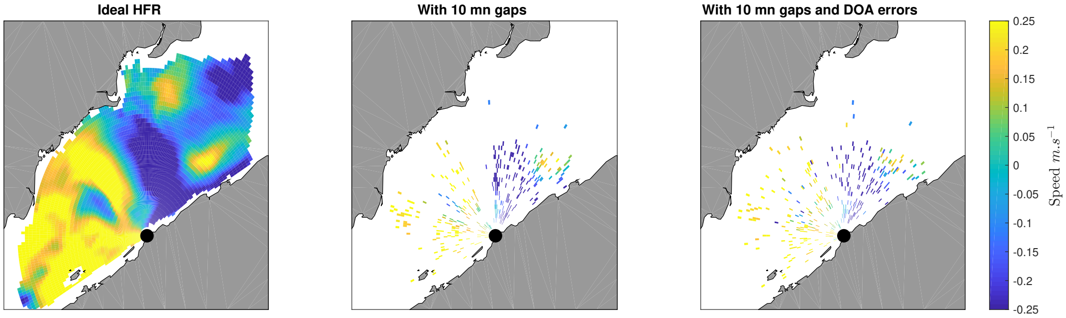

Figure 18: Example of gap and of DOA error effects on synthetic HFR measurements before azimuthal and time averaging.

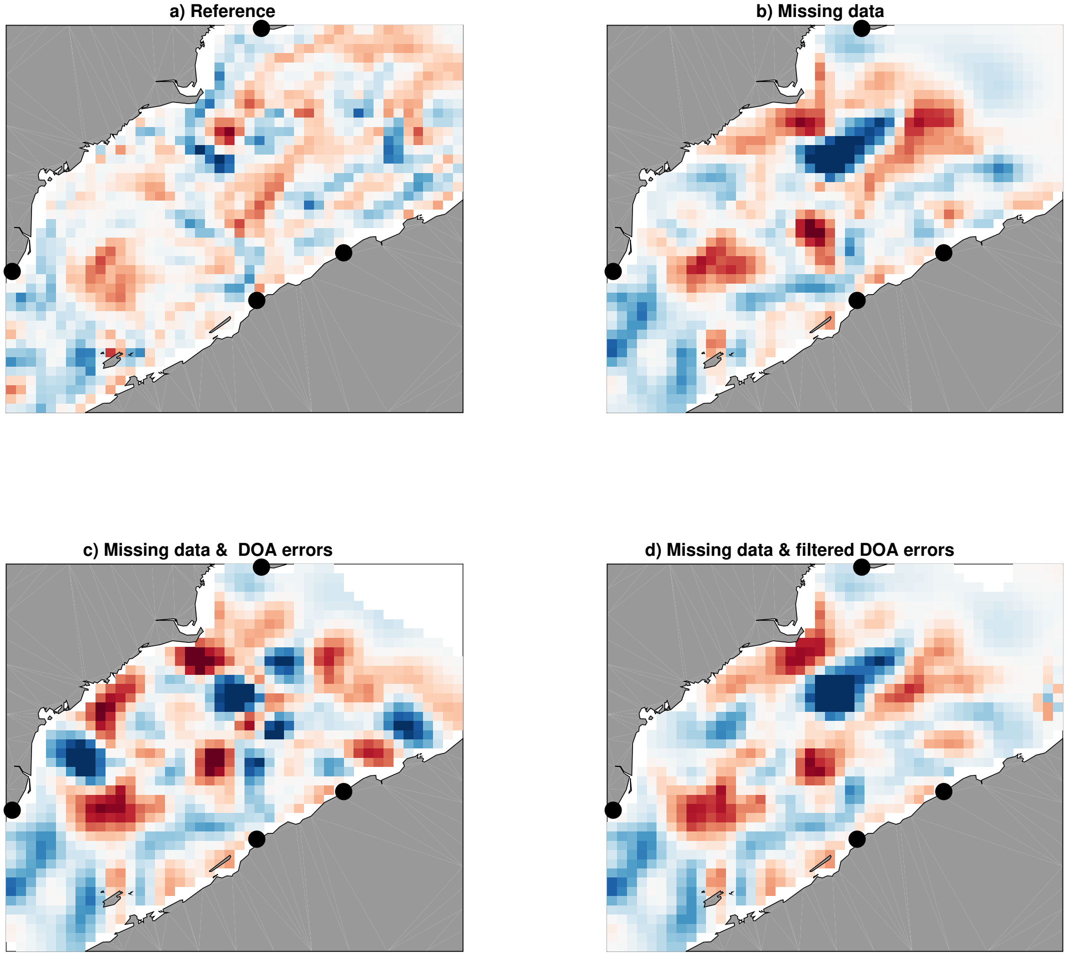

Figure 19: Flow divergence at the same date as in figure 13 computed with the following scenarios : (a) low resolution reference (b) missing data and noise (c) missing data, noise and DOA errors and (d) missing data and filtered DOA errors. The difference in the divergence field between (a) and (b) come from the low presence in data ($P = 0.5$). DOA errors significantly change the divergence field (c) and filtering those errors significantly reduce they create (d). Black dots represent synthetic HFRs positions.

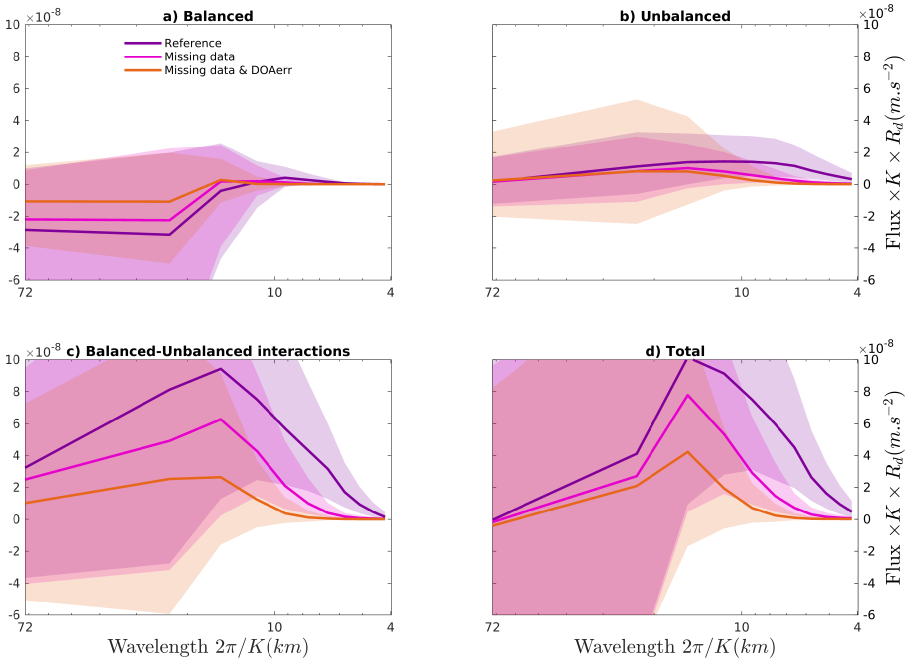

Figure 20: Missing data and DOA errors on KE spectral fluxes for (a) balanced self-interactions (b) unbalanced self-interactions (c) balanced-unbalanced interactions and (d) total currents self-interactions. A colored line is the median and a shaded area is the $25\% - 75\%$ percentile area around the median.

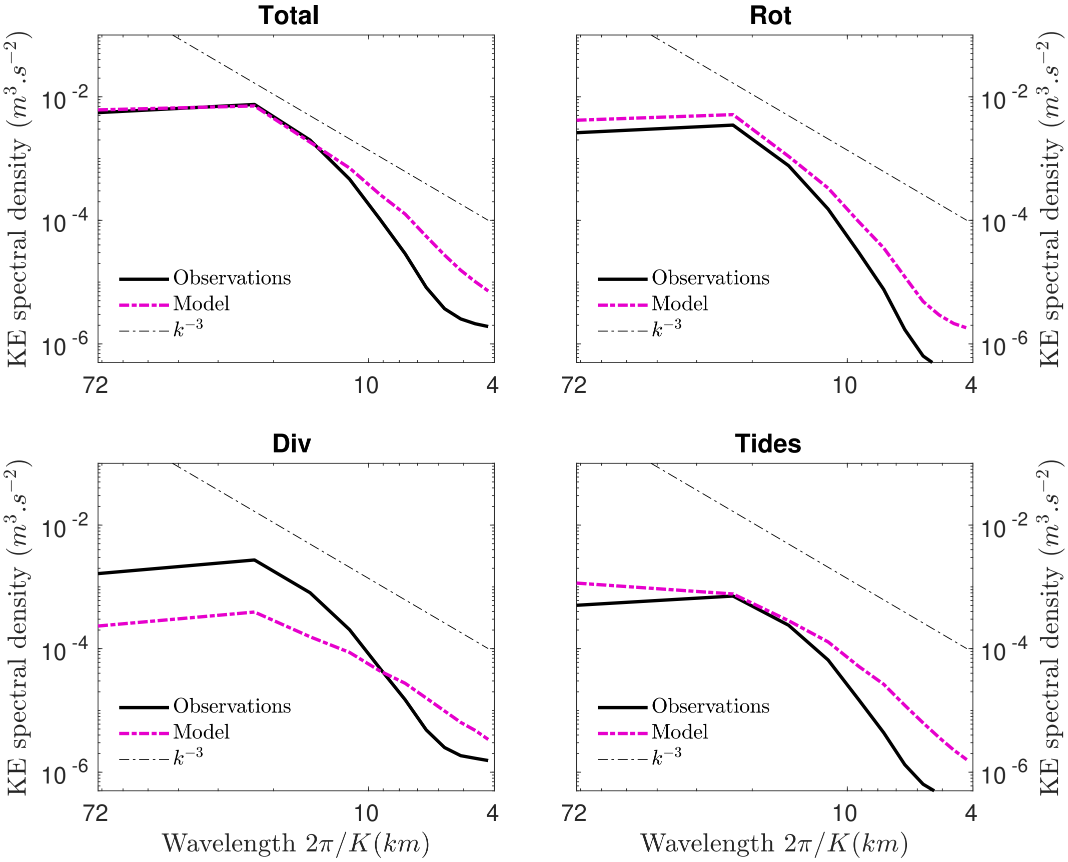

Figure 21: KE spectra from observations and from GSL model degraded at a 2 km resolution in the LSLE.

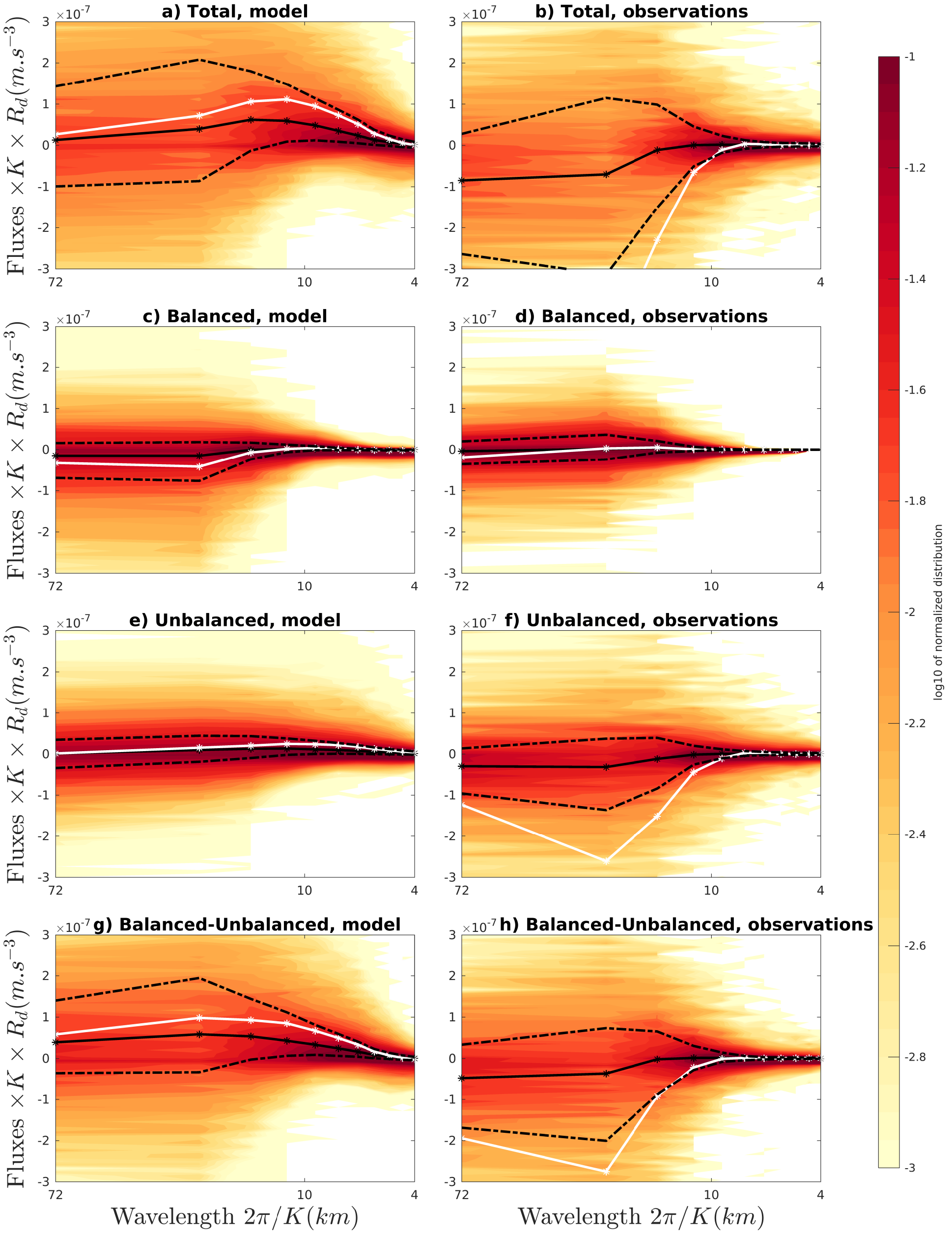

Figure 22: Comparison of spectral distribution between (left) GSL regional model and (right) real observations.

ARTICLE 3

DYNAMIQUE DE SURFACE OBSERVÉE ET MODÉLISÉE DANS LE LSLE

Dans le précedent chapitre, nous montrons notre incapacité èstimer correctement les flux spectraux de KE.

Résumé en français

Dans ce chapitre *Modelled and observed surface dynamics in the LSLE* nous cherchons à mieux comprendre les processus responsable de la dynamique aux subméso-échelles dans la région détude. Dans ce but nous regardons la variabilité saisonnière des courants et des grandeurs liées. Nous comparons modèle régional et observations HFRs. Essentiellement, nous notons la présence des marées semi-diurne, l'absence de pic d'énergie près de la fréquence de Coriols et l'absence d'ondes d'inertie-gravité aux hautes frqences.

ABSTRACT

Here, we compare the surface dynamic in the LSLE obtained from HFRs measurements and from a regional model. Main features shared by the model and the observations are the presence of a semi-diurnal tides, the absence of high frequnecy inertial-gravity waves and the absence of a near inertial peak.

3.1 Introduction

Oceanic variability involves a whole family of ocean dynamics that can be classified by spatial and temporal scales. The attention received by the mesoscale in the past decades was favorized by the development of altimeters. Those scales are characterized by small Rossby number. By contrast, submesoscale are characterized by $O(1)$ Rossby number and horizontal scales smaller than the first baroclinic Rossby deformation radius R_d (Thomas et al., 2008). Submesoscales (approximatively smaller than 50 km in the open ocean) are the bridge between the well known mesoscales and the smallest scales (where dissipation takes place). The traditional quasi-geostrophic theory that apply to the mesoscales is not adapted to the submesoscales as they are partly three-dimensional. Filaments, fronts and local upwelling and downwelling are some examples of submesoscale dynamics that break the geostrophic balance. Their generation mechanisms are described through frontogonesis (associated with mesoscale eddies), baroclinic instabilities (associated with the mixed layer) or wind forced buoyancy loss (Thomas et al., 2008; Callies et al., 2015). Dynamics of scales larger than the deformation scale are fundamentally different from those of the smaller scales. In a large picture, scales larger than R_d (~ mesoscales) experience an inverse cascade of KE whereas scales smaller than R_d (~ submesoscales) experience a direct cascade. In particular, strain induced frontogenesis is a source of unbalanced (~ divergent) KE as an unbalanced circulation is created to counteract frontal intensification and to preserve cross-front geostrophic balance (Hoskins and Bretherton, 1972; Klein et al., 2008; Capet et al., 2008b). However, some submesoscale processes are characterized by an inverse cascade, modifying the main circulation (Lévy et al., 2010, 2012b). Energy pathways in the submesoscales are only partially known through numerical studies (Vanneste and Yavneh, 2004; Molemaker et al., 2005, 2010; Scott and Arbic, 2007; Scott et al., 2011; Vanneste, 2013; Nikurashin et al., 2013; Xie and Vanneste, 2015; Taylor and Straub, 2016) but still need to be quantified with in situ and direct observations.

Actual estimation of KE spectral fluxes from observations rely on satellite altimeters (Scott and Wang, 2005; Arbic et al., 2012, 2013, 2014; Khatri et al., 2018). However, satellite altimeters observe part of the mesoscales and cannot see the submesoscales. Their true resolution is the distance between two tracks (around 100 km, latitude depending). Aviso (a data product from satellite altimeters) are unable to resolve submesoscale variablity because the distance between two tracks is higher the than Rossby deformation radius. Unresolved eddies and the mapping procedure tendency to merge smaller eddies into larger ones (Amores et al., 2018) surely bias the estimation of KE spectral fluxes. It is probably the reason why Scott and Wang (2005) found a transition scale around 150 km. Even the next generation of altimeters will be limited to resolution higher than 30 km because of noise issues (Gómez-Navarro et al., 2018). The observational requirements to capture the submesoscales cannot be achieved by altimetry as they need a spatial resolution of $O(1)$ km and a temporal resolution of $O(1)$ hour. Those requirements are however fullfilled with high frequency radars (HFRs). A direct estimation of KE fluxes has been recently attempted using coastal surface currents from HFRs (Soh and Kim, 2018).

In our two first papers we used a QG and a regional model to investigate conditions in which KE spectral fluxes can be estimated from HFR measurements (Clary et al., 2019, 2021). The goal is to have some insight in the susbmesoscale activity. The next section describes the area of study, quality control, data cleaning, gap filling and mapping processes. A description of the GSL regional model is given in Clary et al. (2021). The third section's goal is to gain some insights on the observed circulation by looking at the seasonal characteristics of the modelled and of the observed circulation. Total currents are dynamically decomposed in the fourth section, where similar analysis is performed for the regional model and for the HFRs observations. Discussion (unfinished) is in the fifth section.

3.2 Material and method

3.2.1 Area

The studied area is the lower Saint-Lawrence estuary (LSLE). This channel has a length of 200km, a width of 30km to 60km and an approximate depth of 300m. The Rossby radius, about 5-10km (Mertz et al., 1988, 1990) is much smaller than the LSLE width, permitting the existence of mesoscale phenomena such as coastal jets, baroclinics eddies and mesoscales unstable waves (Mertz et al., 1990). LSLE is also submitted to geophysical forcings, e.g. tides (Koutitonsky et al., 1990; Koutitonsky and Bugden, 1991) and winds (Koutitonsky and Bugden, 1991; Mertz and Koutitonsky, 1992; Ingram and El-Sabh, 1992). Tides and winds are the main sources of energy for mixing in the ocean (Wunsch and Ferrari, 2004). LSLE is also submitted to freshwater input (Mertz, 1989; Koutitonsky et al., 1990) and to seasonal ice coverage. LSLE is characterized by strong seasonal features. In winter, the estuary water masses are composed of two layers : a cold surface layer and a deep layer (saltier and warmer). The partial ice coverage can impact HFRs measurements quality and quantity (Kamli et al., 2016). For the rest of the year, LSLE is stratified into three layers. In spring, the important income of freshwater, due to the watershed defrost, push downward the winter surface layer. It leads to the formation of the cold intermediate layer (Koutitonsky and Bugden, 1991; Saucier et al., 2003; Cyr et al., 2011, CIL). The formation of the CIL is common in subartic coastal seas. The CIL in the LSLE is fueled by the one formed in the Gulf of St.Lawrence. The consequence is a strong vertical shear as the CIL is advected toward the Saguenay (Galbraith, 2006), i.e. in the opposite direction from that of the surface layer. The CIL is mainly eroded by vertical diffusion in summer and fall (Cyr et al., 2011). The bottom layer is saltier and warmer than the CIL. The vertical configuration in temperature and salinity promote the developement of baroclinic instabilities. Summer is characterized by a strong near surface stratification and by the existence of an anticyclonic circulation downstream of the LSLE (Koutitonsky et al., 1990).

Four HFRs were deployed in late 2012. The two CODARs were deployed on the south shore at Pointe-aux-Père (PAP, 48.52°N 68.47°W) and Sainte-Flavie (STF; 48.5°N 68.47°W) The two WERAs were deployed on the north shore at Pointe-à-Boisvert (PAB, 48.57°N 69.13°W) and at Pointe-aux-Outardes (PAO, 49.04°N 68.46°W).

3.2.2 Data quality control

HFRs remote sensing is based on the back scattering of electromagnetic waves from the conductive rough sea surface. Radial velocity is deduced from Doppler frequency shift computed over an acquisition of many chirps, while distance is obteained from frequency difference between the received and the transmitted radio signals during a chirp. However, the bearing is more complicated to determine. At t present two kinds of HFRs are commonly used, CODARs and WERAs. CODARs can only operate in direction finding whereas WERAs can operate in direction finding or in beamforming.

3.2.2.1 CODARs

The CODAR SeaSonde is a is compact system with two crossed loops antennas and a monopole antenna (N=3), meaning that a maximum of two bearings (N-1) can be determined with Codars. Possible bearings are determined with the help MUltiple SIgnal Classification (MUSIC) algorithm (Schmidt, 1986; Barrick and Lipa, 1997). Much of the operational use Codars with the SeaSonde Radial Suite. However, we take advantage of the latest development in data quality control by using Emery (2018) MATLAB toolbox. It contains the use of measured antenna pattern (Kohut and Glenn, 2003), an improved technique for the determination of the first order region (Kirincich, 2017) and the estimation of bearing errors (Emery and Washburn, 2019). Those error can be larger than 15° in some directions and need to be filtered (Clary et al., 2021).

With CODARs, MUSIC algorithm can give one or two solutions. In this study the MUSIC parameters are [10 ; 5 ; 1/3], corresponding to the MUSIC eigen value ratio, to the angle power ratio and to the MUSIC signal subspace diagonality, respectively. and if MUSIC angle difference between the dual solutions is greater than 20°. Additionally, other non-velocity metrics thresholds are set, as in Kirincich et al. (2012). MUSIC solutions are kept if the peak power is greater than 5 dB, if the monopole receive antenna signal-to-noise ratio (SNR) is greater than 5 and if the half power width (-3dB width) is lower than 30°. At last, measurements with bearing error higher than 5° are flagged.

3.2.2.2 WERAs

We are not aware of any direct estimation of bearing uncertainties for beam-forming Weras. We use a procedure that removes anomalous observations based on the spatial distribution of the received signal power, similarly to Cosoli et al. (2018). In each direction, data outside a 10% confidence interval are flagged. Measurements with signal to noise ratio lower than 8 dB are also removed.

3.2.3 Gap filling

Gaps are filled by time averaging, azimuthal averaging and then by an EOF procedure. Usually, time averaging is performed over 1h and azimuthal averaging is done on a 10° wedge. We use a 3h time averaging with a Gaussian function as a weighting having a 1h30 standard deviation. Azimuthal averaging is done on a 4° wedge, meaning that 2 degrees are taken into account in each direction. We prefer a small wedge in order to keep the averaging cell length smaller than the Rossby deformation Radius, even far away from the

HFR site. Moreover, the received signal power is also used as a weighting function during the averaging (Kirincich et al., 2012). After the averaging, an EOF procedure is computed through an iterative singular value decomposition (SVD) decomposition as it is the most accurate procedure to retrieve small scale features in noisy data (Beckers and Rixen, 2003; Alvera-Azcárate et al., 2005; Beckers et al., 2006; Taylor et al., 2013). EOF gap filling on HFR measurements before mapping total currents was indeed shown to improve the results from the 2Dvar algorithm (Yaremchuk and Sentchev, 2011).

3.2.4 Mapping

At last, total currents are mapped from time averaged radial currents on a 2 km resolution Cartesian grid. Several mapping procedures were previously tested with a focus on how they modify the estimation of rotational spectral fluxes (Clary et al., 2019). Variational interpolation (2Dvar, Yaremchuk and Sentchev, 2009) is the most accurate but requires a careful setting of the smoothing parameters (Appendix B of Clary et al. (2019)). The required typical scales of the curl and divergence fields are estimated from a first mapping with optimal interpolation (Kim et al., 2008). Total currents mapped with uncertainties larger than 0.05 m/s are then removed. 2Dvar mapping errors where normalized by the mean value and then multiplied by HFR mean accuracy.

3.3 Total currents analysis

3.3.1 Correspondence with SST and winds

Once the HFRs measurements are cleaned, averaged and combined into total currents, their analysis can begin. Here, the naming ’total’ has two meanings. The first meaning is that they are the result of a combination process. The second meaning is that they are the sum of differents dynamical components (section 3.4.1). Figure 24 shows some examples of daily-averaged total currents (black arrows) overlaid on daily-averaged sea surface temperature (obtained from *Aqua* MODIS and *Terra* MODIS) and one day averaged winds (obtained from ERA INTERIM, red arrows). In those examples, two types of circulations are observed. On the left panels (panels a and c, on 15/04/2013 and 01/09/2013), eddies are observed and North and South shore currents have opposite directions. Daily measured circulation is in good agreement with daily averaged sea surfce temperature.On the right panels (panel b and d, on 14/05/2013 and 29/10/2013), circulations are controlled by the winds. In particular, the coastal current shore is forced by the strong winds in panel d).

3.3.2 Seasonal circulation

Measurements and GSL model are now compared on the same period : from beginning 2015 to end 2017. The seasonal average is done over 3 years. Hereafter, a year is separated into three seasons : Winter (from January to April), Summer (from May to August) and Fall (from September to December). The seasonal wind rose (for 2015) is shown in figure 25. Dominant wind direction is East South East in winter, East North East in summer, and East in Fall. Wind direction is highly variable in Summer and in Fall, contrary to the Winter. The seasonally averaged circulation is shown in figure 26. The model shows a very similar circulation for all seasons, with an along channel circulation and strong anticyclonic vorticity along the south coast (figure 26 a), c), e)), whereas observations show some seasonal variations. For the observations, winter is characterized by eastward currents in a large part of the LSLE (in agreement with strong winds) and by a strong anticyclonic vorticity along the south coast (as in the model), summer is characterized by an anticylocnic circulation on the north part of the domain and fall by a moderate anticyclonic along the south coast. Even if observed currents can be suspicious (in particular near W1), seasonal circulation are very different between the model and the observations. The seasonal variation of wind (figure 25 have no clear effects on the modeled circulation. Yet, wind forcing on the observed circulation is not clear, as winds energy evolution and currents energy evolution are barely related (figure 27).

3.3.3 Rotary spectra

It is convenient to decompose the circulation into clockwise (CW) and counter clockwise (CCW) component as flows are influenced by tides and Earth's rotation (Gonella, 1972). In the Northern hemisphere, inertial motions are contained in the clockwise component. The relative importance between CW and CCW circulation are interpreted as follows : if CW is dominant, the circulation rotates in the clockwise (or anticyclonic) direction, and if CCW is dominant, the circulation rotates in the counter clockwise (or cyclonic) direction.

The temporal rotary spectra for Winter, Summer and Fall seasons are estimated for the model (figure 28) and for the observations (figure 29). Model and observations rotary spectra are similar for periods longer than 24h, where CW and CCW have the same spectral slope (k^{-1}). The k^{-1} slope is close to the slope estimated by Fu (1981) near the bottom (3900 m depth) on a mooring over the Mid-Atlantic Ridge near $27°N$. This k^{-1} slope would be steeper without bathymetry effects (see also figure 1 of Ferrari and Wunsch (2009)). Steep and rough bathymetry inhibit kinetic energy int the suberinertial range. The k^{-1} slope in the subinertial range, the semi-diurnal peak and the absence of a peak near the Coriolis frequency are the two main features shared by the model and the observations for all seasons. However, CW spectra estimated from the model are much stronger than the one estimated from observations at periods shorter than 24h. The latitude of the LSLE is 48.67°, thus Coriolis period (∼16 h) is between diurnal and semi-diurnal periods.

The forcing of near inertial motions by winds is essentially caused by the passage of storms (D'Asaro, 1985). Silverthorne and Toole (2009) found a strong seasonal cycle in the generation of near inertial motions from moorings in the western North Atlantic Ocean. However, there is no energy peak observed at near inertial frequencies for all seasons for the model and for the observations. At semi-diurnal frequencies (around M2 and S2), the strongest CW spectra are observed in Summer for both model and observations. Presumably, the internal semi-diurnal tides are enhanced in summer by strong near surface stratification.

3.3.4 Horizontal wavenumber-frequency spectra

At the scales of interest, several physical processes are present. The separation of those processes in the frequency-wavenumber space is not straigthforward. The seasonal frequency-wavenumber spectra of total currents (figure 30, for the models, left panels, and for the observations, right panels) are qualitatively similar to the schematic representation in Ferrari and Wunsch (2009), figure 2 of supplementary material. The features shared by the GSL model and by the observations are the existence of an energy band at semi diurnal frequencies for all seasons, the bulk of energy at the lowest frequencies and lower wavenumber (geostrophic currents), the absence of an inertial peak (also notable in rotary spectra figures) and the absence of inertia gravity waves (IGWs). The main difference between GSL model and observations is the very small energy spread around semi-diurnal frequencies in the observations. The energy spread should be caused by incoherent internal tides, which could be resolved by the radars even with the 3 h averaging.

3.4 Dynamical analysis

3.4.1 Helmotlz decomposition

It is convenient to consider the currents as the sum of tidal currents, a detided curl-free currents and detided divergence-free currents. Total surface currents ($\mathbf{u}$) are decomposed into the tidal currents ($\mathbf{u_{tide}}$) estimated by harmonic analysis (Pawlowicz et al., 2002), rotational currents ($\mathbf{u_{rot}}$) estimated from the detided currents by computing the non-divergent component (via Helmholtz decomposition), and detided divergent currents ($\mathbf{u_{div}}$).

$$\mathbf{u} = \mathbf{u_{rot}} + \mathbf{u_{div}} + \mathbf{u_{tide}} \tag{3.1}$$

The same analysis is done for currents from GSL model and from HFRs measurements. In the following sections, the balanced circulation is considered to be the detided rotational circulation and the unbalanced circulation is the sum of tidal currents and of detided divergent currents.

3.4.2 KE spectra

Seasonal KE spectra of the dynamicaal components are shown for the GSL model and for the observations (figure 31). The spectral space can be separated in three subspaces : scales larger than 25 km, scales between 10 km and 25 km , and scales smaller than 10 km. KE spectra slope flattening from the domain scale to 25 km is presumably due to size of the largest eddies limited by the estuary's width.. From scales between 10 km and 25 km spectral slope is k^{-3} for total currents and for rotational currents, as in other observations (Callies et al., 2014, e.g.). The steeper spectral slopes at the smaller scales is an effect of visocity and degrading resolution for the model and of 2dvar smoothing for the observations. As a consequence, the break around 12 km is not due to the injection scale.

In general, KE spectra between model and observations are remarkably similar for all seasons and seasonal variations are weak. The main difference between GSL model spectra and observed spectra is that observed divergent currents are around 10 times stronger than modeled divergent currents. The total KE spectra are dominated by rotational currents at the largest scales whereas they are dominated by divergent currents at scales smaller than 16 km for the observations and at scales smaller than 8 km for the GSL degraded currents. However, this scale is around 2-3 km for GSL 0.5 km resolution (Clary et al., 2021). This difference is due to the overstimation of divergent KE in the observations or to the underestimation of divergent KE in the model.

3.4.3 KE spectral fluxes

Seasonal KE spectral fluxes are shown in figure 32 (GSL model) and figure 33 (observations). If KE spectra are qualitatively similar between the model and the measurements, the KE spectral fluxes are highly different (figures 32, 33). The tidal and detided KE spectral fluxes and their interactions are shown for all seasons on the left panels. The balanced and unbalanced KE spectral fluxes and their interactions are shown for all seasons on the right panels.

For the GSL model, the mediand of total KE spectral fluxes are positive for all seasons and at all wavelengths, implying a direct cascade of KE at all scales, but the spread also have negative values. The positive spectral slope from the domain scale to a 12-18 km scale (season depending) implies a source of total KE at those scales, whereas negative spectral slope at scales smaller than 12-18 km implies a sink of total KE at the smallest scales. Tidal KE spectral fluxes are negligible for all seasons, but their interactions with detited currents are important. Those interactions are characterized by a direct cascade of KE and by a sink of KE (negative spectral slope) for all seasons, except in Winter at scales larger than 20 km where the spectral slope is positive (32). Yet, the large spread with both positive and negative values make interpretations difficult.The balanced-unbalanced decomposition (right panels) shows that balanced spectral fluxes are qualitatively similar for all seasons, with a negative to positive transition scale around 12 km. Unbalanced spectral fluxes are always positive (except at the domain scale in Summer), implying a direct KE cascade, as in Klein et al. (2008). As for tide-detided interactions, balanced-unbalanced interactions are always important at all scales and always imply a direct cascade of KE.

For the observations, total KE spectral fluxes are always negative at scales larger than 20 km, meaning that observations and model are in contradiction. Those contradictions are mainly a consequence of the divergent currents, which are difficult to observe with HFRs measurements. In Winter and in Summer, observed tide-detided interactions and balanced-unbalanced interactions are characterized by an inverse KE cascade for scales larger than 10 km, in contradiction with the model. However, in Fall, tide-detided interactions have a direct cascade and balanced-unbalanced interactions also have a direct cascade for scales smaller than 30 km, similar to the model results. Other differences between model and observations are 1) the weaker tide-detided interactions with the observations (likely a consequence of the 3 h temporal averaging used on HFRs raw measurements before mapping) and 2) the observed balanced transition scales are larger (~35 km in Winter and ~ 20 km in Fall) while no transitionn scale is observed in Summer.

3.5 Discussion and conclusion

The main features shared by the model and by the observations are the strong semi-diurnal KE peaks, the existence of semi-diurnal tide, the absence of IGWs in the superinertial range (except for possible semi-diurnal internal tides) and the absence of a near-inertial peak (figures 28 and 29). For now the absence of IGWs in the area is unexplained.

Model and observed seasonal currents are different (figure 26), and it is unclear if they represent the same variable. Observed currents can locally be suspicious near W1 or at the edge of the domain. However, the lack of seasonality in the model is also suspicious. The probability of a year long similar circulation in the LSLE is very low as the region has a 50°C difference in temperature extrema between winter and summer and as winds amplitudes and directions show strong seasonal variations. The CW dominance for all periods shorter than 24h in the rotary spectra estimated from the model is also very peculiar and it is not observed in the HFR measurements. Even if model and observed seasonal currents are different, their respective KE wavenumber spectra are qualitatively similar (figure 31). Highly different spectral KE fluxes between seasons and between model and observations highlight that KE spectral fluxes can not be inferred from the KE spectra (at least in the area of study).

At present, we are not able to identify frontogenesis signature with the observations because of divergent current sensitivity to errors of measurements. Future research efforts should focus on the obervations of the divergent currents, multiple improvements are possible. The main problem is the gaps in HFR measurements. HFRs in direction finding with only few antennas elements such CODARs can not resolve complex circulation patterns(de Paolo and Terrill, 2007). The new LERAs (Flament et al., 2016) looks more promising. HFRs placement is also to be carefully selected (when possible) in order to optimize the observed area coverage. Another possibility is the increasing of temporal averaging to further reduce measurement noise and missing data, as long as the dominant unbalanced motions are not filtered out.

This study also highlight two important dynamical considerations : the surface Stokes drift and the absence of IGWS. The surface Stokes drift is not considered in our current decomposition. It can however be an important reason for the difference between the model and the observations since HFRs have been shown to measure part of the surface Stokes drift in the region (Dussol et al., 2020). In order to compare model and observations, either the Stokes drift must be resolved or it must be quantified and removed from HFR measurements. Both cases require additional research. An open question is why high frequencies IGWs are not observed in the LSLE while they exist in abrupt bathymetry regions such as Drake passage (Rocha et al., 2016) or Kuroshio extension (Torres et al., 2018). High frequencies IGWs wavelength is probably smaller than HFR resolution (Richards et al., 2013).

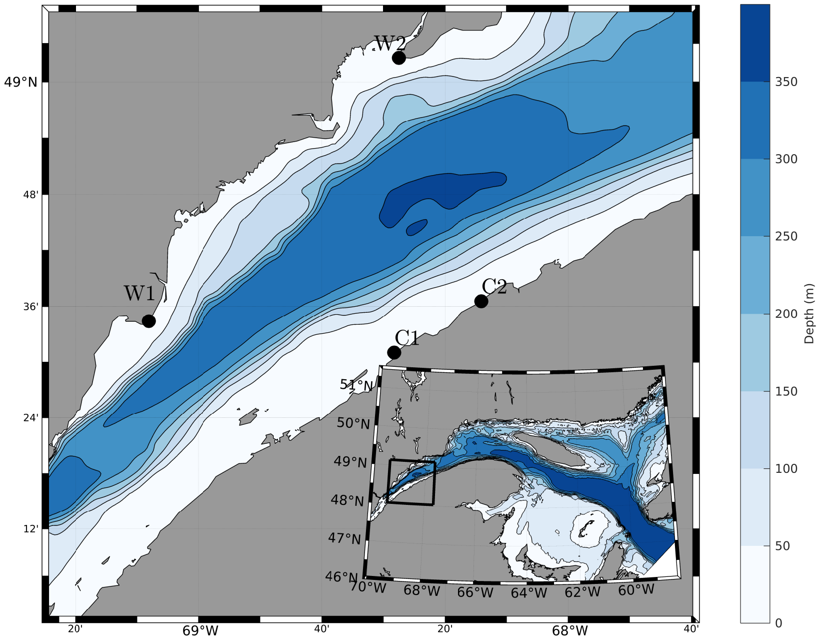

Figure 23: Bathymetry of the LSLE

3.6 Figures

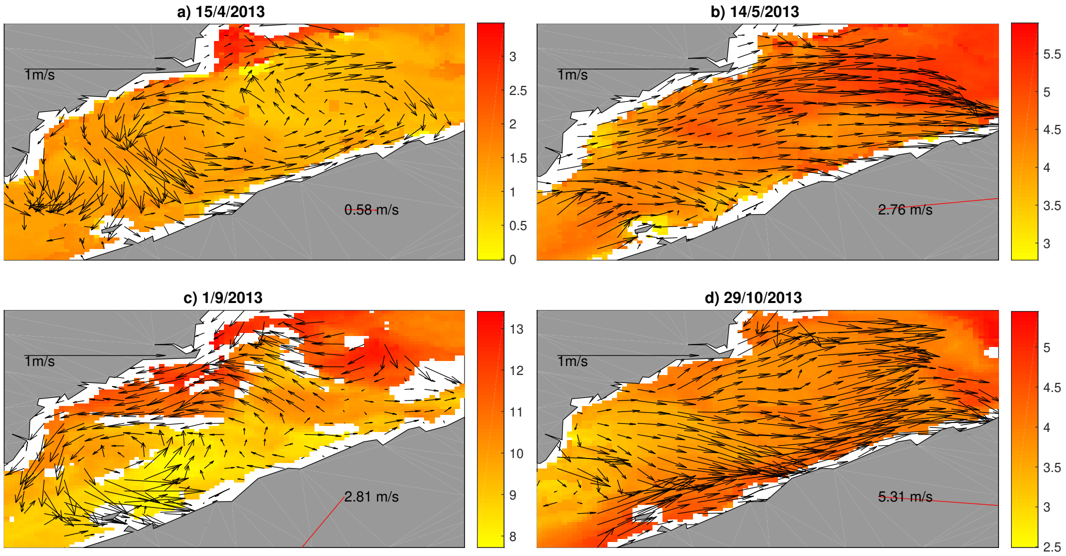

Figure 24: Example of daily average total currents (black arrow) overlaid on daily averaged sea surface temperature from *AQUA* and *TERRA* MODIS. Wind directions (red arrow) and amplitude are from ERA-INTERIM.

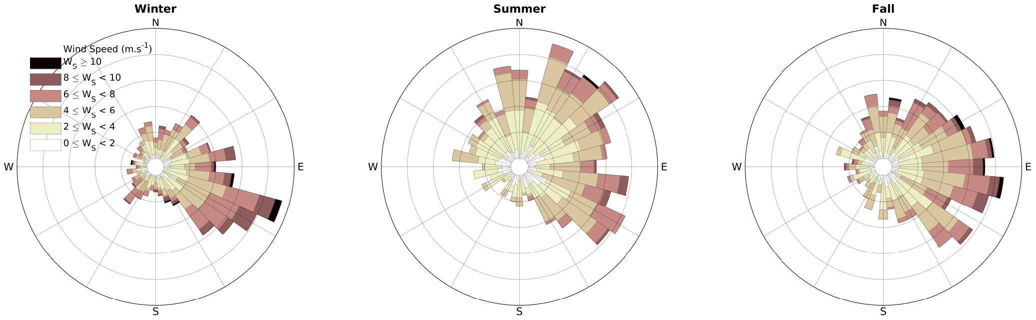

Figure 25: Seasonal wind rose from ERA-Interim on year 2015

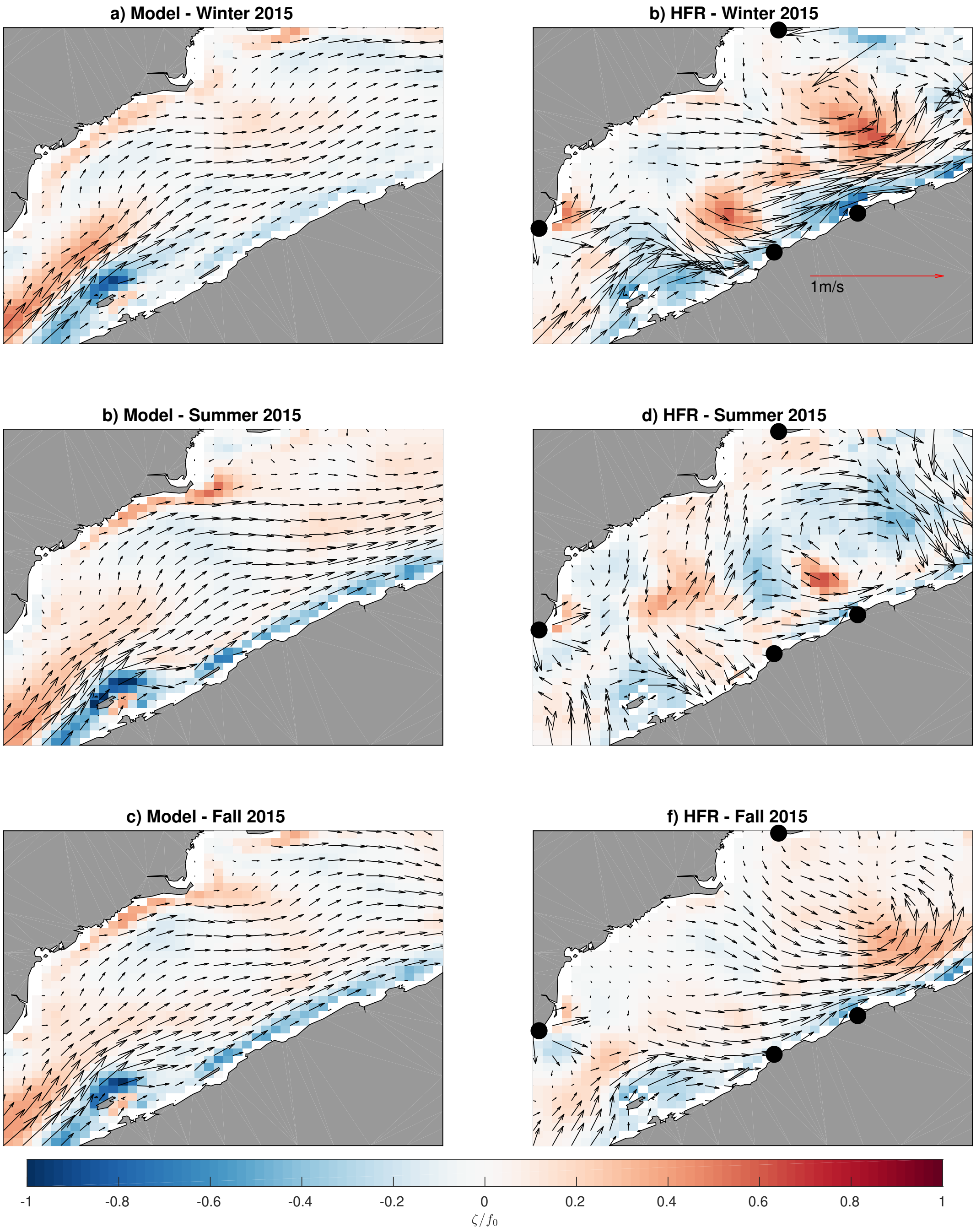

Figure 26: Seasonal mean circulation from GSL model (left panels) and from observations (right panels), in 2015

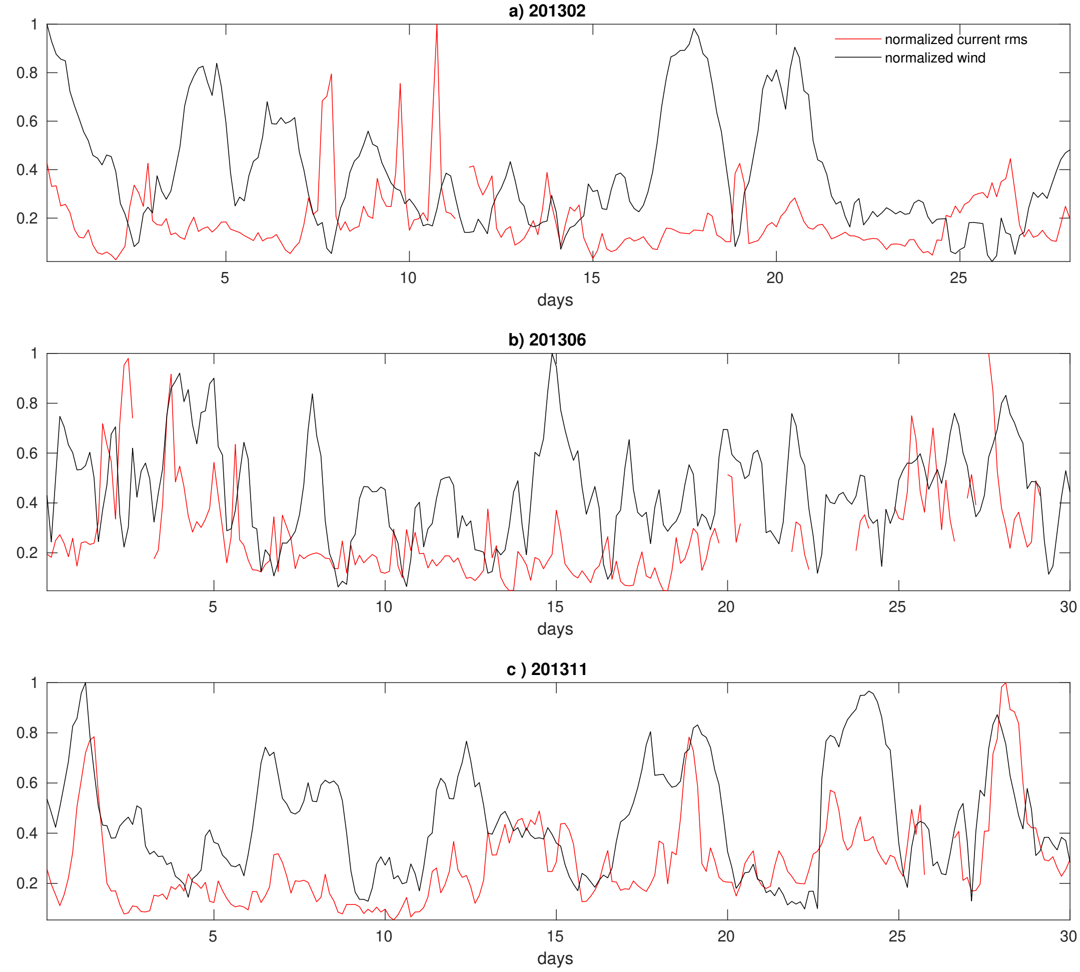

Figure 27: Max normalized wind and currents time series for February 2013 (panel a), June 2013 (panel b) and November 2013 (panel c).

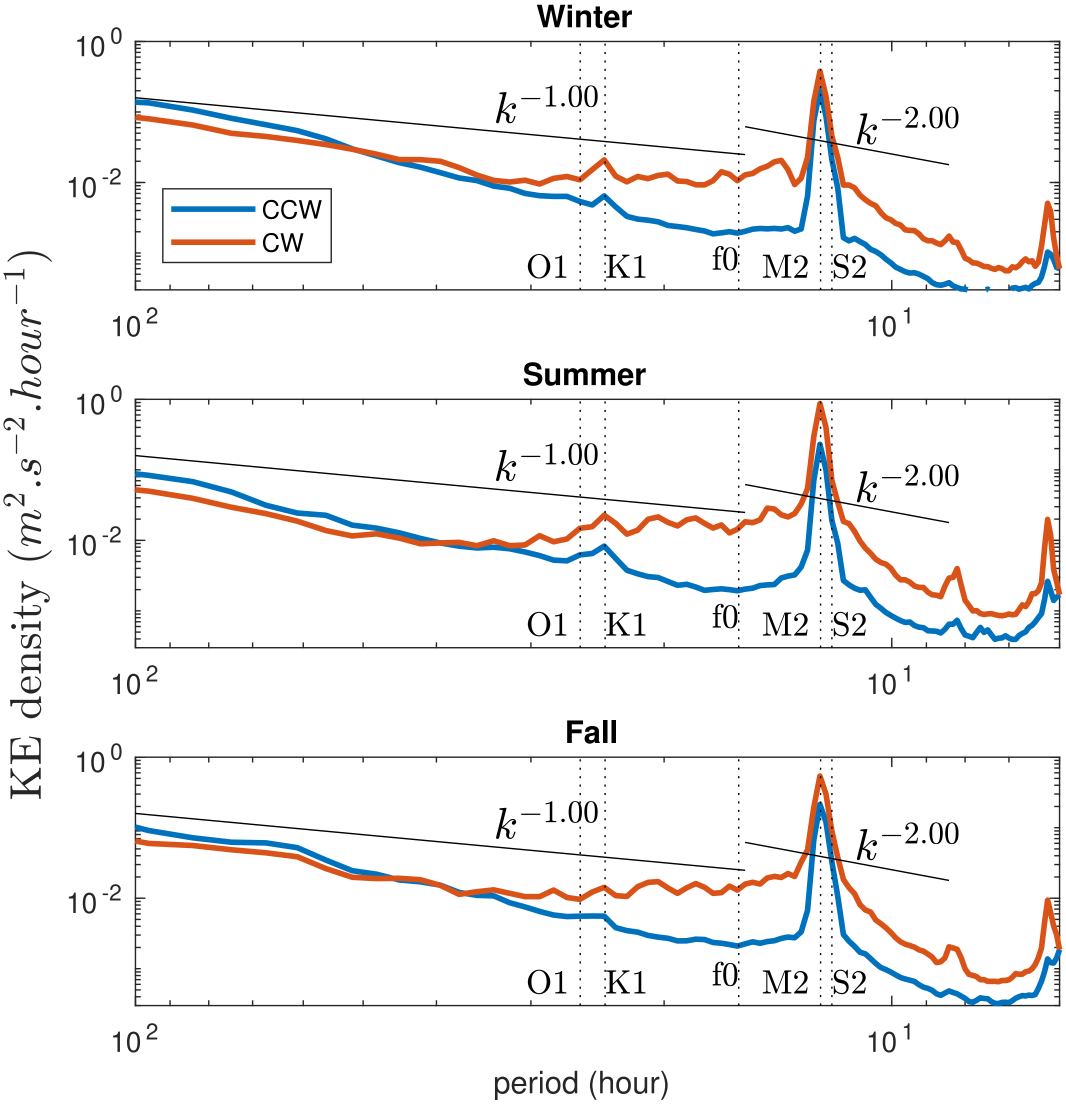

Figure 28: Rotary spectra for winter, summer and fall from the regional model output degraded at 2 km resolution (same resolution as the observed mapped currents)

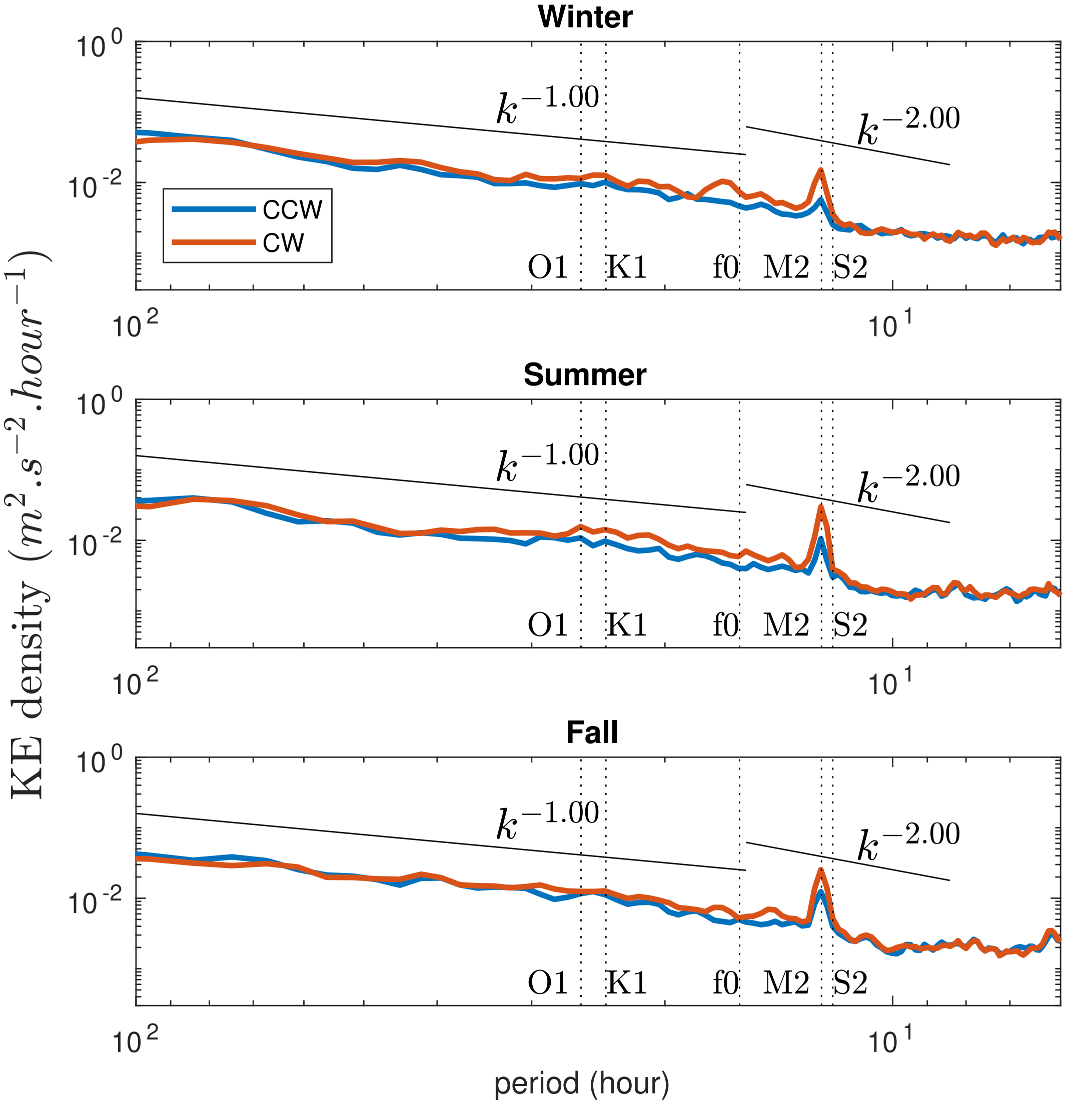

Figure 29: Rotary spectra for winter, summer and fall from the observations between 20015 and 2017

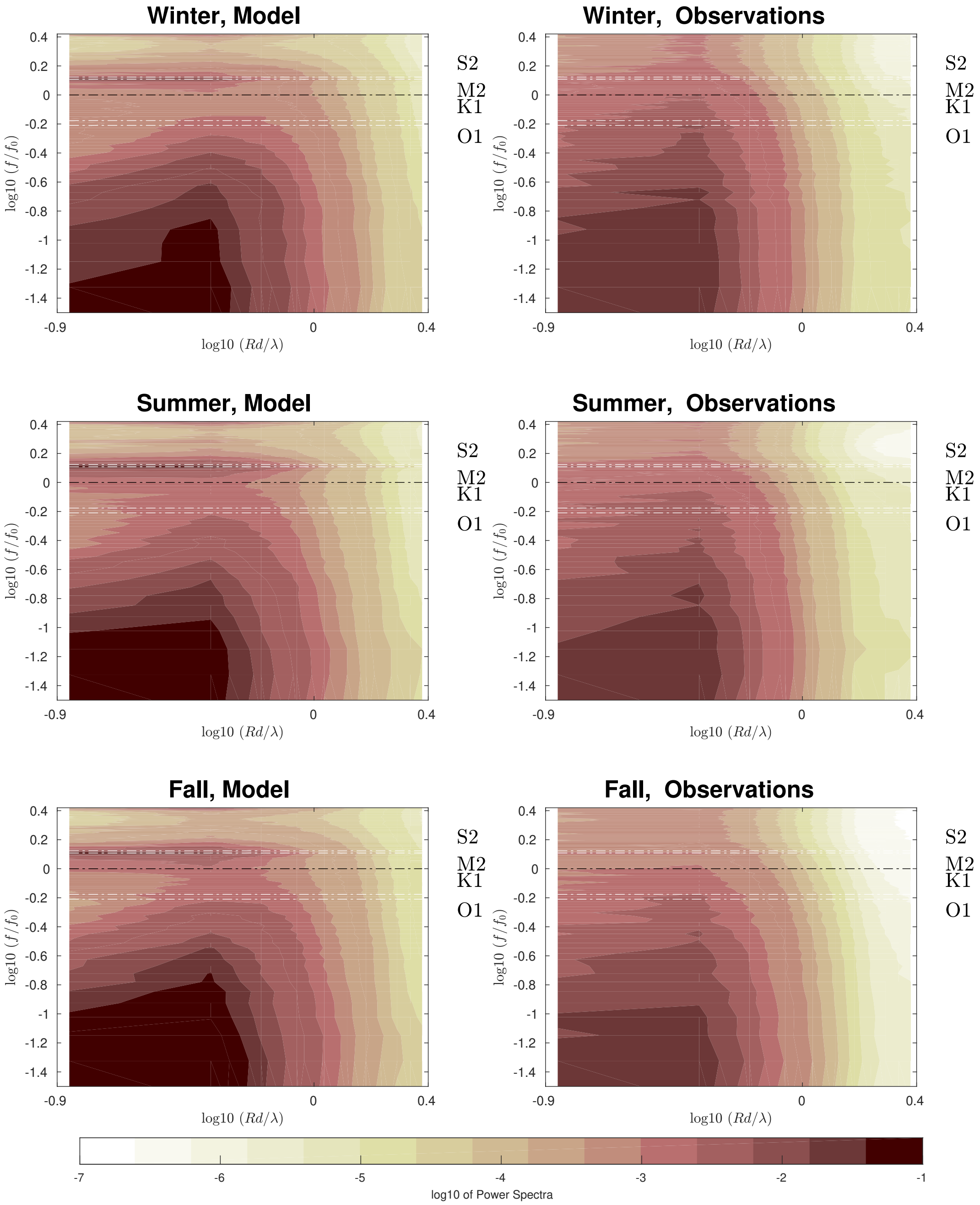

Figure 30: Seasonal wavenumber-frequency spectra from GSL model (left) and from HFR measurements (right)

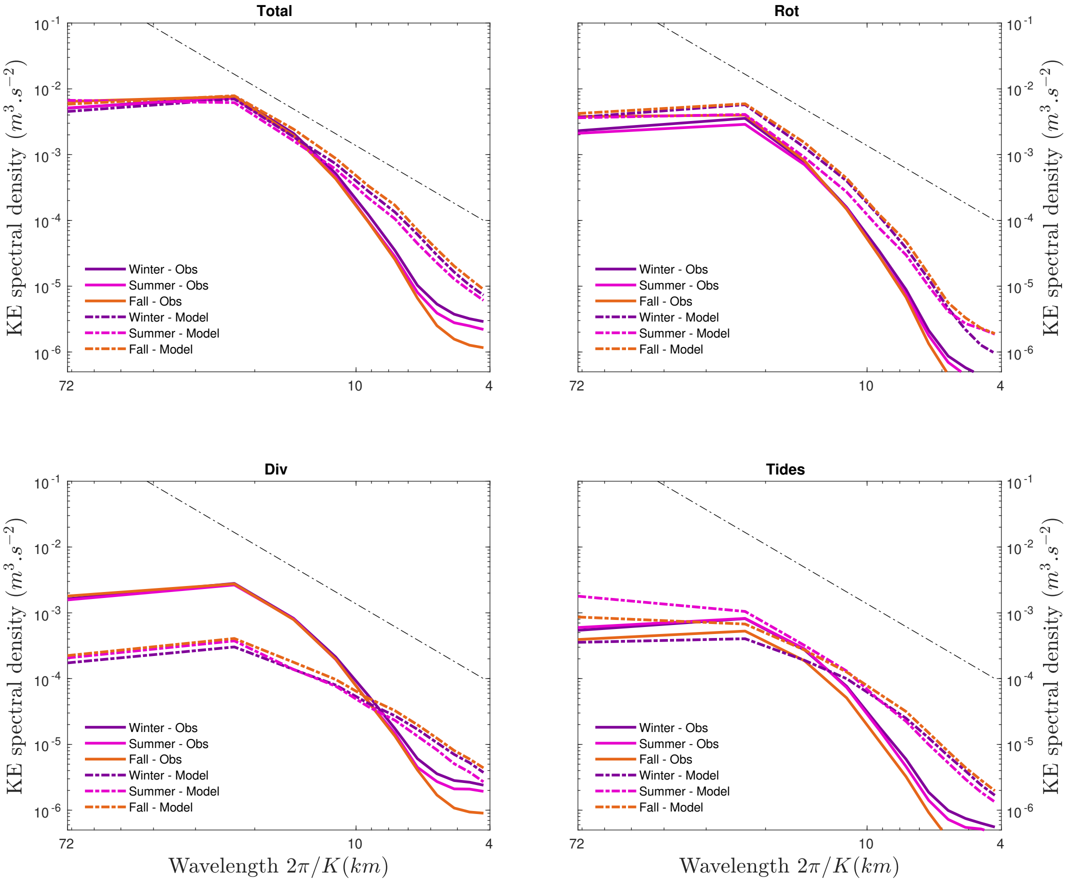

Figure 31: Seasonal KE spectra in the LSLE. Full line are from the observations and dot-dashed lines are from the GSl model at 2km resolution.

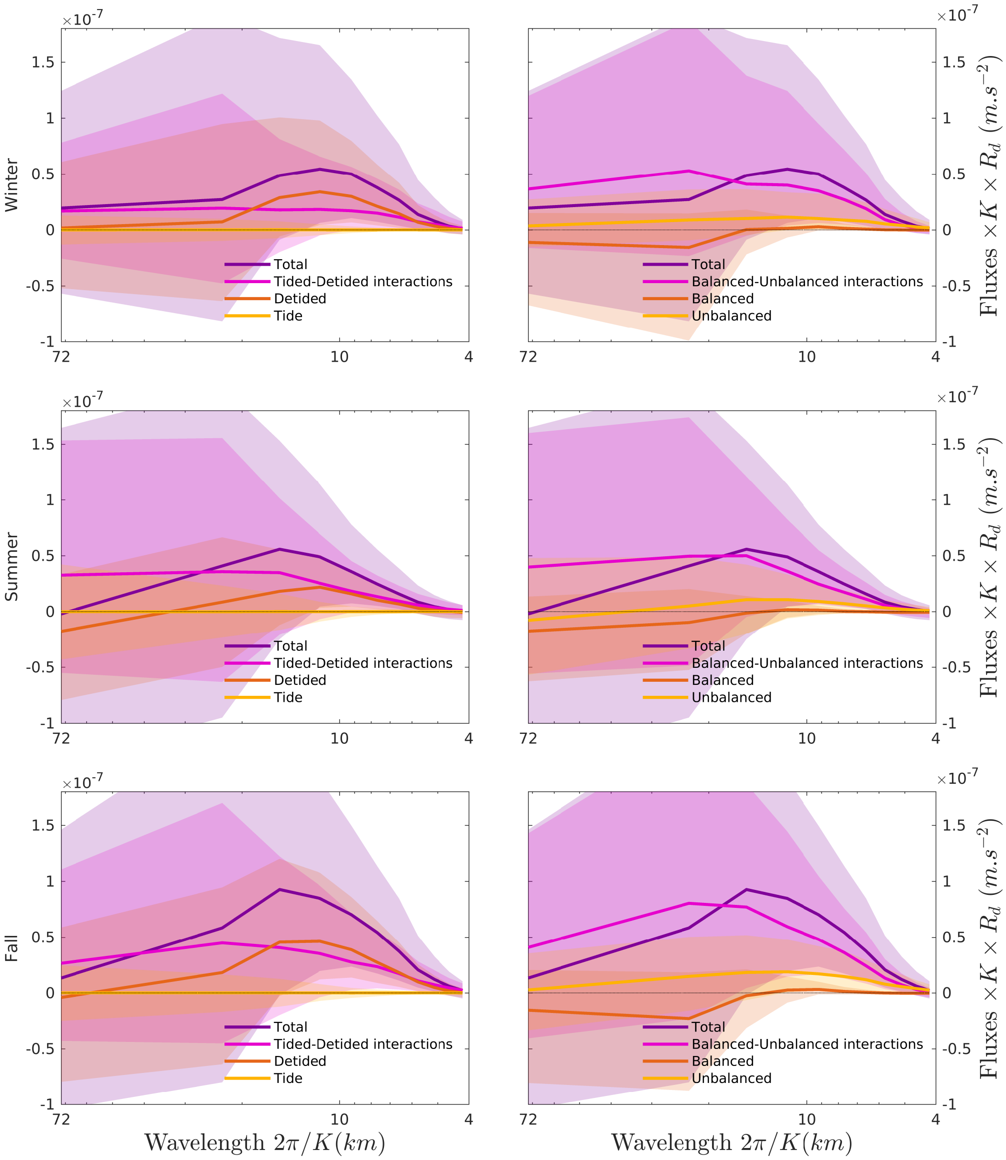

Figure 32: Seasonal KE spectral fluxes from GSL model

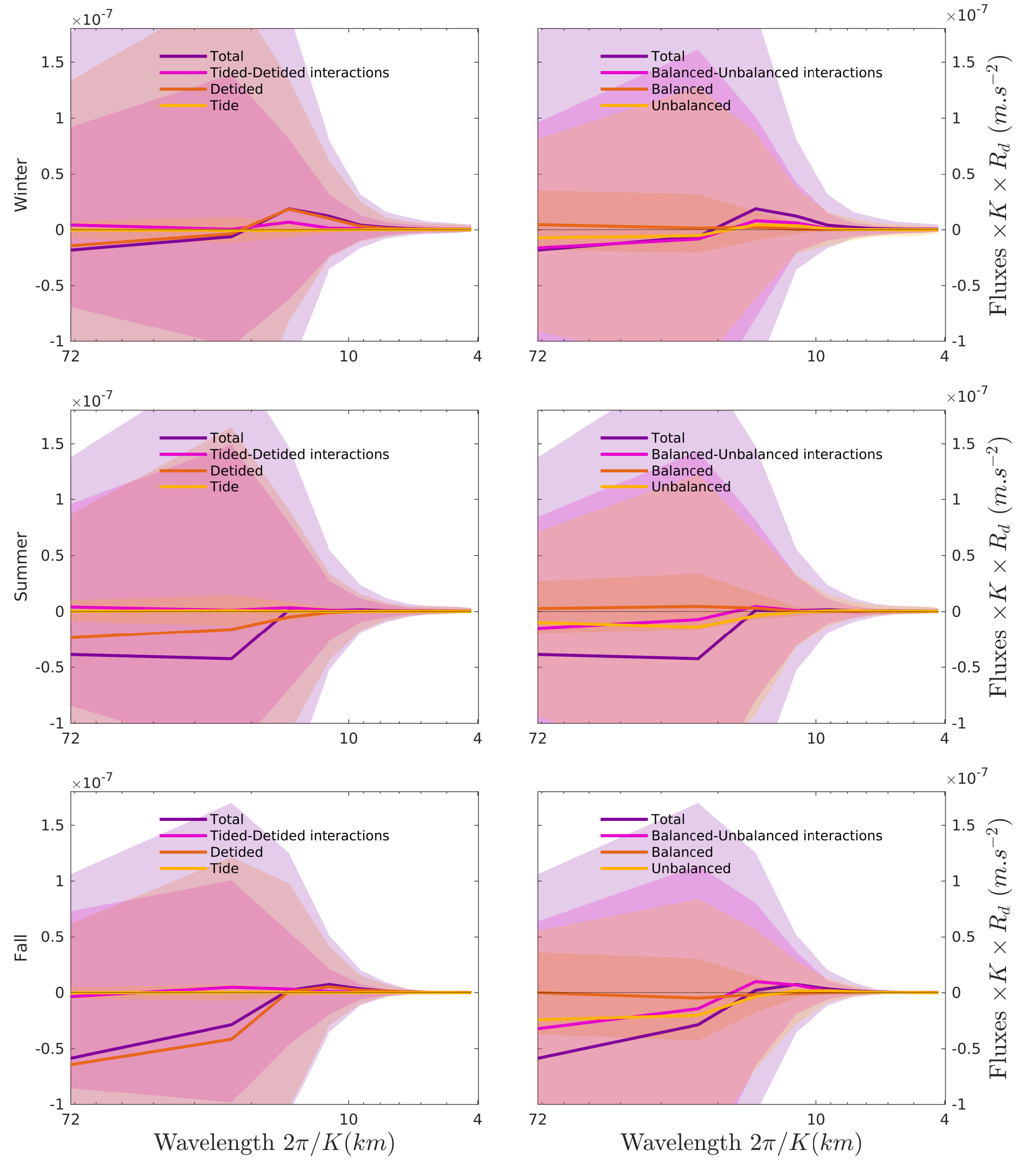

Figure 33: Seasonal KE spectral fluxes between 2015 and 2017 in the LSLE estimated from HFRs measurements

CONCLUSION GÉNÉRALE

L'océan est peuplé de structures dont les échelles caractéristiques varient entre moins de $O(1)$ m à plus de $O(1000)$ km (Ferrari, 2011). Bien que la répartition d'énergie cinétique entre les différentes échelles soit bien connue, les transferts d'énergie entre ces échelles spatiales sont plus difficiles à observer. Il est nécessaire de connaître les gradients horizontaux à toutes les échelles spatiales (équation 1). À notre connaissance, les Radars à Haute-Fréquence (RHFs) constituent les seuls systèmes d'observations capablent d'estimer directement ces transferts aux échelles spatiales inférieures à 50 km. L'objectif de cette thèse de doctorat est l'estimation du transfert (ou flux spectral) de l'énergie cinétique (KE) à partir des mesures de RHFs dans l'Estuaire Maritime du Saint-Laurent (EMSL).

Le premier article (publié, Clary et al., 2019) traite des limitations dues à l'utilisation des mesures de RHFs. Le flux spectral de référence provient d'un modèle Quasi-Géostrophique (QG) doublement périodique dont le flux spectral de KE est bien connu. Différentes sources d'erreurs sont appliquées sur les mesures de radars synthétiques. Les effets de ces erreurs sur les flux spectraux sont étudiés par comparaison avec le flux spectral de référence. Le deuxième article (bientôt soumis) se concentre sur la décomposition des courants et sur leurs interactions dans l'EMSL, en utilisant un modèle régional développé par Environnement et Changement Climatique Canada (ECCC). Le troisième article (en travaux) cherche à apporter des précisions sur la circulation dans la région en comparant le modèle régional et les observations des RHFs.

Le premier article montre que les effets géometriques (non périodicité, taille et ratio entre longueur et largeur du domaine) affectent essentiellement les grandes échelles. Les petites échelles sont affectées par la résolution spatiale. Toutefois, le bruit et l'absence des mesures peuvent affecter toutes les échelles spatiales. Le flux spectral du modèle QG est bien estimé lorsque le niveau de bruit dans les mesures des RHFs est inférieur à 30% et que les cartes de courant totauxcombinées avec moins de 70% de présence de courants radiaux sont éliminées. Lorsque ces conditions sont respectées et que les courants sont combinés avec une méthode de combinaison adaptée, l'échelle de transition (changement de signe du flux spectral) est bien estimée. Généralement, la méthode de combinaison la plus utilisée est la méthode des moindres carrées (Lipa and Barrick, 1983). Cette dernière est la plus facile à mettre en oeuvre, mais est la moins adaptée. La méthode variationnelle (2Dvar, Yaremchuk and Sentchev, 2009) est la plus difficile à mettre en oeuvre. Or, elle est plus performante que les autres pour l'estimation des gradients horizontaux des courants.

Dans le deuxième article, nous montrons que les flux spectraux de KE ont une distribution étalée et asymétrique. Cette distribution devient encore plus étalée pour les flux des mesures de RHFs, en raison des erreurs de mesures. La détermination des angles d'arrivée des signaux (nécessaire à la localisation des courants) a tendance à fausser les courants combinés lorsque la quantité de mesure est faible. Le moyennage temporel est un moyen d'atténuer les erreurs de mesures, au détriment de la perte de l'information existante aux périodes inférieures à la période de moyennage. Bien que très utilisé par les utilisateurs radars, pour remplir les trous dans les grilles de mesures des RHFs, le moyennage en angle ne diminue pas nécessairement la largeur de la distribution des flux. Il est aussi possible que ce moyennage en angle propage les erreurs. En considérant que les champs suspects sont éliminés, nos résultats montrent qu'une période minimale de trois mois est nécessaire pour obtenir un flux median représentatif. L'estimation des flux spectraux de KE de chaque mode (rotationnel, divergent et marées), ainsi que les interactions entre les différents modes de courants, montre que les interactions sont importantes dans la région d'étude. Par exemple, le courant de marée est très faible en KE et son flux spectral de KE est négligeable, mais il interagit fortement avec les courants résiduels. Le courant divergent est plus sensible aux erreurs de mesures que le courant rotationnel et les courants de marées. Ainsi, les erreurs de mesurent biaisent surtout les flux spectraux du courant divergent et les interactions de ce dernier avec les autres types de courant. Puisque dans l'EMSL les interactions entre le courant rotationnel et le courant divergent dominent le flux spectral de KE du courant total, il est nécessaire d'estimer au mieux les courants divergents. Malheureusement, les RHFs n'estiment pas correctement les courants divergents aux hautes fréquences.

Le troisième chapitre est une comparaison entre le modèle régional et les observations des RHFs dans l'EMSL. Cette comparaison entre la circulation simulée et observée repose sur l'analyse de la répartition de l'énergie cinétique en temps ou en espace pour différentes saisons. Les points communs entre le modèle régional et les observations sont : l'absence de pic à la fréquence de Coriolis, l'absence d'ondes d'inertie-gravité et la présences d'onde de marées semi-diurnes. Les courants, les spectres de KE et les flux saisonniers de KE du modèle varient peu alors que ceux des observations varient beaucoup. Pour les flux spectraux de KE, la plus grande différence s'observe en hiver, où le flux spectral du courant divergent observé est négatif à presque toutes les échelles spatiales. Nous ne pouvons pas expliquer avec certitude l'origine des différences saisonnières entre le modèle et les observations. Ces dernières peuvent provenir d'erreurs de mesure non considérées ou bien de la dynamique de certains processus manquante ou mal représentée par le modèle.

3.7 Retombées de la thèse

3.7.1 Développement d'une procédure de traitement de qualité des mesures de RHFs

Actuellement, il n'existe pas de norme dans la procédure de contrôle qualité des mesures de RHFs. Un effort de normalisation est toutefois mené par la National Oceanic and Atmospheric Administration (NOAA), sous forme d'un manuel nommé Quality Assurance / Quality Control of Real Time Oceanographic Data (QARTOD). La procédure mise en place, au cours de cette thèse, est indépendante du QARTOD, car ce dernier m'étais inconnu jusqu'au début 2021.Ainsi, les contrôles sont parfois différents de ceux du QARTOD et certains tests réalisés sont absents (ou seulement suggérés) dans le QARTOD. Par exemple, nous éliminons les mesures avec des erreurs d'angles supérieures à 5° pour les CODARs (Emery and Washburn, 2019) et nous faisons une régression linéaire avec la distance sur la puissance du signal reçu pour les WERAs (Cosoli et al., 2018). Un autre exemple, le moyennage temporel est fait en prenant en compte la puissance du signal reçu (Kirincich et al., 2012), puis les courants radiaux sont complétés par une méthode utilisant les Empirical orthogonal functions (EOF) itératives (Beckers and Rixen, 2003; Alvera-Azcárate et al., 2005; Beckers et al., 2006; Taylor et al., 2013). Chaque étape d'analyse entre la mesure brute du signal et l'analyse spectrale a été inspirée de la littérature. La procédure d'analyse est détaillée dans l'annexe 3). La mise en place de chacune des étapes a occupé une grande partie de la thèse de doctorat. En effet, il a fallu traiter les deux types de radars existants dans l'EMSL : les CODARs (fonctionnant en *direction-finding*) et les WERAs (fonctionnant en *beam-forming*). La dernière mise-à-jour de la procédure de traitement date d'octobre 2020.

3.7.2 Le 2dvar : une méthode de combinaison adaptée aux conditions de mesures

Les courants obtenus à partir des mesures RHFs dépendent de la méthode de combinaison choisie et de sa paramétrisation. La méthode 2dvar (méthode non locale) est la plus adaptée aux conditions de mesures. Avec la parametrisation proposée dans le premier article de cette thèse (Clary et al., 2019), la méthode 2dvar s'adapte en permanence aux conditions de mesures. Plus précisément, la résolution de la grille cartésienne sur laquelle la combinaison se fait, le niveau de bruit, le nombre de mesures, le nombre d'inconnues (les deux composantes du courant pour chaque point de la grille cartésienne), les échelles caractéristiques de l'écoulement sont pris en compte. Aussi, les paramètres de lissage du 2Dvar ont été rendus inversement proportionnels à la densité des données. Cela signifie que les contraintes de lissage augmentent localement avec le manque de mesures. Le but est d'atténuer les variations brusques du champ combiné lorsque des mesures manquent (ces variations brusques peuvent être dues au bruit de mesures). En comparaison, la méthode de combinaison aux moindres carrés ne dépend que de la moyenne des mesures dans un rayon donné. Ainsi, les travaux de cette thèse permettent de conclure qu'il est préférable d'utiliser la méthode de combinaison 2dvar pour toutes recherches en lien avec les courants totaux, comme par exemple l'étude de la dérive de surface.

3.7.3 Retombées pour d'autres projets

Les mesures de RHFs et les procédures de contrôle qualité servent à deux projets en cours sous la direction de Cédric Chavanne. Ils serviront également à d'autres projets dans le futur. Le premier projet en cours est le doctorat d'Abigaelle Dussol, intitulé " Balance and imbalance as seen in numerical and dynamically-inferred sea surface altimetry data in the St. Lawrence estuary". Le deuxième projet en cours concerne l'assimilation des mesures radars dans les modèles numériques d'ECCC (projet de post-doctorat de Sandy Gregorio). Cette assimilation peut néanmoins artificiellement créer dans ondes-d'inerties gravité.

3.8 Perspectives

3.8.1 Rappel sur le bilan de KE

Dans cette thèse de doctorat, on a cherché à estimer le transfert spectral de KE à la surface de l'"EMSL à partir de mesures de RHFs. Il est utile de remettre cette estimation dans son contexte. Le bilan de KE s'écrit (Capet et al., 2008c) :

$$\begin{aligned}
\frac{1}{2}\partial_t \mathbf{u}_h^2 &= -\mathbf{u}_h(\mathbf{u_h}.\nabla_\mathbf{h})\mathbf{u}_h - \mathbf{u}_h.w\partial_z\mathbf{u}_h - \frac{1}{\rho_0}\mathbf{u}_h\nabla_P + wb + \mathbf{u}_h.\mathbf{D}_h + \mathbf{u}_h\partial_z(\kappa\partial_z\mathbf{u}_h),\\
\partial_t KE &= \qquad A_h \qquad + \quad A_v \quad + \quad P \quad + \; C + \; R \; + \quad V.
\end{aligned}$$

Le terme de gauche est la dérivée temporelle du KE. Les termes de droite correspondent dans l'ordre : au flux de l'advection horizontale (A_h), au flux de l'advection verticale (A_v), au travail de la pression (P), à la conversion d'énergie potentielle en cinétique (C), au mélange horizontal (R), et au mélange vertical (comprenant le travail du vent, V). Les deux termes R et V comprennent aussi la dissipation. Parmi ces termes, seulement A_h et A_v sont capables de redistribuer le KE entre les échelles spatiales. Les autres membres de droite sont des sources ou des puits de KE. A travers cette thèse de doctorat, seul le terme A_h a été étudié, et seulement en surface. Pour connaître la variation de KE dans un domaine, il faudrait non seulement intégrer en temps, mais aussi en profondeur. Or. nous ne disposons que de mesures de courants en surface. La profondeur effective des radars utilisés est inférieure à un mètre. Pour estimer les divers termes du bilan de KE, une campagne océanographique complète, avec des sondes CTD ('Conductivity Temperature Depth') et des ADCP ('Acoustic Doppler Current Profiler') régulièrement espacés, est nécessaire.

3.8.2 Méthode pour le calcul du flux spectral dans le domaine spatial

Le calcul du flux spectral de KE s'est fait dans le domaine spectral en utilisant une décomposation en série de Fourier, comme effectué dans de nombreux articles dont Capet et al. (2008a,c); Klein et al. (2008); Molemaker et al. (2010); Arbic et al. (2012); Sasaki et al. (2014). Cependant, cette décomposition en série de Fourier suppose que le signal est périodique. Rendre artificiellement un signal périodique revient à multiplier le signal par une fenêtre dont les valeurs sont nulles aux bords. Le but est de minimiser le repliement spectral ('spectral leakage'). L'effet de cette fenêtre est de modifier une partie du signal. A titre personnel, j'utilise un cosine taper avec un ratio 0.5 (modifiant seulement 50% du signal) comme meilleur compromis entre la modification minimale du champ par la fenêtre et le problème de repliement spectral.

Une autre formulation du flux spectral de KE consiste à séparer le courant en un courant moyen et en une perturbation pour une échelle spatiale donnée (Scott and Wang, 2005; Scott and Arbic, 2007; Taylor and Straub, 2016). Même si dans la littérature cette séparation est effectuée dans le domaine spectral, il est possible de faire ce calcul dans le domaine spatial en suivant la formulation de Germano (1992). Cette approche permet aussi de cartographier les régions caractérisées par une cascade directe ou inverse (Xiao et al., 2009; Aluie et al., 2018) et ainsi de mieux identifier les processus en jeu. Dans ce cas, le flux d'énergie cinétique à une échelle L donnée vaut

$$\Pi(L) = \overline{\mathbf{U}(\mathbf{U}.\nabla)\mathbf{u}'} + \overline{\mathbf{U}(\mathbf{u}'.\nabla)\mathbf{U}} + \overline{\mathbf{U}(\mathbf{u}'.\nabla)\mathbf{u}'},$$

où $\overline{X}$ est l'opérateur moyenne, $\mathbf{U}$ est le courant moyen et $\mathbf{u}'$ le courant turbulent pour une échelle spatiale L donnée. Le premier terme traduit l'advection du courant turbulent par le courant moyen. Le deuxième terme traduit l'advection du courant moyen par le courant turbulent et le dernier terme traduit l'advection du courant turbulent par lui-même. Si le domaine est périodique, alors le dernier terme est nul. Cette méthode de calcul a aussi l'avantage, par rapport à l'analyse spectrale, de ne pas supposer la turbulence comme étant homogène. On suggère d'utiliser la formulation ci-dessus pour toutes estimations du flux spectral de KE dans des domaines de tailles similaire à celles observables par les RHFs ($\sim$ 100 km^2) afin de s'affranchir des effets du fenêtrage.

3.8.3 L'effet de la dérive de Stokes

Les RHFs mesurent une partie la dérive de Stokes en surface en plus des courants Eulériens moyens. La dérive de Stokes n'as pas été analysée dans cette thèse. Il existe un débat dans la littérature, à savoir si les RHFs mesurent la dérive de Stokes de surface ou une quantité liée à cette dernière (Chavanne, 2018). La première partie du doctorat (en cours) d'Abigaelle Dussol, sous la direction de Cédric Chavanne, à pour but de répond à ce dilemme. Il est possible que la dérive de Stokes soit l'une des causes principales de la différence entre les flux spectraux éstimés à partir du modèle régional GSL et ceux éstimés avec les observations. Très récemment, il a été montré que les RHFs mesurent la moitié de la dérive de Stokes de surface, lorsque cette dernière est non négligeable, soit en hiver (Dussol et al., 2020). Elle pourrait expliquer les différences entre le modèle et les observations en hiver. Aussi, une autre raison pour expliquer ces différences en hiver est la couverture de glace, qui limite la couverture des RHFs (Kamli et al., 2016).

3.9 Limites de la thèse

La principale limite de cette thèse de doctorat est le manque de confiance dans le flux spectral lié au courant divergent et à ses interactions avec les courants non divergent. Pour avoir confiance dans les flux spectraux de KE estimés à partir des mesures de RHFs, il faut : soit s'assurer que les courants divergents soient bien estimés par les radars ; soit choisir une région où les courants divergents sont négligeables et interagissent peu. Dans le premier cas, il faut choisir stratégiquement l'emplacement des RHFs, c'est à dire en testant plusieurs combinaisons d'emplacements avec des radars synthétiques. En pratique, ces emplacements dépendent davantage de la législation et de l'accès au réseau électrique que du bon vouloir de l'utilisateur. Le deuxième cas demande aussi une étude numérique en amont. À priori, les régions côtières où les courants divergents interagissent peu ne sont pas nombreuses.

Les travaux de cette thèse montrent la faiblesse d'utilisation des CODARs pour l'estimation des transferts d'énergie dans notre région d'étude, où la dynamique hors équilibre est importante. En effet, les CODARs ont du mal à estimer correctement les courants radiaux dans des scénarios simples (de Paolo and Terrill, 2007). Il semblerait que les WERAs soient plus efficaces pour estimer les transferts de KE. Il est à noter que la précision des WERAs est meilleure en direction finding qu'en beamforming (Kirincich et al., 2019). Comme les WERAs utilisés pour cette thèse fonctionnent en beamforming, il faudrait un retraitement complet de ces derniers. Enfin, un nouveau type de RHFs, les LERAs (Flament et al., 2016) pourrait constituer un système de mesure intéressant pour une estimation précise des courants divergents. Pour conclure, nous pensons que l'interprétation des flux spectraux, estimées à partir des RHFs, n'est vraiment réalisable qu'en connaissant l'importance de ces flux dans une région donnée. Ainsi, nous recommandons fortement de mener une étude numérique complète au préalable pour quantifier l'importance des différents terme du bilan de KE avant de se lancer dans l'estimation et l'interprétation des flux spectraux de KE. Enfin, il est possible que l'importante variabilité dans les flux spectraux estimés depuis le modèle régional et depuis les observations soit due à la présence des côtes de part et d'autre du domaine qui constribuent à transférer l’énergie des grandes vers les petites échelles.

ANNEXE III

PROCÉDURE D'ANALYSE

3.10 Contrôle Qualité des mesures HFRs

3.10.1 WERAs

Pour les WERAs, le contrôle qualité consiste à :

1. Éliminer les courants radiaux d'amplitude supérieure à 1.5 $m.s^{-1}$,
2. Éliminer les mesures à une distance supérieure à 50 km, si le WERA est PAB (i.e. W1),
3. Éliminer les mesures dont l'angle par rapport à la normale au réseau d'antennes de réception est supérieur à 40 degrés dans la direction antihoraire si le WERA est PAO (i.e. W2). À ces angles, le lobe principal du diagramme d'antenne est trop large et le lobe principal pointe vers l'océan le longe de la côte nord de l'estuaire.
4. Éliminer les mesures avec un ratio signal à bruit supérieur à 500 si la distance au radar est supérieure à 50 km,
5. Éliminer les mesures avec un ratio signal à bruit inférieur à 8 dB (Cosoli et al., 2018),
6. Éliminer les mesures en dehors d'un intervalle de confiance de manière itérative. A chaque itération, cet intervalle de confiance de 10% est calculé autour de la régression polynomiale (ordre 1 ou 3) du logarithme de la puissance de mesure reçue entre 8 km et 40 km de distance. Ce test est adapté de Cosoli et al. (2018), qui considère le logarithme du ratio signal à bruit. Les deux considérations ont été discutés par mail avec Simone

Cosoli.

3.10.2 CODARs

Pour les CODARs, le contrôle qualité consiste à :

1. Choisir le diagramme d'antenne en comparant les courants des CODARs avec les courants mesurés par des AWACs et des ADCPs mouillés dans l'EMSL (par Sandy Gregorio),
2. Déterminer les régions de premier ordre dans le spectre de Bragg à l'aide d'une technique d'imagerie (Kirincich, 2017),
3. Déterminer les pics de la fonction d'arrivée des angles possibles,
4. Déterminer les incertitudes et les biais de ces angles (Emery and Washburn, 2019),
5. Calculer la largeur de la fonction d'arrivée autour de ces angles (largeur à -3 dB)
6. Calculer la puissance du signal reçu à ces angles,
7. Choisir parmi les solutions possibles ce qui est du bruit. Parmi les trois solutions possibles avec les CODARs, soit une solution est gardée (Mono), soit deux solutions sont gardées (Dual). Les choix des trois paramètres déterminant si on garde une ou deux solutions dépendent de l'utilisateur.À chaque solution possible sont associés un vecteur propre et une valeur propre. Ces paramètres sont :
    (a) Le ratio des valeurs propres entre la solution Mono et la plus grande solution Dual. Si la valeur propre Mono est trop grande par rapport aux Dual, alors il ne peut y avoir qu'une seule solution
    (b) le degré de diagonalité de la matrice formée par les vecteurs propres des deux solutions Dual. La matrice devrait être parfaitement diagonale si ces vecteurs propres étaient orthogonaux.

   (c) le ratio entre le signal reçu par la première solution Dual avec la deuxième solution Dual. Si une solution est trop forte par rapport à l'autre, alors la solution ne peut pas être Dual.

8. Éliminer les solutions avec un pic de la fonction d'arrivée trop faible (inférieur à 5 dB), une largeur à -3 dB trop grande (supérieure à 50°) ou un ratio signal à bruit du monopole inférieur à 5 dB (Kirincich et al., 2012),
9. Éliminer les solutions avec une erreur d'angle supérieure à 5°. L'erreur d'angle est définie comme étant la norme des incertitudes et des biais, $DOA_{err} = \sqrt{DOA_{bias} + DOA_{std}}$

3.11 Moyennage des courants radiaux

Les mesures aux 10-20 mn sont ensuite moyennées en temps et en angle. Le moyennage consiste à :

1. Supprimer les mesures dans la terre ferme. Cette étape peut être faite durant le contrôle qualité.
2. Mettre toutes les mesures aux 10-20 mn sur la même grille polaire par interpolation linéaire selon la distance au radar. Cette étape est nécessaire pour les WERAs car leur bande passante change avec le temps. Les RHFs émettent en continu et sont donc obligés de moduler temporellement leurs fréquences pour distinguer le signal retour entre deux temps,
3. Utiliser une fonction de poids gaussienne en temps, d'écart type σ_t, sur un intervalle de temps de $2\sigma_t$. Pour les mesures HFRs, nous choisissons σ_t =1h30 afin d'avoir suffisamment de mesures et de conserver au mieux les marées semi-diurnes,
4. Utiliser la puissance reçue comme fonction de poids (Kirincich et al., 2012),
5. Moyenner en angles sur X°. Pour nous, X=4°,

6. Éliminer les courants moyennés ayant une précision supérieure à 0.06 m.s^{-1}. Une trop grande précision est due soit à une grande variabilité dans les mesures utilisées pour obtenir le courant moyen, soit à un trop faible nombre de mesures. Pour rappel, la précision est définie comme étant le ratio entre l'écart standard et la racine carrée du nombre d'observations,
7. Éliminer les courants moyennés ayant un écart standard supérieur à 0.6 m.s^{-1}. Ce point ci est un peu retondant avec le précédant, mais a tout de même permis d'éliminer quelques mesures visuellement suspectes,
8. Remplir les trous par une procédure EOF itérative (Beckers and Rixen, 2003; Alvera-Azcárate et al., 2005; Beckers et al., 2006; Taylor et al., 2013).

3.12 Obtention et analyse du courant total

3.12.1 Combinaison des données HFRs

Les courants HFRs moyennés sont ensuite combinés pour calculer le courant total L'obtention et le traitement du courant total consiste à

1. Éliminer les courants radiaux d'amplitude supérieure à 1.5 m.s^{-1} avant la combinaison,
2. Choisir une méthode de combinaison. Nous avons testé 3 méthodes locales (UWLS, WLS, OI, Kim et al., 2008) et une méthode non locale (2Dvar, Yaremchuk and Sentchev, 2009)
3. Déterminer les longueurs de variabilité du mode divergent et du mode rotationnel à partir des courants combinés uen première fois avec l'OI.
4. Paramétriser dynamiquement 2Dvar selon le niveau de bruit, le nombre de mesures, le nombre de points sur lesquels faire la combinaison, la résolution de la grille de combinaison et les longueurs de variabilité définies à l'étape précédente.

5. Combiner les courants radiaux en courants totaux avec 2Dvar. Je choisis aussi de rendre les paramètres du 2Dvar localement inversement proportionnels à la quantité de mesures dans un rayon donné. Ce point à été discuté par mail avec Max Yaremchuck et Alexei Sentchev, et testé aussi bien avec des mesures synthétiques que des vraies mesures,
6. Calculer les incertitudes liées à la combinaison et éliminer les courants avec une incertitudes supérieure à 0.05 m.s^{-1}. Les erreurs liées au 2Dvar sont en général semblables au GDOP sur les bords du domaine.
7. Éliminer les courants totaux d'amplitude supérieure à 1.5 m.s^{-1},
8. Éliminer les temps ayant un ratio signal à bruit trop fort sur l'ensemble des radars ν =0.3 (Clary et al., 2019). Pour le 2dvar le niveau de bruit est calculé en prenant en compte l'incertitude est non pas l'écart standard, ce qui abaisse significativement le niveau de bruit,
9. Éliminer les temps ayant trop peu de mesures par rapport aux nombres d'inconnues (2 inconnues par point de grille), soit une présence de mesures P inférieure à P=0.7 (Clary et al., 2019),
10. Remplir les trous par une procédure EOF itérative.

3.12.2 Analyse du courant total

Une fois que les courants totaux sont estimés, ils sont tournés de 30° environ pour être dans l'axe du canal. Puis, un sous-domaine d'étude rectangulaire est choisi pour les diverses analyses.

3.12.2.1 Décomposition

Le courant total est le courant obtenu de la combinaison des courants radiaux des HFRs. Il est ensuite décomposé comme suit :

$$\mathbf{u} = \mathbf{u_{rot}} + \mathbf{u_{div}} + \mathbf{u_t}. \tag{3.2}$$

où :

- $\mathbf{u_t}$ est le courant de marée. C'est la somme des marées diurnes (O1 et K1 calculées par analyse harmonique Pawlowicz et al. (2002)) et des marées semi-diurnes (entre 11h et 13.5h). Les marées semi-diurnes peuvent être non cohérentes car elles ont des fréquences plus grandes que la fréquence de Coriolis,
- $\mathbf{u_{rot}}$ est le courant rotationnel, obtenu du courant sans marée $\mathbf{u_{nt}} = \mathbf{u} - \mathbf{u_t}$ en résolvant l'équation d'Helmholtz $(\nabla \wedge \mathbf{u_{nt}}).\mathbf{k} = \nabla^2\Psi$) où l'inconnue Ψ est la fonction de courant. Puis, le courant rotationnel vaut $\mathbf{u_{rot}} = (-\partial_y\Psi, \partial_x\Psi)$. Pour résoudre l'équation, nous avons imposé des conditions de Neumann sur les bord Ouest et Est du domaine ($\Psi_X(y) = -\int_0^y u(X, y')dy'$, avec X étant le bord Ouest ou le bord Est du domaine) et des conditions de Neumann sur les bord Sud et Nord ($\Psi_{Sud} = 0$ et $\Psi_{Nord} = (\Psi_{Ouest}(Nord) + \Psi_{Est}(Nord))/2$),
- $\mathbf{u_{div}} = \mathbf{u} - \mathbf{u_t} - \mathbf{u_{rot}}$

3.12.2.2 Analyse spectrale

Les étapes de l'analyse spectrale sont :

1. Enlever la tendance linéaire. Si le champ est bidimensionnel, on enlève le plan tendance. Un autre choix est d'enlever la moyenne.
2. Multiplier le champ par une fenêtre. On choisit d'appliquer une fenêtre de Tukey ('cosine tapered') avec une fraction en cosinus de 0.5. Ainsi seule la moitie du domaine est modifiée par le fenêtrage. En comparaison, l'habituelle fenêtre de Hanning modifie presque la totalité du champ.
3. calculer la densité spectrale en puissance (pour les spectre de KE) ou la fonction de transfert (pour les flux spectraux de KE)

4. Définir le domaine spectral. En une dimension, le domaine spectral est le vecteur allant de dk à k_N par pas de dk, où $dk = 2\pi/L$ est la résolution spectrale, L est la longueur du domaine et $k_N = 2\pi/(2d)$ est la fréquence (ou nombre d'onde) de Nyquist. d est la résolution d'observation. En deux dimensions, il se peut que le domaine ne soit pas carré, auquel cas il faut définir deux résolutions spectrales distinctes.
5. Moyenner (pour le KE) ou intégrer (pour les flux spectraux de KE) sur le domaine spectral.

RÉFÉRENCES

Aluie, H., M. Hecht, and G. K. Vallis, 2018: Mapping the Energy Cascade in the North Atlantic Ocean: The Coarse-Graining Approach. *J. Phys. Oceanogr.*, **48 (2)**, 225–244, doi:10.1175/JPO-D-17-0100.1.

Alvera-Azcárate, A., A. Barth, M. Rixen, and J. Beckers, 2005: Reconstruction of incomplete oceanographic data sets using empirical orthogonal functions: application to the Adriatic Sea surface temperature. *Ocean Model.*, **9 (4)**, 325–346, doi:10.1016/j.ocemod.2004.08.001.

Amores, A., G. Jordà, T. Arsouze, and J. Le Sommer, 2018: Up to What Extent Can We Characterize Ocean Eddies Using Present-Day Gridded Altimetric Products? *J. Geophys. Res. Ocean.*, **123 (10)**, 7220–7236, doi:10.1029/2018JC014140.

Arbic, B. K., and G. R. Flierl, 2003: Coherent vortices and kinetic energy ribbons in asymptotic quasi two-dimensional f-plane turbulence. *Phys. Fluids*, **15 (8)**, 2177–2189, doi:10.1063/1.1582183.

Arbic, B. K., M. Müller, J. G. Richman, J. F. Shriver, A. J. Morten, R. B. Scott, G. Sérazin, and T. Penduff, 2014: Geostrophic Turbulence in the Frequency–Wavenumber Domain: Eddy-Driven Low-Frequency Variability*. *J. Phys. Oceanogr.*, **44 (8)**, 2050–2069, doi:10.1175/JPO-D-13-054.1.

Arbic, B. K., K. L. Polzin, R. B. Scott, J. G. Richman, and J. F. Shriver, 2013: On Eddy Viscosity, Energy Cascades, and the Horizontal Resolution of Gridded Satellite Altimeter Products*. *J. Phys. Oceanogr.*, **43 (2)**, 283–300, doi:10.1175/JPO-D-11-0240.1.

Arbic, B. K., R. B. Scott, G. R. Flierl, A. J. Morten, J. G. Richman, and J. F. Shriver, 2012: Nonlinear Cascades of Surface Oceanic Geostrophic Kinetic Energy in the Frequency Domain. *J. Phys. Oceanogr.*, **42**, 1577–1600, doi:10.1175/JPO-D-11-0151.1.

Ardhuin, F., L. Marié, N. Rascle, P. Forget, and A. Roland, 2008: Observation and estimation of Lagrangian, Stokes and Eulerian currents induced by wind and waves at the sea surface. *J. Phys. Oceanogr.*, **39 (11)**, 2820–2838, doi:10.1175/2009JPO4169.1.

Barrick, D., and B. Lipa, 1997: Evolution of Bearing Determination in HF Current Mapping Radars. *Oceanography*, **10 (2)**, 72–75, doi:10.5670/oceanog.1997.27.

Beckers, J. M., A. Barth, and A. Alvera-Azcárate, 2006: DINEOF reconstruction of clouded images including error maps application to the Sea-Surface Temperature around Corsican Island. *Ocean Sci.*, **2 (2)**, 183–199, doi:10.5194/os-2-183-2006.

Beckers, J. M., and M. Rixen, 2003: EOF Calculations and Data Filling from Incomplete Oceanographic Datasets*. *J. Atmos. Ocean. Technol.*, **20 (12)**, 1839–1856, doi:10.1175/1520-0426(2003)020⟨1839:ECADFF⟩2.0.CO;2.

Boccaletti, G., R. Ferrari, and B. Fox-Kemper, 2007: Mixed Layer Instabilities and Restratification. *J. Phys. Oceanogr.*, **37 (9)**, 2228–2250.

Callies, J., and R. Ferrari, 2013: Interpreting Energy and Tracer Spectra of Upper-Ocean Turbulence in the Submesoscale Range (1–200 km). *J. Phys. Oceanogr.*, **43 (11)**, 2456–2474, doi:10.1175/JPO-D-13-063.1.

Callies, J., R. Ferrari, and O. Bühler, 2014: Transition from geostrophic turbulence to inertia–gravity waves in the atmospheric energy spectrum. *Proc. Natl. Acad. Sci.*, **111 (48)**, 17 033–17 038, doi:10.1073/pnas.1410772111.

Callies, J., R. Ferrari, J. M. Klymak, and J. Gula, 2015: Seasonality in submesoscale turbulence. *Nat. Commun.*, **6**, 6862, doi:10.1038/ncomms7862.

Capet, X., P. Klein, B. L. Hua, G. Lapeyre, and J. C. McWilliams, 2008a: Surface kinetic energy transfer in surface quasi-geostrophic flows. *J. Fluid Mech.*, **604**, 165–174, doi:10.1017/S0022112008001110.

Capet, X., J. C. McWilliams, M. J. Molemaker, and A. F. Shchepetkin, 2008b: Mesoscale to Submesoscale Transition in the California Current System. Part II: Frontal Processes. *J. Phys. Oceanogr.*, **38 (1)**, 44–64, doi:10.1175/2007JPO3672.1.

Capet, X., J. C. McWilliams, M. J. Molemaker, and a. F. Shchepetkin, 2008c: Mesoscale to Submesoscale Transition in the California Current System. Part III: Energy Balance and Flux. *J. Phys. Oceanogr.*, **38 (1)**, 2256–2269.

Chapman, R. D., L. K. Shay, H. C. Graber, J. B. Edson, A. Karachintsev, C. L. Trump, and D. B. Ross, 1997: On the accuracy of HF radar surface current measurements: Intercomparisons with ship-based sensors. *J. Geophys. Res. Ocean.*, **102 (C8)**, 18 737–18 748, doi:10.1029/97JC00049.

Charney, J. G., 1971: Geostrophic Turbulence. *J. Atmos. Sci.*, **28 (6)**, 1087–1095, doi:10.1175/1520-0469(1971)028⟨1087:GT⟩2.0.CO;2.

Chavanne, C., 2018: Do High-Frequency Radars Measure the Wave-Induced Stokes Drift? *J. Atmos. Ocean. Technol.*, **35 (5)**, 1023–1031, doi:10.1175/JTECH-D-17-0099.1.

Chavanne, C., P. Flament, and K. W. Gurgel, 2010: Interactions between a Submesoscale Anticyclonic Vortex and a Front*. *J. Phys. Oceanogr.*, **40 (8)**, 1802–1818, doi:10.1175/2010JPO4055.1.

CHEN, Q., S. CHEN, G. L. EYINK, and D. D. HOLM, 2005: Resonant interactions in rotating homogeneous three-dimensional turbulence. *J. Fluid Mech.*, **542 (-1)**, 139, doi:10.1017/S0022112005006324, 0404055.

Clary, J., C. Chavanne, and L. P. Nadeau, 2021: How well can surface KE spectral fluxes be estimated from HFRs ? *Unpubl. Artic.*

Clary, J., L.-P. Nadeau, and C. Chavanne, 2019: The Effect of Measurement Limitations on High-Frequency Radar-Derived Spectral Energy Fluxes. *J. Atmos. Ocean. Technol.*, **36 (11)**, 2139–2152, doi:10.1175/JTECH-D-18-0237.1.

Cosoli, S., B. Grcic, S. de Vos, and Y. Hetzel, 2018: Improving Data Quality for the Australian High Frequency Ocean Radar Network through Real-Time and Delayed-Mode Quality-Control Procedures. *Remote Sens.*, **10 (9)**, 1476, doi:10.3390/rs10091476.

Cyr, F., D. Bourgault, and P. S. Galbraith, 2011: Interior versus boundary mixing of a cold intermediate layer. *J. Geophys. Res.*, **116 (C12)**, C12 029.

D'Asaro, E. A., 1985: The Energy Flux from the Wind to Near-Inertial Motions in the Surface Mixed Layer. 1043–1059 pp., doi:10.1175/1520-0485(1985)015⟨1043:TEFFTW⟩2.0.CO;2.

de Paolo, T., and E. Terrill, 2007: Skill Assessment of Resolving Ocean Surface Current Structure Using Compact-Antenna-Style HF Radar and the MUSIC Direction-Finding Algorithm. *J. Atmos. Ocean. Technol.*, **24 (7)**, 1277–1300, doi:10.1175/JTECH2040.1.

Dussol, A. R., C. Chavanne, S. Gregorio, and D. Dumont, 2020: Experimental confirmation of Stokes drift measurement by high frequency radars. *Manuscr. Submitt. Publ.*

Egbert, G. D., and S. Y. Erofeeva, 2002: Efficient inverse modeling of barotropic ocean tides. *J. Atmos. Ocean. Technol.*, **19 (2)**, 183–204, doi:10.1175/1520-0426(2002)019⟨0183:EIMOBO⟩2.0.CO;2.

Emery, B., 2018: {HFR CS Processing Toolbox for MATLAB}, Software Release Version 1.0, https://doi.org/10.5281/zenodo.1451950. doi:10.5281/zenodo.1451950.

Emery, B., and L. Washburn, 2019: Uncertainty Estimates for SeaSonde HF Radar Ocean Current Observations. *J. Atmos. Ocean. Technol.*, **36 (2)**, 231–247, doi:10.1175/JTECH-D-18-0104.1.

Emery, W. J., 2001: *Data Analysis Methods in Physical Oceanography*. Elsevier, doi:10.1016/B978-0-444-50756-3.X5000-X.

Ferrari, R., 2011: Ocean science. A frontal challenge for climate models. *Science*, **332 (6027)**, 316–7.

Ferrari, R., and C. Wunsch, 2009: Ocean Circulation Kinetic Energy: Reservoirs, Sources, and Sinks. *Annu. Rev. Fluid Mech.*, **41 (1)**, 253–282, doi:10.1146/annurev.fluid.40.111406.102139.

Flament, P., D. Harris, M. Flament, I. Fernandez, R. Hlivak, X. Flores-vidal, and L. Marié, 2016: A Compact High Frequency Doppler Radio Scatterometer for Coastal Oceanography. *AGU Fall Meet. Abstr.*, Vol. 2016, OS11C–06.

Flores-vidal, X., P. Flament, R. Durazo, C. Chavanne, and K. W. Gurgel, 2013: High-frequency radars: Beamforming calibrations using ships as reflectors. *J. Atmos. Ocean. Technol.*, **30** **(3)**, 638–648, doi:10.1175/JTECH-D-12-00105.1.

Forget, P., 2015: Noise properties of HF radar measurement of ocean surface currents. *Radio Sci.*, **50** **(8)**, 764–777, doi:10.1002/2015RS005681.

Fox-Kemper, B., R. Ferrari, and R. Hallberg, 2008: Parameterization of Mixed Layer Eddies. Part I: Theory and Diagnosis. *J. Phys. Oceanogr.*, **38** **(6)**, 1145–1165.

Fox-Kemper, B., and Coauthors, 2019: Challenges and Prospects in Ocean Circulation Models. *Front. Mar. Sci.*, **6** **(FEB)**, 1–29, doi:10.3389/fmars.2019.00065.

Fu, L.-L., 1981: Observations and models of inertial waves in the deep ocean. *Rev. Geophys.*, **19** **(1)**, 141, doi:10.1029/RG019i001p00141.

Fu, L. L., and C. Ubelmann, 2014: On the transition from profile altimeter to swath altimeter for observing global ocean surface topography. *J. Atmos. Ocean. Technol.*, **31** **(2)**, 560–568, doi:10.1175/JTECH-D-13-00109.1.

Galbraith, P. S., 2006: Winter water masses in the Gulf of St. Lawrence. *J. Geophys. Res.*, **111** **(C6)**, C06 022.

Germano, M., 1992: Turbulence: the filtering approach. *J. Fluid Mech.*, **238**, 325–336.

Gómez-Navarro, L., R. Fablet, E. Mason, A. Pascual, B. Mourre, E. Cosme, and J. L. Sommer, 2018: SWOT spatial scales in the western Mediterranean sea derived from pseudo-observations and an Ad Hoc filtering. *Remote Sens.*, **10** **(4)**, 1–30, doi:10.3390/rs10040599.

Gonella, J., 1972: A rotary-component method for analysing meteorological and oceanographic vector time series. *Deep. Res. Oceanogr. Abstr.*, **19** **(12)**, 833–846, doi:10.1016/0011-7471(72)90002-2.

Gurgel, K. W., H. H. Essen, and S. P. Kingsley, 1999: High-frequency radars: physical limitations and recent developments. *Coast. Eng.*, **37** **(3-4)**, 201–218, doi:10.1016/S0378-3839(99)00026-5.

Harris, F., 1978: On the use of windows for harmonic analysis with the discrete Fourier transform. *Proc. IEEE*, **66** **(1)**, 51–83, doi:10.1109/PROC.1978.10837.

Held, I. M., R. T. Pierrehumbert, S. T. Garner, and K. L. Swanson, 1995: Surface quasi-geostrophic dynamics. *J. Fluid Mech.*, **282**, 1–20.

Hoskins, B. J., and F. P. Bretherton, 1972: Atmospheric Frontogenesis Models: Mathematical Formulation and Solution. *J. Atmos. Sci.*, **29**, 11–37.

Ingram, R. G., and M. I. El-Sabh, 1992: Fronts and Mesoscale Features in the St Lawrence Estuary. *Oceanogr. a Large-Scale Estuar. Syst.*, Vol. 39, 71–93, doi:10.1002/9781118663783.ch4.

Kamli, E., C. Chavanne, and D. Dumont, 2016: Experimental Assessment of the Performance of High-Frequency CODAR and WERA Radars to Measure Ocean Currents in Partially Ice-Covered Waters. *J. Atmos. Ocean. Technol.*, **33 (3)**, 539–550, doi:10.1175/JTECH-D-15-0143.1.

Khatri, H., J. Sukhatme, A. Kumar, and M. K. Verma, 2018: Surface ocean enstrophy, kinetic energy fluxes, and spectra from satellite altimetry. *J. Geophys. Res. Ocean.*, **123 (5)**, 3875–3892, doi:10.1029/2017JC013516.

Kim, S. Y., 2010: Observations of submesoscale eddies using high-frequency radar-derived kinematic and dynamic quantities. *Cont. Shelf Res.*, **30 (15)**, 1639–1655.

Kim, S. Y., and P. M. Kosro, 2013: Observations of near-inertial surface currents off Oregon: Decorrelation time and length scales. *J. Geophys. Res. Ocean.*, **118 (7)**, 3723–3736, doi:10.1002/jgrc.20235.

Kim, S. Y., E. J. Terrill, and B. D. Cornuelle, 2008: Mapping surface currents from HF radar radial velocity measurements using optimal interpolation. *J. Geophys. Res.*, **113 (C10)**, C10 023, doi:10.1029/2007JC004244.

Kirincich, A., 2017: Improved detection of the first-order region for direction-finding HF radars using image processing techniques. *J. Atmos. Ocean. Technol.*, **34 (8)**, 1679–1691, doi:10.1175/JTECH-D-16-0162.1.

Kirincich, A., B. Emery, L. Washburn, and P. Flament, 2019: Improving surface current resolution using direction finding algorithms for multiantenna high-frequency radars. *J. Atmos. Ocean. Technol.*, **36 (10)**, 1997–2014, doi:10.1175/JTECH-D-19-0029.1.

Kirincich, A. R., T. De Paolo, and E. Terrill, 2012: Improving HF radar estimates of surface currents using signal quality metrics, with application to the MVCO high-resolution radar system. *J. Atmos. Ocean. Technol.*, **29 (9)**, 1377–1390, doi:10.1175/JTECH-D-11-00160.1.

Klein, P., B. L. Hua, G. Lapeyre, X. Capet, S. Le Gentil, and H. Sasaki, 2008: Upper Ocean Turbulence from High-Resolution 3D Simulations. *J. Phys. Oceanogr.*, **38 (8)**, 1748–1763.

Kohut, J. T., and S. M. Glenn, 2003: Improving HF Radar Surface Current Measurements with Measured Antenna Beam Patterns. *J. Atmos. Ocean. Technol.*, **20 (9)**, 1303–1316, doi:10.1175/1520-0426(2003)020⟨1303:IHRSCM⟩2.0.CO;2.

Koutitonsky, V. G., and G. L. Bugden, 1991: The Physical Oceanography of the Gulf of St. Lawrence: A Review with Emphasis on the Synoptic Variability of the Motion. *Can. Spec. Publ. Fish. Aquat. Sci. 113*, J.-C. Therriault, Ed., the gulf o ed., 57–90.

Koutitonsky, V. G., R. E. Wilson, and M. I. El-Sabh, 1990: On the seasonal response of the Lower St Lawrence Estuary to buoyancy forcing by regulated river runoff. *Estuarine, Coast. Shelf . . .*, 359–379.

Kraichnan, R. H., 1971: Inertial-range transfer in two- and three-dimensional turbulence. *J. Fluid Mech.*, **47 (3)**, 525–535, doi:10.1017/S0022112071001216.

Lefaivre, D., A. D'Astous, and P. Matte, 2016: Hindcast of Water Level and Flow in the St. Lawrence River Over the 2005–2012 Period. *Atmosphere-Ocean*, **54 (3)**, 264–277, doi:10.1080/07055900.2016.1168281.

Lévy, M., R. Ferrari, P. J. Franks, A. P. Martin, and P. Rivière, 2012a: Bringing physics to life at the submesoscale. *Geophys. Res. Lett.*, **39 (14)**, 1–13, doi:10.1029/2012GL052756.

Lévy, M., D. Iovino, L. Resplandy, P. Klein, G. Madec, A. M. Tréguier, S. Masson, and K. Takahashi, 2012b: Large-scale impacts of submesoscale dynamics on phytoplankton: Local and remote effects. *Ocean Model.*, **43-44**, 77–93, doi:10.1016/j.ocemod.2011.12.003.

Lévy, M., P. Klein, A. M. Tréguier, D. Iovino, G. Madec, S. Masson, and K. Takahashi, 2010: Modifications of gyre circulation by sub-mesoscale physics. *Ocean Model.*, **34 (1-2)**, 1–15, doi:10.1016/j.ocemod.2010.04.001.

Lipa, B., and D. Barrick, 1983: Least-squares methods for the extraction of surface currents from CODAR crossed-loop data: Application at ARSLOE. *IEEE J. Ocean. Eng.*, **8 (4)**, 226–253, doi:10.1109/JOE.1983.1145578.

Lipa, B. J., B. Nyden, D. S. Ullman, and E. Terrill, 2006: SeaSonde radial velocities: derivation and internal consistency. *IEEE J. Ocean. Eng.*, **31 (4)**, 850–861, doi:Doi10.1109/Joe.2006.886104.

Martin, A., and P. Pondaven, 2003: On estimates for the vertical nitrate flux due to eddy pumping. *J. Geophys. Res. Ocean.*, **108**, 1–10, doi:10.1029/2003JC001841.

McWilliams, J. C., 1985: A Uniformly Valid Model Spanning the Regimes of Geostrophic and Isotropic, Stratified Turbulence: Balanced Turbulence. *J. Atmos. Sci.*, **42**, 1773–1774, doi:10.1175/1520-0469(1985)042⟨1773:AUVMST⟩2.0.CO;2.

McWilliams, J. C., M. J. Molemaker, and I. Yavneh, 2001: From stirring to mixing of momentum: Cascades from balanced flows to dissipation in the oceanic interior. *Proceeding 12th Aha Hulikoa Hawaiian Winter Work.*, 59–66.

Mensa, J. A., Z. D. Garraffo, A. Griffa, T. M. Özgökmen, A. Haza, and M. Veneziani, 2013: Seasonality of the submesoscale dynamics in the Gulf Stream region. *Ocean Dyn.*, **63 (8)**, 923–941, doi:10.1007/s10236-013-0633-1.

Mensa, J. A., M. L. Timmermans, I. E. Kozlov, W. J. Williams, and T. M. Özgökmen, 2018: Surface Drifter Observations From the Arctic Ocean's Beaufort Sea: Evidence for Submesoscale Dynamics. *J. Geophys. Res. Ocean.*, **123 (4)**, 2635–2645, doi:10.1002/2017JC013728.

Mertz, G., 1989: Low frequency variability in the lower St. Lawrence Estuary. *J. Mar. ...*, **47**, 285–302.

Mertz, G., M. I. El-Sabh, D. Proulx, and A. R. Condal, 1988: Instability of a buoyancy-driven coastal jet: The Gaspé Current and its St. Lawrence precursor. *J. Geophys. Res.*, **93 (C6)**, 6885, doi:10.1029/JC093iC06p06885.

Mertz, G., Y. Gratton, and J. A. Gagné, 1990: Properties of unstable waves in the lower St Lawrence Estuary. *Atmosphere-Ocean*, **28 (2)**, 230–240, doi:10.1080/07055900.1990.9649376.

Mertz, G., and V. G. Koutitonsky, 1992: Wind-induced eddy motion in the lower St. Lawrence Estuary. *Estuarine, Coast. ...*, **34 (6)**, 543–556, doi:10.1016/S0272-7714(05)80061-7.

Milbrandt, J. A., S. Bélair, M. Faucher, M. Vallée, M. L. Carrera, and A. Glazer, 2016: The Pan-Canadian High Resolution (2.5 km) Deterministic Prediction System. *Weather Forecast.*, **31 (6)**, 1791–1816, doi:10.1175/WAF-D-16-0035.1.

Moffatt, H. K., 2014: Note on the triad interactions of homogeneous turbulence. *J. Fluid Mech.*, **741**, 1–11, doi:10.1017/jfm.2013.637.

Molemaker, M. J., J. C. Mcwilliams, and X. Capet, 2010: Balanced and unbalanced routes to dissipation in an equilibrated Eady flow. *J. Fluid Mech.*, **654**, 35–63.

Molemaker, M. J., J. C. McWilliams, and I. Yavneh, 2005: Baroclinic Instability and Loss of Balance. *J. Phys. Oceanogr.*, **35 (9)**, 1505–1517, doi:10.1175/JPO2770.1.

Nadeau, L.-P., and D. N. Straub, 2009: Basin and Channel Contributions to a Model Antarctic Circumpolar Current. *J. Phys. Oceanogr.*, **39 (4)**, 986–1002, doi:DOI10.1175/2008JPO4023.1.

Nikurashin, M., and R. Ferrari, 2010: Radiation and Dissipation of Internal Waves Generated by Geostrophic Motions Impinging on Small-Scale Topography: Application to the Southern Ocean. *J. Phys. Oceanogr.*, **40 (9)**, 2025–2042, doi:10.1175/2010JPO4315.1.

Nikurashin, M., G. K. Vallis, and A. Adcroft, 2013: Routes to energy dissipation for geostrophic flows in the Southern Ocean. *Nat. Geosci.*, **6 (1)**, 48–51, doi:10.1038/ngeo1657.

Ohlmann, C., P. White, L. Washburn, E. Terrill, B. Emery, and M. Otero, 2007: Interpretation of coastal HF radar-derived surface currents with high-resolution drifter data. *J. Atmos. Ocean. Technol.*, **24 (4)**, 666–680, doi:10.1175/JTECH1998.1.

Paquin, J.-P., and Coauthors, 2020: High-resolution modelling of a coastal harbour in the presence of strong tides and significant river runoff. *Ocean Dyn.*, **70 (3)**, 365–385, doi: 10.1007/s10236-019-01334-7.

Pawlowicz, R., B. Beardsley, and S. Lentz, 2002: Classical tidal harmonic analysis including error estimates in MATLAB using T_TIDE. *Comput. Geosci.*, **28 (8)**, 929–937, doi:10.1016/S0098-3004(02)00013-4.

Pearson, J., B. Fox-Kemper, R. Barkan, J. Choi, A. Bracco, and J. C. McWilliams, 2019: Impacts of Convergence on Structure Functions from Surface Drifters in the Gulf of Mexico. *J. Phys. Oceanogr.*, **49 (3)**, 675–690, doi:10.1175/JPO-D-18-0029.1.

Poje, A. C., T. M. özgökmen, D. J. Bogucki, and A. D. Kirwan, 2017: Evidence of a forward energy cascade and Kolmogorov self-similarity in submesoscale ocean surface drifter observations. *Phys. Fluids*, **29 (2)**, doi:10.1063/1.4974331].

Richards, C., D. Bourgault, P. S. Galbraith, A. Hay, and D. E. Kelley, 2013: Measurements of shoaling internal waves and turbulence in an estuary. *J. Geophys. Res. Ocean.*, **118 (1)**, 273–286, doi:10.1029/2012JC008154.

Rocha, C. B., T. K. Chereskin, S. T. Gille, and D. Menemenlis, 2016: Mesoscale to Submesoscale Wavenumber Spectra in Drake Passage. *J. Phys. Oceanogr.*, **46 (2)**, 601–620, doi:10.1175/JPO-D-15-0087.1.

Salmon, R., 1980: Baroclinic instability and geostrophic turbulence. *Geophys. Astrophys. Fluid Dyn.*, **15**, 167–211.

Salmon, R., 1998: *Lectures on geophysical fluid dynamics*. Oxford University Press, 400 pp.

Sasaki, H., P. Klein, B. Qiu, and Y. Sasai, 2014: Impact of oceanic-scale interactions on the seasonal modulation of ocean dynamics by the atmosphere. *Nat. Commun.*, **5**, 5636, doi:10.1038/ncomms6636.

Saucier, F. J., F. Roy, and G. Gilbert, 2003: Modeling the formation and circulation processes of water masses and sea ice in the Gulf of St. Lawrence, Canada. *J. Geophys. Res.*, **108 (C8)**, 3269, doi:10.1029/2000JC000686.

Schmidt, R., 1986: Multiple emitter location and signal parameter estimation. *IEEE Trans. Antennas Propag.*, **34 (3)**, 276–280, doi:10.1109/TAP.1986.1143830.

Scott, R. B., 2001: Evolution of energy and enstrophy containing scales in decaying, two-dimensional turbulence with friction. *Phys. Fluids*, **13 (9)**, 2739–2742, doi:10.1063/1.1388181.

Scott, R. B., and B. K. Arbic, 2007: Spectral Energy Fluxes in Geostrophic Turbulence: Implications for Ocean Energetics. *J. Phys. Oceanogr.*, **37 (3)**, 673–688, doi: 10.1175/JPO3027.1.

Scott, R. B., J. A. Goff, A. C. Naveira Garabato, and A. J. Nurser, 2011: Global rate and spectral characteristics of internal gravity wave generation by geostrophic flow over topography. *J. Geophys. Res. Ocean.*, **116 (9)**, 1–14, doi:10.1029/2011JC007005.

Scott, R. B., and F. Wang, 2005: Direct Evidence of an Oceanic Inverse Kinetic Energy Cascade from Satellite Altimetry. *J. Phys. Oceanogr.*, **35 (9)**, 1650–1666.

Shcherbina, A. Y., E. A. D'Asaro, C. M. Lee, J. M. Klymak, M. J. Molemaker, and J. C. McWilliams, 2013: Statistics of vertical vorticity, divergence, and strain in a developed submesoscale turbulence field. *Geophys. Res. Lett.*, **40 (17)**, 4706–4711, doi:10.1002/grl.50919.

Silverthorne, K. E., and J. M. Toole, 2009: Seasonal Kinetic Energy Variability of Near-Inertial Motions. *J. Phys. Oceanogr.*, **39 (4)**, 1035–1049, doi:10.1175/2008JPO3920.1.

Smith, G. C., F. Roy, and B. Brasnett, 2013: Evaluation of an operational ice-ocean analysis and forecasting system for the Gulf of St Lawrence. *Q. J. R. Meteorol. Soc.*, **139 (671)**, 419–433, doi:10.1002/qj.1982.

Smith, G. C., and Coauthors, 2018: Impact of coupling with an ice-ocean model on global medium-range NWP forecast skill. *Mon. Weather Rev.*, **146 (4)**, 1157–1180, doi:10.1175/MWR-D-17-0157.1.

Soh, H. S., and S. Y. Kim, 2018: Diagnostic Characteristics of Submesoscale Coastal Surface Currents. *J. Geophys. Res. Ocean.*, 1–22, doi:10.1002/2017JC013428.

Straub, D. N., and B. T. Nadiga, 2014: Energy Fluxes in the Quasigeostrophic Double Gyre Problem. *J. Phys. Oceanogr.*, **44 (6)**, 1505–1522, doi:10.1175/JPO-D-13-0216.1.

Su, Z., J. Wang, P. Klein, A. F. Thompson, and D. Menemenlis, 2018: Ocean submesoscales as a key component of the global heat budget. *Nat. Commun.*, **9 (1)**, 1–8, doi:10.1038/s41467-018-02983-w.

Taylor, M. H., M. Losch, M. Wenzel, and J. Schröter, 2013: On the sensitivity of field reconstruction and prediction using empirical orthogonal functions derived from Gappy data. *J. Clim.*, **26 (22)**, 9194–9205, doi:10.1175/JCLI-D-13-00089.1.

Taylor, S., and D. Straub, 2016: Forced Near-Inertial Motion and Dissipation of Low-Frequency Kinetic Energy in a Wind-Driven Channel Flow. *J. Phys. Oceanogr.*, **46 (1)**, 79–93, doi:10.1175/JPO-D-15-0060.1.

Thomas, L. N., A. Tandon, and A. Mahadevan, 2008: Submesoscale processes and dynamics. *Geophys. Monogr. Ser.*, 17–38.

Torres, H. S., P. Klein, D. Menemenlis, B. Qiu, Z. Su, J. Wang, S. Chen, and L. L. Fu, 2018: Partitioning Ocean Motions Into Balanced Motions and Internal Gravity Waves: A Modeling Study in Anticipation of Future Space Missions. *J. Geophys. Res. Ocean.*, **123 (11)**, 8084–8105, doi:10.1029/2018JC014438.

Tsinober, A., 1996: *Turbulence: The Legacy of A. N. Kolmogorov . By U. F RISCH . Cambridge University Press, 1995. 296 pp. ISBN 0 521 45713 0. £15.95.*, Vol. 317. 407–410 pp., doi:10.1017/S0022112096210791.

Tulloch, R., J. Marshall, C. Hill, and K. S. Smith, 2011: Scales, Growth Rates, and Spectral Fluxes of Baroclinic Instability in the Ocean. *J. Phys. Oceanogr.*, **41 (6)**, 1057–1076, doi:10.1175/2011JPO4404.1.

Vallis, G. K., 2006: *Atmospheric and Oceanic Fluid Dynamics*. Cambridge University Press, Cambridge, U.K., 745 pp.

Vanneste, J., 2013: Balance and Spontaneous Wave Generation in Geophysical Flows. *Annu. Rev. Fluid Mech.*, **45**, 147–72, doi:10.1146/annurev-fluid-011212-140730.

Vanneste, J., and I. Yavneh, 2004: Exponentially Small Inertia–Gravity Waves and the Breakdown of Quasigeostrophic Balance. *J. Atmos. Sci.*, **61 (2)**, 211–223, doi:10.1175/1520-0469(2004)061⟨0211:ESIWAT⟩2.0.CO;2.

Wunsch, C., 1997: The Vertical Partition of Oceanic Horizontal Kinetic Energy. *J. Phys. Oceanogr.*, **27 (8)**, 1770–1794, doi:10.1175/1520-0485(1997)027⟨1770:TVPOOH⟩2.0.CO;2.

Wunsch, C., and R. Ferrari, 2004: VERTICAL MIXING, ENERGY, AND THE GENERAL CIRCULATION OF THE OCEANS. *Annu. Rev. Fluid Mech.*, **36 (1)**, 281–314, doi:10.1146/annurev.fluid.36.050802.122121.

Xiao, Z., M. Wan, S. Chen, and G. L. Eyink, 2009: Physical mechanism of the inverse energy cascade of two-dimensional turbulence: a numerical investigation. *J. Fluid Mech.*, **619**, 1–44.

Xie, J.-H., and J. Vanneste, 2015: A generalised-Lagrangian-mean model of the interactions between near-inertial waves and mean flow. *J. Fluid Mech.*, **774**, 143–169, doi:10.1017/jfm.2015.251.

Xu, Y., and L.-L. Fu, 2011: Global Variability of the Wavenumber Spectrum of Oceanic Mesoscale Turbulence. *J. Phys. Oceanogr.*, **41 (4)**, 802–809, doi:10.1175/2010jpo4558.1.

Yaremchuk, M., and A. Sentchev, 2009: Mapping radar-derived sea surface currents with a variational method. *Cont. Shelf Res.*, **29 (14)**, 1711–1722, doi:10.1016/j.csr.2009.05.016.

Yaremchuk, M., and A. Sentchev, 2011: A combined EOF/variational approach for mapping radar-derived sea surface currents. *Cont. Shelf Res.*, **31 (7-8)**, 758–768, doi:10.1016/j.csr.2011.01.009.